Precursors and nuclei, the early stages of flow-induced crystallization

Citation for published version (APA):
Steenbakkers, R. J. A. (2009). *Precursors and nuclei, the early stages of flow-induced crystallization*. [Phd Thesis 1 (Research TU/e / Graduation TU/e), Mechanical Engineering]. Technische Universiteit Eindhoven. https://doi.org/10.6100/IR656498

DOI:
10.6100/IR656498

Document status and date:
Published: 01/01/2009

Document Version:
Publisher's PDF, also known as Version of Record (includes final page, issue and volume numbers)

Please check the document version of this publication:

• A submitted manuscript is the version of the article upon submission and before peer-review. There can be important differences between the submitted version and the official published version of record. People interested in the research are advised to contact the author for the final version of the publication, or visit the DOI to the publisher's website.
• The final author version and the galley proof are versions of the publication after peer review.
• The final published version features the final layout of the paper including the volume, issue and page numbers.

Link to publication

General rights
Copyright and moral rights for the publications made accessible in the public portal are retained by the authors and/or other copyright owners and it is a condition of accessing publications that users recognise and abide by the legal requirements associated with these rights.

- Users may download and print one copy of any publication from the public portal for the purpose of private study or research.
- You may not further distribute the material or use it for any profit-making activity or commercial gain
- You may freely distribute the URL identifying the publication in the public portal.

If the publication is distributed under the terms of Article 25fa of the Dutch Copyright Act, indicated by the "Taverne" license above, please follow below link for the End User Agreement:

www.tue.nl/taverne

Take down policy
If you believe that this document breaches copyright please contact us at:

openaccess@tue.nl

providing details and we will investigate your claim.

Download date: 04. Oct. 2023

Precursors and nuclei, the early stages of flow-induced crystallization

Precursors and nuclei, the early stages of flow-induced crystallization / by R.J.A. Steenbakkers.
Technische Universiteit Eindhoven, 2009.

A catalogue record is available from the Eindhoven University of Technology Library:
ISBN 978-90-386-2114-2
NUR 971

This thesis was prepared with the $\LaTeX\,2_\varepsilon$ documentation system.
Reproduction: University Press Facilities, Eindhoven, The Netherlands.
Cover design: R.J.A. Steenbakkers.

Precursors and nuclei, the early stages of flow-induced crystallization

PROEFSCHRIFT

ter verkrijging van de graad van doctor aan de
Technische Universiteit Eindhoven, op gezag van de
rector magnificus, prof.dr.ir. C.J. van Duijn, voor een
commissie aangewezen door het College voor
Promoties in het openbaar te verdedigen
op maandag 21 december 2009 om 16.00 uur

door

Rudi Johannes Antonius Steenbakkers

geboren te Geldrop

Dit proefschrift is goedgekeurd door de promotor:

prof.dr.ir. H.E.H. Meijer

Copromotor:
dr.ir. G.W.M. Peters

Deep in the human unconscious is a pervasive need for a logical universe that makes sense.
But the real universe is always one step beyond logic.

– Frank Herbert, *Dune* –

Contents

Summary **xi**

1 Introduction **1**

2 Suspension-based rheological modeling of crystallizing polymer melts **3**

2.1 Introduction 4

2.2 Modeling 7

2.2.1 Linear viscoelastic suspension rheology 8

2.2.2 Nonlinear viscoelastic suspension rheology 13

2.3 Evaluation of a linear viscoelastic model 17

2.3.1 History and relation to other models 18

2.3.2 Influence of phase properties 21

2.3.3 Comparison to numerical and experimental data 23

2.3.4 Application to crystallization experiments 24

2.4 Conclusions 35

Appendices 36

2A 3D generalized self-consistent method and Bousmina's linear viscoelastic model 36

2B 2D generalized self-consistent method 36

3 Local formulation of flow-enhanced nucleation coupled with rheology **41**

3.1 Introduction 42

3.2 Objective and outline 44

3.3 Rheological modeling 45

3.4 Spherulitic structure formation 47

3.4.1 Precursors of crystalline nuclei 48

3.4.2 Quiescent and flow-induced precursors 50

3.5 Local formulation of flow-enhanced nucleation 52

3.5.1 Influence of convection 54

3.5.2 Swallowing of HMW chains by growing nuclei 58

3.6 Results . . . 60
3.7 Conclusions . . . 62
Appendices . . . 64
 3A Instantaneous nucleation of precursors . . . 64
 3B Creation in and convection out of incubators . . . 65
 3C Evaluation of flow-induced precursors as branch points . . . 68

4 Validation of a global formulation of flow-enhanced nucleation 71
4.1 Introduction and outline of the model . . . 72
 4.1.1 Creation and nucleation of precursors . . . 72
 4.1.2 Saturation . . . 73
4.2 Experiments . . . 74
 4.2.1 Flow-enhanced nucleation . . . 74
 4.2.2 Rheological characterization . . . 76
4.3 Results and Discussion . . . 79
 4.3.1 Interference of flow with nucleation . . . 79
 4.3.2 Dissolution of precursors . . . 80
 4.3.3 Role of orientation and stretch . . . 80
 4.3.4 Sensitivity to the longest Rouse time estimate . . . 86
4.4 Conclusions . . . 86
Appendices . . . 88
 4A Rolie-Poly and XPP constitutive equations . . . 88
 4B Simulations of FIC experiments of Housmans et al. . . . 89

5 Temperature effects on flow-enhanced nucleation and its saturation 93
5.1 Introduction and outline . . . 94
5.2 Experiments . . . 94
 5.2.1 Flow-enhanced nucleation . . . 94
 5.2.2 Rheological characterization . . . 95
5.3 Results and discussion . . . 95
 5.3.1 Flow-enhanced nucleation . . . 95
 5.3.2 Saturation . . . 97
5.4 Conclusions . . . 101

6 Conclusions and prospects 103
6.1 Rheology of crystallizing melts in the late stages . . . 103
6.2 Local versus global flow-enhanced nucleation . . . 103
 6.2.1 Role of dormant flow-induced precursors . . . 104
6.3 FIC criteria: does work work for pointlike precursors? . . . 105
6.4 Bimodal blends . . . 107
 6.4.1 Multi-mode Giesekus model . . . 108

6.4.2 Multi-mode XPP model 108

References **111**

Samenvatting **129**

Acknowledgements **131**

Curriculum vitae **133**

Summary

Precursors and nuclei, the early stages of flow-induced crystallization

Flow-induced crystallization (FIC) is the main factor determining the properties of melt-processed semicrystalline polymer products. Therefore it has received much attention in scientific research, both experimental and theoretical. Although the essential phenomena in FIC are slowly being unraveled, a comprehensive theoretical framework, able to explain all these phenomena, is still lacking.

Crystallization of polymers can be divided into three regimes:

1. quiescent crystallization, in which spherical structures (spherulites) are formed,
2. flow-enhanced nucleation, leading to a higher number density of spherulites,
3. formation of oriented fibrillar nuclei, which are a template of anisotropic crystalline structures.

Upon increasing the rate or duration of flow, transitions from regime 1 to regime 2 and regime 3 can be observed. The objective of this thesis is to investigate how flow-enhanced nucleation (regime 2) can be modeled from a rheological point of view, including the coupling between the structure formed and the viscoelastic behavior of the melt.

The results of this thesis are twofold. First, the rheology of polymer melts in the late stages of crystallization, characterized, in regime 2, by growth of spherulites, is captured by a viscoelastic suspension model. Secondly, flow-enhanced nucleation in the early stages, which determines the subsequent spherulitic structure development, is modeled. A local and a global formulation of this phenomenon are compared. The local formulation offers a consistent theoretical concept for the processes of creation and nucleation of flow-induced precursors (subcritical nuclei). However, it is not yet able to explain experimental observations. The more empirical global formulation, on the other hand, agrees very well with experimental data. Conclusions are drawn from these results and recommendations for future research are given.

CHAPTER ONE

Introduction

Flow-induced crystallization, which is unavoidable in processing of semicrystalline polymers, is a wonderful example of the 'butterfly effect' [92]. After only a few seconds of flow in the amorphous state, the time scale of subsequent crystallization is typically reduced by an order of magnitude for moderate deformation rates [50, 97, 191] and even by a few orders of magnitude for high deformation rates, as encountered in processing [14, 118]. This is related to the drastic morphological changes that occur, from increases on the order of several decades in the number density of isotropic spherulites [97, 191] to rapid growth of anisotropic crystallites, which are almost always perfectly oriented in the flow direction [118, 173].

Many properties of polymer products strongly depend on the morphology. Examples are mechanical properties, such as (anisotropic) stiffness, toughness, and wear resistance, but also dimensional stability and surface roughness. Hence flow-induced crystallization is a crucial phenomenon in processing of semicrystalline polymers for high-performance products. In typical industrial applications, which involve complex time-dependent flow and temperature fields, predicting morphology development is a challenging problem [44].

Flow-induced crystallization is closely related to the chain-like molecular structure of polymers and their consequently time-dependent (viscoelastic) deformation behavior. Experimental studies show that chains of high molecular weight govern the kinetics of flow-enhanced nucleation and the transition to oriented growth, and based on these observations, theoretical concepts have been developed [146, 195]. This growing fundamental understanding should be exploited to design new experiments, which can give more detailed information about the origins of flow-induced crystallization. Unfortunately, not always the most insightful choices are made.

As an example, Elmoumni *et al.* [60] subjected two isotactic polypropylene melts, labeled iPP171 and iPP300 based on their weight-averaged molecular weights, to short-term shear flow. They did this at comparable Weissenberg numbers (products of strain rate and relaxation time), which means that the flow strength, as experienced by the molecules, was similar. The authors reported no significant differences in structure development between these materials. Hence, they concluded that relaxation of chains after flow, which takes more time in iPP300 due to its higher molecular weight, does not play a role in flow-induced crystallization. However, since they applied the same strain in all experiments, the shear times at comparable Weissenberg numbers were longer for iPP300 than for iPP171 (by a factor of four to five). Thus, while the molecules experienced a similar flow, more time was available for structure formation during flow of iPP300, in addition to its slower relaxation afterwards. The conclusion of Elmoumni *et al.* can therefore not be drawn from their own experiments. The similar structure development in the two materials then becomes more intriguing. (Note that this similarity was deduced from small-angle light scattering and wide-angle X-ray diffraction. They also showed optical micrographs, in which the transition to oriented crystallization occurs at a lower Weissenberg number for the higher molecular weight [60].)

The tendency to keep the strain constant, thereby varying both the strain rate and the duration of flow, is widespread among experimentalists since the early work of Vleeshouwers and Meijer [203]. It originates from the notion that the same strain gives the same deformation history, which is not true for the *molecular* deformation history. A purely macroscopic quantity like strain is unable to characterize the complex nonlinear viscoelastic behavior of polymer melts, especially if a process far from equilibrium, e.g. flow-induced crystallization, takes place. If the influence of macroscopic flow parameters, such as strain rate and flow time, is to be investigated unambiguously, they should be varied one at a time.

This thesis presents a theoretical framework for flow-enhanced nucleation and spherulitic structure formation, which can be extended straightforwardly to include the transition to oriented growth [44]. Ideally, however, it will not only be read by theorists, but also by experimentalists, who may find many points of departure for the design of new experiments.

The outline of this thesis is as follows. In Chapter 2, a method is developed to calculate the evolution of rheological properties in the late stages of crystallization, which are dominated by filling of the material volume with crystalline structures. Chapters 3 to 5 focus on the early stages of flow-induced crystallization, where the precursors of crystalline nuclei are formed, which determine subsequent structure development. Two different formulations of a flow-enhanced nucleation model are discussed in Chapter 3 versus Chapters 4 and 5. Based on the main conclusions, some challenges and opportunities for future research are discussed in Chapter 6.

Chapter two

Suspension-based rheological modeling of crystallizing polymer melts[1]

Abstract

The applicability of suspension models to polymer crystallization is discussed. Although direct numerical simulations of flowing particle-filled melts are useful for gaining understanding about the rheological phenomena involved, they are computationally expensive. A more coarse-grained suspension model, which can relate the parameters in a constitutive equation for the two-phase material to morphological features, such as the volume fractions of differently shaped crystallites and the rheological properties of both phases, will be more practical in numerical polymer processing simulations. General issues, concerning the modeling of linear and nonlinear viscoelastic phenomena induced by rigid and deformable particles, are discussed. A phenomenological extension of linear viscoelastic suspension models into the nonlinear regime is proposed. A number of linear viscoelastic models for deformable particles are discussed, focusing on their possibilities in the context of polymer crystallization. The predictions of the most suitable model are compared to direct numerical simulation results and experimental data.

---

[1] This chapter has been reproduced, slightly adapted, from R.J.A. Steenbakkers and G.W.M. Peters, *Rheologica Acta* 47:643–665, 2008. DOI 10.1007/s00397-008-0273-4

2.1 Introduction

The significant effects of flow on the crystallization kinetics of polymers, specifically the increase of the nucleation density and the transition from spherical to anisotropic growth, have incited a great deal of scientific effort, both experimental and theoretical. Experimental studies usually involve subjecting an undercooled melt to a short, well defined flow in the early stage of crystallization, where nearly all of the material is still in the amorphous phase, and monitoring the subsequent structure development by any one of a variety of measurement techniques, including dilatometry, rheometry, microscopy, and scattering and diffraction methods, or a combination of these methods. Since our understanding of the phenomena occurring in the early stage, which determine to a great extent the final semicrystalline morphology, is still incomplete, it is not surprising that far less attention has been devoted to the influence of structure development on the rheology of a crystallizing melt. However, once the mechanisms of flow-induced crystallization are known, this will be the first step in going from short-term flow to continuous flow experiments, where the local process of phase transformation is affected by the development of semicrystalline structures on an orders of magnitude larger length scale and vice versa. These experiments will be useful as validation for polymer processing simulations.

During the last decade, a number of concepts have been proposed that deal with the rheology of crystallizing polymer melts. Winter and coworkers [95,96,160–163,208] observed an apparent similarity to the rheology of chemical gels, in which polymer molecules are connected by permanent crosslinks into a sample spanning network. They considered crystallizing melts as physical gels, in which crystallites were connected by amorphous 'tie chains'.

Janeschitz-Kriegl *et al.* [107] estimated the fraction of chains involved in nuclei in their experiments and found it to be so small that, during the major part of the crystallization process, no interaction among the nuclei or the resulting spherulites was to be expected. To explain the observed nonlinear increase of the nucleation density as a function of the mechanical work supplied to the melt, they introduced the concept of flow-induced activation of dormant nuclei [108, 109].

Another explanation of the strong self-enhancing effect of nucleation was proposed by Zuidema *et al.* [212, 213]. They assumed that nuclei *locally* act as physical crosslinks, increasing the probability that chain segments remain in an ordered state long enough to serve as new nuclei. In other words, gel-like behavior is not caused by the formation of a percolating network of semicrystalline domains, but by effective branching of the amorphous phase. Low-frequency rheological measurements, recently published by Coppola *et al.* [43], seem to support this idea (but see the discussion in Section 2.3.4).

A few attempts have been made to capture the kinetics of flow-induced crystallization in a continuum description, embedded in a formal theoretical framework of nonequilibrium thermodynamics. For example, the Poisson bracket formalism [23] was used by Doufas *et al.* [52]. In their model, which was applied to flow-induced crystallization during fiber spinning [53, 54, 56, 57] and film blowing [55], details of the microstructure, e.g. size and shape of the crystallites, are not taken into account. The crystalline phase is simply modeled as a collection of bead-rod chains. A Giesekus model is used for the amorphous phase, with the relaxation time depending on the degree of crystallinity χ as

$$\lambda_{am} = \lambda_{am,0}\,(1-\chi)^2 \tag{2.1}$$

to account for the loss of chain segments due to crystallization.

Hütter [99] developed a flow-induced spherulitic crystallization model based on the 'general equation for the nonequilibrium reversible-irreversible coupling' or GENERIC [76, 152]. The microstructure enters his model through the evolution of the interfacial area, obtained from the Schneider rate equations [168]. This gives rise to a pressure term in the momentum balance, related to the surface tension, as well as to an interfacial heat flux in the energy balance. However, the extra stress tensor is written as the sum of the viscous stress contributions from the matrix and the spherulites,

$$\boldsymbol{\tau} = \boldsymbol{\tau}_{am} + \boldsymbol{\tau}_{sc}\,, \tag{2.2}$$

as if the material were a homogenous mixture. Here 'am' stands for the amorphous matrix and 'sc' for the partially crystalline, partially amorphous material inside the spherulites, which we call the semicrystalline phase. When both phases are incompressible, the partial stresses are given by

$$\boldsymbol{\tau}_{am} = 2\,(1-\phi)\,\eta_{am}\boldsymbol{D} \tag{2.3}$$

and

$$\boldsymbol{\tau}_{sc} = 2\phi\eta_{sc}\boldsymbol{D}\,, \tag{2.4}$$

where ϕ is the volume fraction of spherulites, or degree of space filling, and $\boldsymbol{D}$ is the deformation rate tensor. Eqs. (2.2), (2.3), and (2.4) yield the effective viscosity

$$\eta = (1-\phi)\,\eta_{am} + \phi\eta_{sc}\,. \tag{2.5}$$

Thus, no connection is made between rheological properties and microstructural features. Van Meerveld *et al.* [193, 196] extended Hütter's model with a description of the viscoelastic behavior of the melt and used it to simulate fiber spinning. In contrast to Hütter *et al.* [100], who developed a single set of rate equations, allowing for changes in crystallite shapes and growth directions, they used two sets of rate equations to describe the evolution of spherulites and oriented crystallites. Although morphology development is incorporated in these models, at the continuum level the stress is determined by the additive ‘rule of mixtures’, Eq. (2.2). The question remains whether this is a realistic choice for describing the rheology of crystallizing polymer melts.

The morphology that develops as nuclei grow into crystallites with distinct shapes agrees with the basic concept of a suspension: isolated particles (the crystallites) are scattered throughout a continuous matrix (the amorphous phase). It is well known that the rule of mixtures fails to describe the volume fraction dependence of the rheological properties of suspensions. The same may hence be expected for crystallizing melts. Boutahar *et al.* [28,29], Tanner [183,184], and Van Ruth *et al.* [197] therefore used ideas from suspension rheology to describe the evolution of linear viscoelastic properties during crystallization, as a function of the degree of space filling and the properties of the individual phases.

Crystallizing polymer melts differ from ordinary suspensions in a number of ways. The crystallites grow, they can have different shapes depending on the flow history, and their properties evolve in time. The latter can be shown by combined optical microscopy and rheological measurements during crystallization. The dynamic modulus continues to increase after the completion of space filling [197]. This is the result of perfection of the semicrystalline phase, also referred to as secondary crystallization. In this chapter, crystallites are therefore treated as particles whose properties depend on their internal degree of crystallinity,

$$\chi_1 = \frac{\chi}{\phi}, \tag{2.6}$$

thus providing the possibility to incorporate perfection in the model. The surrounding amorphous phase acts as a matrix, whose properties change as well. Small-amplitude oscillatory shear measurements by Vega *et al.* [198] show strongly increased storage and loss moduli, measured at a constant frequency, directly after short steady shear flows. The same effect, but less severe, can be recognized in the work of Housmans *et al.* [97]. At the same time scale, no significant degree of space filling was observed by means of optical microscopy [D.G. Hristova, personal communication]. Therefore these results cannot be explained by particle-like effects of the crystallites on the overall rheology. Coppola *et al.* [43] drew the same conclusion from a comparison of dynamic measurements on partially crystallized melts and on an amorphous melt filled with solid spheres. However, for the partially crystallized samples, the degree of space filling was probably underestimated (see Section 2.3.4).

To explain these observations, the amorphous matrix will be described as a crosslinking melt, with flow-induced nucleation precursors acting as physical crosslinks [212,213]. In the later stages of crystallization, the flow is severely disturbed by the presence of crystallites. Both phenomena have a nonlinear effect on the kinetics of flow-induced crystallization; furthermore, they are mutually coupled. The influence of flow on the early-stage kinetics, related to structure development within the amorphous matrix, will be discussed in Chapters 3, 4, and 5. Two-dimensional simulations of flow-induced crystallization in a particle-filled polymer melt have already been performed without taking the physical crosslinking effect into account [104]. Here we focus on the later stages of crystallization, which are dominated by space filling and perfection of the internal structure of the crystallites.

A suspension model for crystallization under real processing conditions has to meet at least the following requirements:

1. The model has to be applicable in the entire range of volume fractions, i.e. from the purely amorphous state ($\phi = 0$) to complete filling of the material by the crystallites ($\phi = 1$). This rules out dilute suspension theories, although an interpolation between analytical results for $\phi \to 0$ and $\phi \to 1$ has been applied with some success [184].

2. The possibility to incorporate differently shaped particles is essential for describing different semicrystalline morphologies. Here, spherulites and oriented crystallites are represented by spheres and cylinders, respectively, and we need a suspension model that can deal with both.

3. To describe the evolution of linear viscoelastic properties, as measured during crystallization, the model must provide a relationship between these properties and morphological features.

4. Quantitative description of most manufacturing processes requires that the effect of crystallization on the nonlinear viscoelastic behavior is captured as well.

In Section 2.2.1, we briefly review how the effective dynamic mechanical properties of a linear viscoelastic suspension can be obtained from an elastic suspension model by means of the correspondence principle [37, 83–85]. The consequences of modeling crystallites as either rigid or deformable particles are discussed. No specific suspension model is used; the discussion is of a general nature. A complementary phenomenological modeling approach to nonlinear viscoelastic suspension rheology is introduced in Section 2.2.2. Its ability to qualitatively reproduce results from experiments [140, 149] and numerical simulations [102] is investigated. The properties of a specific linear viscoelastic suspension model are discussed in Sections 2.3.1 and 2.3.2. In Section 2.3.3, its predictions are compared to numerical [102] and experimental [140] results for rigid particle suspensions. In Section 2.3.4, they are compared to experimental data on quiescent and short-term shear-induced crystallization of different polymer melts [J.F. Vega and D.G. Hristova, private communications] and [28, 29, 43]. The conclusions of this chapter are summarized in Section 2.4.

2.2 Modeling

Various constitutive models are available to describe the nonlinear viscoelastic behavior of the matrix of the suspension, i.e. the amorphous phase of the crystallizing melt. Differential models are most suited for numerical simulations of complex flows. Some of the most advanced are the Rolie-Poly model [130] for linear melts and the Pom-Pom [142] and eXtended Pom-Pom (XPP [202]) models for branched melts. These and other differential models can be written in a general form, involving a slip tensor, which represents the nonaffine motion of polymer chains with respect to the macroscopic flow [156].

The linear viscoelastic behavior of the matrix is characterized by the complex dynamic modulus, which is a function of the frequency ω,

$$G_0^*(\omega) = G_0'(\omega) + jG_0''(\omega) \tag{2.7}$$

and which is fitted by an M-mode discrete relaxation spectrum, giving the storage modulus

$$G_0'(\omega) = \sum_i^M G_{0,i} \frac{\lambda_{0,i}^2 \omega^2}{1 + \lambda_{0,i}^2 \omega^2} \tag{2.8}$$

and the loss modulus

$$G_0''(\omega) = \sum_i^M G_{0,i} \frac{\lambda_{0,i} \omega}{1 + \lambda_{0,i}^2 \omega^2} \tag{2.9}$$

in terms of the moduli $G_{0,i}$ and relaxation times $\lambda_{0,i}$. The influence of particles on the linear viscoelastic properties of a suspension is discussed next.

2.2.1 Linear viscoelastic suspension rheology

Our point of departure is the general expression for the effective shear modulus G of a suspension of elastic particles dispersed throughout an elastic matrix [190],

$$G(\phi) = f_G(\phi, \underset{\sim}{s}, \nu_0, \nu_1, \mu, \ldots) G_0 \,, \tag{2.10}$$

where ϕ is the volume fraction of the dispersed phase, $\underset{\sim}{s}$ is an array of shape factors that define the particle geometry, ν_0 and ν_1 are the Poisson ratios of the continuous phase and the dispersed phase, respectively, and μ is the ratio of the shear moduli of the phases,

$$\mu = \frac{G_1}{G_0} \,. \tag{2.11}$$

In general, G_0 and G_1 only occur in suspension models via this ratio. The dimensionless quantity $f_G = G/G_0$ is known as the relative shear modulus. Expressions analogous to Eq. (2.10) can be written down for the effective bulk modulus K, Young's modulus E, and Poisson ratio ν [190]. Any two of these properties determine the mechanical behavior of an elastic material. In viscous systems, the relative viscosity $f_\eta = \eta/\eta_0$ is used.

To describe suspensions where both the matrix and the particles are linear viscoelastic, the effective dynamic shear modulus is written in the same form as in the elastic case,

$$G^*(\omega,\phi) = f_G^*(\phi, \underset{\sim}{s}, \nu_0, \nu_1, \mu^*(\omega), \ldots) G_0^*(\omega) \tag{2.12}$$

with $\mu^* = G_1^*/G_0^*$. This implies that G_0^* and G_1^* are known in the same range of frequencies. The relative dynamic shear modulus will later on be denoted by $f_G^*(\omega,\phi)$ or simply by f_G^*. But one should keep in mind that, besides the frequency and the volume fraction, it also depends on the geometry of the particles and the material properties of the phases. The dynamic modulus ratio μ^* governs the frequency dependence of f_G^*, which makes it a complex quantity,

$$f_G^*(\omega,\phi) = f_G'(\omega,\phi) + j f_G''(\omega,\phi)\,. \tag{2.13}$$

The Poisson ratios may, in principle, also be complex. However, experiments on different thermoplastic polymers have shown that the imaginary part of the complex Poisson ratio $\nu^* = \nu' - j\nu''$ has a maximum at the glass transition temperature T_g, where it is about an order of magnitude smaller than the real part, i.e. $\nu'' \sim 10^{-2}$, and that it decreases strongly upon departure from T_g [4, 206]. We therefore assume that, in the present case, all Poisson ratios are real.

For a constant volume fraction, the correspondence principle [37, 83–85] relates the relative dynamic shear modulus f_G^* to the relative shear modulus of an elastic suspension with the same microstructure. In the case of a steady-state oscillatory deformation with frequency ω, f_G^* is simply obtained by replacing the moduli G_0 and G_1 in the elastic model by their dynamic counterparts G_0^* and G_1^*. Of course the volume fraction of crystallites in a crystallizing polymer melt is not constant. However, according to Tanner [184], if ϕ changes slowly compared to the characteristic time scale of stress relaxation, the correspondence principle will still be a good approximation.

At this point, it should be noted that the density difference between the amorphous phase and the semicrystalline phase of a polymer has an influence on the volume fraction, which is given by

$$\phi = \frac{\tilde{\phi}\rho_{am}}{\tilde{\phi}\rho_{am} + \left(1-\tilde{\phi}\right)\rho_{sc}}\,. \tag{2.14}$$

Here ρ_{am} and ρ_{sc} are the densities of the amorphous and the semicrystalline phase, respectively. The volume fraction $\tilde{\phi}$, uncorrected for the density difference, is calculated as the volume of transformed amorphous phase per initial unit volume of material. Eq. (2.14) can easily be included in the rate equations for the growth of the semicrystalline phase [129, 168]. In Section 2.3.4, where the actual volume fraction is determined directly from microscopic images, no correction is necessary.

Crystallites as rigid particles

Since, in general, the dynamic modulus of a polymer increases by several orders of magnitude during crystallization, one may argue that the crystallites can be considered rigid. Any suspension model should make sure that, with this assumption, all occurrences of μ^* cancel each other out. This is trivial; if the infinite modulus ratio remained, the effective modulus of the suspension would already go to infinity when adding an infinitesimal amount of particles to the pure matrix, which is unrealistic. If the Poisson ratios are real, as we assume here, for rigid particles the relative dynamic modulus thus becomes real as well,

$$f_G(\phi) \equiv \lim_{|\mu^*|\to\infty} f_G^*(\phi, \mu^*(\omega)) \,. \tag{2.15}$$

The effective storage modulus is then given by

$$G'(\omega, \phi) = f_G(\phi) \sum_i^M G_{0,i} \frac{\lambda_{0,i}^2 \omega^2}{1 + \lambda_{0,i}^2 \omega^2} \tag{2.16}$$

and the effective loss modulus by

$$G''(\omega, \phi) = f_G(\phi) \sum_i^M G_{0,i} \frac{\lambda_{0,i} \omega}{1 + \lambda_{0,i}^2 \omega^2} \,. \tag{2.17}$$

Hence, upon adding particles, all moduli increase by the same amount, which moreover is independent on the frequency, whereas the relaxation times remain equal to those of the matrix.

For suspensions in which the particles are essentially rigid, the validity of Eqs. (2.15), (2.16), and (2.17) has been confirmed by experiments as well as numerical simulations. Schaink *et al.* [166] investigated the individual effects of Brownian motion and hydrodynamic interactions on the viscosity of suspensions of rigid spheres by means of Stokesian dynamics simulations. They used a viscous fluid as well as a linear viscoelastic fluid as the matrix and found that the hydrodynamic contributions in both cases were similar. Expressions for the components $\eta' = G''/\omega$ and $\eta'' = G'/\omega$ of the dynamic viscosity, equivalent to Eqs. (2.16) and (2.17), were obtained. Using the relative viscosity from the viscous simulation results, Schaink et al. were able to reproduce some of the oscillatory shear data of Aral and Kalyon [7] for suspensions of glass spheres in a viscoelastic fluid, namely those with $\phi = 0.1$ and $\phi = 0.2$. See *et al.* [169] subjected suspensions of spherical polyethylene particles in two different viscoelastic matrix fluids to small-amplitude oscillatory squeezing flow. They found that indeed, independent on the frequency, the relative quantities $\eta'(\phi)/\eta'_0$ of one system and $G'(\phi)/G'_0$ and $G''(\phi)/G''_0$ of the other system were all described by a single master curve in the examined volume fraction range, $0 \leqslant \phi \leqslant 0.4$.

Since we want to be able, in a later stage, to extend our work with a model for perfection of the semicrystalline phase and study its effect on mechanical properties, we prefer to treat crystallites as deformable particles. In this way also the possibility to model relatively weak (low χ_1) as well as stiff (high χ_1) semicrystalline structures remains. Moreover, in numerical polymer processing simulations, it is preferable to work with a dynamic modulus that remains finite. This is not the case if crystallites are modeled as rigid particles up to large volume fractions.

Tanner [184] proposed to use two separate models. The first gives f_G for small volume fractions, assuming the crystallites to be rigid, according to Eq. (2.15). From the second model, which describes the crystallizing melt at large volume fractions, the additional relative dynamic modulus

$$h_G^* = \frac{G^*}{G_1^*} \tag{2.18}$$

is obtained. Depending on the microstructure of the system, we could for example use a model for densely packed particles, i.e. the crystallites, with the amorphous phase filling the interstices, or a suspension model with the amorphous phase as the particles and the semicrystalline phase as the matrix. In any case, the relevant dynamic modulus ratio is now μ^{*-1}. It is assumed that the amorphous phase essentially consists of voids, so that

$$h_G(1-\phi) \equiv \lim_{|\mu^*|^{-1}\to 0} h_G^*(1-\phi, \mu^{*-1}(\omega))\,. \tag{2.19}$$

An interpolation between the solutions of the small and large volume fraction models is necessary to insure a continuous transition at intermediate volume fractions. A linear interpolation has the general form

$$G^*(\omega,\phi) = \mathcal{F}(\phi)G_0^*(\omega) + \mathcal{H}(\phi)G_1^*(\omega) \tag{2.20}$$

with

$$\mathcal{F}(\phi) = [1 - w(\phi)]\, f_G(\phi) \tag{2.21}$$

and

$$\mathcal{H}(\phi) = w(\phi)h_G(\phi)\,, \tag{2.22}$$

where $w \in [0,1]$ is an empirical weighting function. Tanner [184] determined $\mathcal{F}$ and $\mathcal{H}$ directly, by fitting them to the oscillatory shear data of Boutahar *et al.* [29] for a polypropylene melt containing different volume fractions of spherulites. A qualitative agreement with the shear-induced crystallization experiments of Wassner and Maier [205] was found using these empirically determined interpolation functions. It should be noted that the experiments were limited to very low shear rates $(0.003 \leqslant \dot{\gamma} \leqslant 0.16\,\mathrm{s}^{-1})$.

If $G_1^*(\omega)$ is known and is fitted by a discrete relaxation spectrum of N modes, Eqs. (2.16) and (2.17) are now extended to

$$G'(\omega,\phi) = \mathcal{F}(\phi)\sum_{i=1}^{M} G_{0,i}\frac{\lambda_{0,i}^2\omega^2}{1+\lambda_{0,i}^2\omega^2} + \mathcal{H}(\phi)\sum_{k=1}^{N} G_{1,k}\frac{\lambda_{1,k}^2\omega^2}{1+\lambda_{1,k}^2\omega^2} \tag{2.23}$$

and

$$G''(\omega,\phi) = \mathcal{F}(\phi)\sum_{i=1}^{M} G_{0,i}\frac{\lambda_{0,i}\omega}{1+\lambda_{0,i}^2\omega^2} + \mathcal{H}(\phi)\sum_{k=1}^{N} G_{1,k}\frac{\lambda_{1,k}\omega}{1+\lambda_{1,k}^2\omega^2}\,. \tag{2.24}$$

In both the small volume fraction model and the large volume fraction model, all moduli change by the same amount while the relaxation times do not change. Due to the interpolation, however, the overall relaxation behavior of the material varies with the volume fraction, unless $M = N$ and $\lambda_{0,i} = \lambda_{1,i}$.

Although it is possible to capture, in this rather simple way, the evolution of linear viscoelastic properties during crystallization, we take a different approach. The linear viscoelastic modeling presented here will be extended to the nonlinear viscoelastic regime for application in polymer processing simulations. The interpolation method is not suited to this purpose since the optimal fitting parameters, defining the weighting function $w(\phi)$, probably change with the processing conditions.

Crystallites as deformable particles

In general, if G_1^* is finite, f_G^* is complex and Eq. (2.12) yields for the effective storage modulus

$$G' = \left(f_G' - f_G''\tan\delta_0\right)G_0' \tag{2.25}$$

and for the effective loss modulus

$$G'' = \left(f_G' + \frac{f_G''}{\tan\delta_0}\right)G_0'' \tag{2.26}$$

with $\tan\delta_0 = G_0''/G_0'$ the loss angle of the matrix. The fact that the expressions between parentheses in Eqs. (2.25) and (2.26) are different has an important consequence. Eq. (2.25) can be written as

$$G' = \sum_{i=1}^{M}\left(f_G' - \frac{f_G''}{\lambda_{0,i}\omega}\right)G_{0,i}\frac{\lambda_{0,i}^2\omega^2}{1+\lambda_{0,i}^2\omega^2} \tag{2.27}$$

and Eq. (2.26) as

$$G'' = \sum_{i=1}^{M} \left(f'_G + f''_G \lambda_{0,i}\omega\right) G_{0,i} \frac{\lambda_{0,i}\omega}{1 + \lambda_{0,i}^2\omega^2} \,. \tag{2.28}$$

It is clear that, if the effective relaxation times λ_i are chosen equal to the relaxation times $\lambda_{0,i}$ of the matrix, G' and G'' can only be described by the same spectrum if $f''_G = 0$. All moduli then increase by the same amount f'_G relative to those of the matrix, so that G' and G'' are shifted independent on the frequency, corresponding qualitatively to the behavior of a rigid particle suspension. But $f''_G = 0$ only if μ^* is real, i.e. if G_1^* is proportional to G_0^* so that both have the same frequency dependence, which is not the case in suspensions encountered in practice, nor in crystallizing polymer melts.

If $f''_G \neq 0$, f_G^* must be determined in the whole range of frequencies of interest, given the dynamic moduli $G_0^*(\omega)$ and $G_1^*(\omega)$ of the individual phases. In numerical simulations of crystallization during flow, G^* can at any time step be fitted by a new set of effective moduli and effective relaxation times, using the set from the previous time step as a first estimate. If the number of modes is the same for each phase, they can be expressed in terms of the moduli and relaxation times of the matrix as

$$G_i(\phi) = k_{G,i}(\phi) G_{0,i} \tag{2.29}$$

and

$$\lambda_i(\phi) = k_{\lambda,i}(\phi) \lambda_{0,i} \tag{2.30}$$

with $1 \leqslant k_{G,i} \leqslant G_{1,i}/G_{0,i}$ and $1 \leqslant k_{\lambda,i} \leqslant \lambda_{1,i}/\lambda_{0,i}$. In this way a smooth transition from the matrix spectrum to the particle spectrum is obtained. If the latter consists of $N < M$ modes, while going from $\phi = 0$ to $\phi = 1$, $M - N$ of the initial M modes should vanish. If $N > M$, $N - M$ new modes should appear. To ensure consistency, a single criterion must be used to choose the number of modes in the phase spectra and in the effective spectrum.

Thus we use a single suspension model, in contrast to the interpolation method, where different models are used at small and large volume fractions. Therefore we need a suspension model that is valid in the entire range of volume fractions, as stated in the Introduction. This severely limits the number of suitable models. We will come back to this in Section 2.3.

2.2.2 Nonlinear viscoelastic suspension rheology

The correspondence principle is only valid in the linear viscoelastic regime, since it relies on the fact that the stress evolution is given by a Boltzmann integral [37, 84, 85]. In the context of modeling flow-induced crystallization during processing, nonlinear effects will be important at least in the amorphous phase, where the largest deformations take place. In general, nonlinear viscoelastic constitutive models contain the moduli G_i and the relaxation times λ_i of the linear relaxation spectrum plus a number of additional parameters. We assume that the correspondence principle still applies to the linear viscoelastic part of the rheology. The effective moduli and relaxation times are then related to those of the matrix by Eqs. (2.29) and (2.30), respectively.

Experiments on suspensions of rigid particles in a viscoelastic matrix have shown that the maximum strain amplitude, below which linear viscoelastic behavior is observed, decreases strongly with increasing particle volume fraction [7]. Thus, even though the matrix is linear viscoelastic, at a certain volume fraction the behavior of the suspension will become nonlinear viscoelastic. This phenomenon may also be expected to occur if the particles are not rigid, although to our knowledge no supporting data are available.

The experimental results of Ohl and Gleissle [149] and Mall-Gleissle *et al.* [140], in which suspensions of essentially rigid spheres in viscoelastic matrix fluids were subjected to simple shear flow, show a pronounced influence of the volume fraction on the normal stress differences. It was found that, for constant ϕ, the steady-state first normal stress difference $N_1 = \tau_{11} - \tau_{22}$ correlated with the shear stress as $N_1 \sim \tau_{12}^n$, where $1.63 \leqslant n \leqslant 1.68$. When the volume fraction of particles was increased at a constant value of the shear stress, they saw that the first normal stress difference decreased. This means that the dependence of N_1 on ϕ is weaker than that of τ_{12}^n on ϕ.

Hwang *et al.* [102], who simulated two-dimensional suspensions of rigid discs in an Oldroyd-B fluid, found a similar scaling of the time-averaged steady-state stress functions N_1 and τ_{12} with an exponent $n = 2$. Furthermore, they showed that both the macroscopic shear viscosity $\eta = \tau_{12}/\dot{\gamma}_0$, where $\dot{\gamma}_0$ is the externally applied shear rate, and the macroscopic first normal stress coefficient $\Psi_1 = N_1/\dot{\gamma}_0^2$ increase with $\dot{\gamma}_0$ as well as with ϕ. Mall-Gleissle *et al.* [140] also observed that the magnitude of the second normal stress difference $|N_2| = |\tau_{22} - \tau_{33}|$ increased by the same amount as N_1 upon increasing the volume fraction at constant shear stress. This was not the case in the simulations of Hwang *et al.* [102] because the Oldroyd-B model does not predict a second normal stress difference in planar shear.

The dependence of N_1 and τ_{12} on the volume fraction of particles can be reproduced, at least qualitatively, by assuming that the 'effective' velocity gradient tensor can be written as

$$\boldsymbol{L}(\phi, \dot{\gamma}_0) = k_L(\phi, \dot{\gamma}_0)\boldsymbol{L}_0 \tag{2.31}$$

to take into account that the macroscopic velocity field $\boldsymbol{L}_0$ is locally disturbed by the presence of particles. The undisturbed shear rate, defined as

$$\dot{\gamma}_0 = \sqrt{2\boldsymbol{D}_0 : \boldsymbol{D}_0} \tag{2.32}$$

with $\boldsymbol{D}_0 = \frac{1}{2}\left[\boldsymbol{L}_0 + \boldsymbol{L}_0^T\right]$ the undisturbed deformation rate tensor, together with the volume fraction of particles determines the strength of the disturbances k_L according to Eq. (2.31). To illustrate this phenomenological model of particle-induced nonlinear effects, we choose a single-mode upper-convected Maxwell model. Using Eqs. (2.29), (2.30), and (2.31), the constitutive relation for the extra stress tensor becomes

$$\overset{\triangledown}{\boldsymbol{\tau}} + \frac{1}{k_\lambda \lambda_0}\boldsymbol{\tau} = 2k_G k_L G_0 \boldsymbol{D}_0 \,. \tag{2.33}$$

In a steady-state simple shear flow, Eq. (2.33) yields the shear stress

$$\tau_{12} = k_G k_\lambda k_L G_0 \lambda_0 \dot{\gamma}_0 \tag{2.34}$$

and the first normal stress difference

$$N_1 = 2k_G k_\lambda^2 k_L^2 G_0 \lambda_0^2 \dot{\gamma}_0^2 = \frac{2\tau_{12}^2}{k_G G_0} \,. \tag{2.35}$$

In accordance with the numerical simulations of Hwang *et al.* [102], the first normal stress difference, at a given volume fraction, is proportional to the square of the shear stress. They used an Oldroyd-B model for the matrix, which leads to equivalent results if used in combination with the phenomenological nonlinear viscoelastic model discussed here. Furthermore, also in accordance with these simulations and with the experiments of Mall-Gleissle *et al.* [140], the ratio of the first normal stress difference and the n^{th} power (here $n = 2$) of the shear stress, both normalized by their values at $\phi = 0$, is independent on the shear stress and shear rate:

$$\beta(\phi) = \frac{N_1(\phi, \dot{\gamma}_0)/N_1(\phi = 0, \dot{\gamma}_0)}{\left[\tau_{12}(\phi, \dot{\gamma}_0)/\tau_{12}(\phi = 0, \dot{\gamma}_0)\right]^2} = \frac{1}{k_G(\phi)} \,. \tag{2.36}$$

Figure 2.1 shows how τ_{12} and N_1 change if the volume fraction is increased from ϕ_1 to ϕ_2 while the macroscopic shear rate is kept constant. For rigid particles ($k_\lambda = 1$) not disturbing the macroscopic velocity field ($k_L = 1$), N_1 increases linearly with τ_{12}. However, Hwang et al.'s results indicate that the dependence of N_1 on τ_{12}, upon increasing the volume fraction at a constant shear rate, becomes stronger than linear. Here this deviation is taken into account by the parameter k_L, which is a function of the volume fraction as well as the shear rate. Thus, with this parameter a shear thickening is introduced, which is also in accordance with the simulations of Hwang et al. Moreover, it qualitatively agrees with the experiments of Ohl and Gleissle [149] involving rigid particle suspensions with shear thinning matrix fluids, where the shear thinning effect was observed to decrease with increasing volume fraction at high shear rates.

In order to describe the dependence of N_2 on ϕ, a constitutive model should be chosen which predicts a negative second normal stress difference in simple shear flow. One option is to use

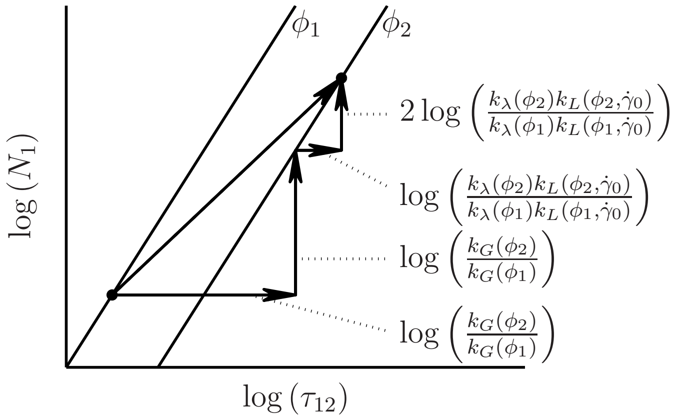
ϕ_1
ϕ_2
$2\log\left(\frac{k_\lambda(\phi_2)k_L(\phi_2,\dot{\gamma}_0)}{k_\lambda(\phi_1)k_L(\phi_1,\dot{\gamma}_0)}\right)$
$\log\left(\frac{k_\lambda(\phi_2)k_L(\phi_2,\dot{\gamma}_0)}{k_\lambda(\phi_1)k_L(\phi_1,\dot{\gamma}_0)}\right)$
$\log\left(\frac{k_G(\phi_2)}{k_G(\phi_1)}\right)$
$\log\left(\frac{k_G(\phi_2)}{k_G(\phi_1)}\right)$
$\log(N_1)$
$\log(\tau_{12})$

Figure 2.1: Schematic drawing of the volume fraction dependence of the first normal stress difference and the shear stress at a macroscopic shear rate $\dot{\gamma}_0$.

a model with a Gordon–Schowalter derivative [124] and a nonzero slip parameter ζ, like the Phan-Thien–Tanner (PTT) model. However, it can be shown that β then depends on the macroscopic Weissenberg number, $Wi_0 = \lambda_0\dot{\gamma}_0$, which contradicts the experimental results. Via a different approach, Tanner and Qi [185] developed a phenomenological nonlinear viscoelastic suspension model, showing reasonable agreement with experimental data for N_1 as well as N_2. The stress tensor in their model consists of two modes. One is described by a PTT model, with $\zeta = 0$ and including a volume fraction dependence of the relaxation time, and the other by a Reiner–Rivlin model with a volume fraction-dependent viscosity. The latter causes the second normal stress difference. A definitive validation of the method proposed here may be possible by starting with more advanced constitutive models, like for example the Rolie-Poly [130], Pom-Pom [142], or XPP [202] models.

As shown in Figure 2.1, shifting the shear stress and the first normal stress difference by $k_G(\phi)$, we should end up on the line with slope n corresponding to the volume fraction ϕ. Hence, experimental data such as those of Mall-Gleissle et al. can be used to validate any combination of a constitutive model for the matrix and a suspension model for the influence of the particles on the effective linear viscoelastic properties. Moreover, numerical results like those of Hwang et al. allow for the independent validation of linear viscoelastic models for suspensions of rigid particles, since the same constitutive model for the matrix can be chosen as in the simulations. Unfortunately, we are not aware of similar experimental or numerical results for deformable particles.

The parameter k_L, which describes the nonlinear viscoelasticity induced by the presence of particles, can be found by fitting it to experimental or numerical data. This procedure is not independent on the constitutive model used for the matrix, because different constitutive models may yield different values for the exponent n. For the upper-convected Maxwell and

Oldroyd-B models, where $n = 2$, we find

$$k_L(\phi, \dot{\gamma}_0) = \frac{N_1(\phi, \dot{\gamma}_0)/N_1(\phi = 0, \dot{\gamma}_0)}{\tau_{12}(\phi, \dot{\gamma}_0)/\tau_{12}(\phi = 0, \dot{\gamma}_0)} \,. \tag{2.37}$$

Figure 2.1 shows that this parameter determines the deviation from the curve $N_1 \sim \tau_{12}$, when the volume fraction is increased at a constant macroscopic shear rate $\dot{\gamma}_0$. Hwang et al. showed the dependence of k_L on the volume fraction and the macroscopic shear rate in their two-dimensional simulations (figure 8 in [102]).

In the following an elastic suspension model, taken from the literature, is transformed to a linear viscoelastic model by means of the correspondence principle. Its predictions are compared qualitatively to the numerical simulations of Hwang *et al.* in Section 2.3.3 and quantitatively to crystallization experiments in Section 2.3.4. A quantitative evaluation of the phenomenological model of nonlinear viscoelastic suspension rheology, discussed above, is beyond the scope of this chapter.

2.3 Evaluation of a linear viscoelastic model

Analytical descriptions of the effects of particles on the rheology of a suspension are generally restricted to isolated particles or to interactions between pairs of particles and are therefore valid only in dilute or semi-dilute conditions, respectively. In the case of a crystallizing polymer melt, however, we need a suspension model that is applicable in the entire range of volume fractions. An appropriate choice might be one of the so-called self-consistent estimates, which have been used for quite some time in the mechanical modeling of elastic composites. Essentially, the effective properties are found as follows. A stress or strain is prescribed at the boundary of a unit cell, which gives a simplified picture of the microstructure. The mechanical response of the unit cell is calculated and when this response becomes homogeneous, the effective mechanical properties are found.

The generalized self-consistent method of Christensen and Lo [38] was claimed by these authors to be valid in the entire range of volume fractions. Furthermore, it gives solutions for suspensions of spherical particles and suspensions of long parallel cylindrical fibers, corresponding to the different microstructures found locally in a crystallizing polymer melt. The generalized self-consistent method thus meets the first two requirements stated in the Introduction. The third and fourth have already been dealt with in Section 2.2. We therefore discuss this model in detail here.

2.3.1 History and relation to other models

The generalized self-consistent method was originally called three-phase model but renamed by Christensen [40] in reference to the self-consistent method [33, 93, 94]. This model, which has an analogy in the theory of heterogenous conducting materials [32], considers a single particle embedded in a homogeneous matrix with the effective properties sought. The generalized self-consistent method, on the other hand, uses a unit cell made up of a particle surrounded by a concentric shell of the matrix material. This coated particle is embedded in the effective homogeneous medium. The difference between the two models can be interpreted as follows: 'While the self-consistent method seeks to predict the interaction of an inclusion and its neighboring microstructure (the combined effect of the matrix and other inclusions), this model includes (in a certain approximate sense) the interaction between the inclusion and the surrounding matrix, as well as the neighboring microstructure' [148]. A coated particle unit cell was used earlier by Fröhlich and Sack [65] for elastic spheres in a viscous matrix, by Oldroyd [150] for viscous drops or elastic spheres in a viscous matrix, by Kerner [114] for elastic spheres in an elastic matrix, and by Hermans [89] for unidirectional elastic fibers in an elastic matrix. Two versions of the generalized self-consistent method exist: a three-dimensional (3D) one in which the particle and matrix domains of the unit cell are concentric spheres and a two-dimensional (2D) one in which they are concentric circles. These give the solutions for spherical particles and long parallel cylindrical fibers, respectively.

Table 2.1 summarizes the main properties of the generalized self-consistent method and some other suspension models. Palierne [153] developed a model for incompressible linear viscoelastic emulsions, in which the drops are at least approximately spherical. For dilute emulsions, he considered a single drop suspended in the effective medium. Not surprisingly, neglecting the effect of surface tension, the result is the same as the analytical solution of the self-consistent method in the dilute limit, taking the matrix as incompressible [93]. In contrast to both the self-consistent and the generalized self-consistent method, the derivation of the non-dilute Palierne model is based on a unit cell in which one particle is at the center of a sphere filled with the matrix and other particles, which in turn is surrounded by the effective medium. If the effect of surface tension is again neglected, it turns out that the result is exactly the viscoelastic analogue of the model of Kerner [114] for all volume fractions [71, 153]. Through a similar derivation for an elastic suspension of spheres, Uemura and Takayanagi [192] also arrived at the same effective shear modulus as Kerner, although a different expression for the effective Poisson ratio was obtained.

Christensen and Lo [38] demonstrated that the elastic shear modulus predicted by the 3D generalized self-consistent method lies between the classical upper [80] and lower bounds [81, 204] for all volume fractions, whereas Kerner's result coincides with the lower bound. Contrary to Palierne's model, the 3D generalized self-consistent method is only equivalent to Kerner's model for vanishing volume fraction of spheres. Whereas Palierne did not consider

Table 2.1: Attributes of some suspension models (SCM: self-consistent method, GSCM: generalized self-consistent method, TOA: third-order assumption). Elastic (E) models can be converted to linear viscoelastic (LVE) models by means of the correspondence principle.

Model	Phases	Particles	Volume fraction	Ref.
SCM	E	spheres	small or large	[93]
		cylinders		[94]
GSCM		spheres cylinders	arbitrary, size distribution should admit $\phi \rightarrow 1$	[38–40]
Torquato, exact		arbitrary	arbitrary	[188]
Torquato, TOA			small to moderate	[189]
Palierne	LVE	spheres	small to moderate	[153]
Bousmina				[27]

drops close to contact with each other, Christensen [40] derived, by physical reasoning similar to that of Frankel and Acrivos [64], the functional form of $f_G(\phi)$ and of the relative transverse shear modulus $f_{G_{23}}(\phi)$ for rigid spheres and unidirectional rigid cylinders, respectively, when $\phi \rightarrow 1$. They were found to agree with the corresponding asymptotic forms of the generalized self-consistent method, for a compressible matrix as well as for an incompressible matrix. Of course the volume fraction can only go to one if the distribution of particle diameters is sufficiently broad, so that small particles can fill the spaces between larger particles.

Bousmina [27] proposed an emulsion model based on the 3D generalized self-consistent method, extending the particle modulus with a term due to surface tension. In the coefficients of the quadratic function, one of whose roots is f_G^* (see Eq. (2.41) later on) only terms of order ϕ were retained. It is therefore not surprising that only small differences with Palierne's model were observed. The expressions for the coefficients given in Bousmina's paper contain a few errors, apparently mostly because he was unaware of an erratum [39] to the original paper on the generalized self-consistent method; the correct expressions are included in Appendix 2A.

Christensen [40] validated the 3D generalized self-consistent method with respect to experimental data on suspensions of rigid spheres. The results proved superior to those of two homogenization schemes widely used at that time, i.e. the Mori–Tanaka method [22] and the differential scheme [159], especially for volume fractions $\phi > 0.4$. However, Nemat-Nasser and Yu [147] pointed out uncertainties in some of the experimental data used for comparison, which were compiled by Thomas [187]. Segurado and Llorca [170] performed 3D numerical simulations of suspensions of spheres in an elastic matrix, where $0 \leqslant \phi \leqslant 0.5$. They compared their results to the predictions of the Mori–Tanaka method, the generalized self-consistent method, and the third-order approximation [189] of an exact series expansion for the effective stiffness tensor of elastic two-phase media [188]. The generalized self-consistent method performed just as well as this third-order approximation when the particles were deformable, except that the effective bulk modulus was predicted slightly more accurately by the third-order approximation. For rigid spheres, the latter also yielded somewhat better results.

Because the generalized self-consistent method is much easier to implement than Torquato's third-order approximation, we will use it to determine the linear viscoelastic properties of a suspension with the aid of the correspondence principle. As explained above, the suspension is represented by a unit cell consisting of a particle and a surrounding matrix shell. Their radii are a and b, respectively. The volume fraction of particles is given by

$$\phi = \left(\frac{a}{b}\right)^3 \tag{2.38}$$

for the 3D coated sphere unit cell and

$$\phi = \left(\frac{a}{b}\right)^2 \tag{2.39}$$

for the 2D coated cylinder unit cell. The unit cell is suspended in an infinitely extending effective medium, which has the effective properties of the suspension. These properties are found when the response of the unit cell to a given load equals the response of the homogeneous effective medium. In the 3D generalized self-consistent method, the relative shear modulus (see Eq. 2.10) is obtained from the quadratic equation

$$A f_G^2 + B f_G + C = 0\,, \tag{2.40}$$

where the coefficients A, B, and C depend on ϕ, μ, ν_0, and ν_1. These coefficients are given in Appendix 2A. The relative bulk modulus was found to be the same as in the composite spheres model of Hashin [80].

For elastic suspensions of long parallel cylindrical fibers, Hashin and Rosen [82] derived the components of the fourth-order stiffness tensor, except the shear modulus in the transverse plane. The 2D generalized self-consistent method gives the relative transverse shear modulus as the solution of a quadratic expression similar to Eq. (2.40), but with different coefficients. These are included in Appendix 2B.

In accordance with the correspondence principle, the relative dynamic modulus is obtained from

$$A^* {f_G^*}^2 + B^* f_G^* + C^* = 0\,, \tag{2.41}$$

where the complex coefficients A^*, B^*, and C^* follow from A, B, and C when μ is replaced by μ^*. For a crystallizing polymer melt, we propose to calculate the effect of the presence of spherulites by means of the 3D generalized self-consistent method, and to use the resulting

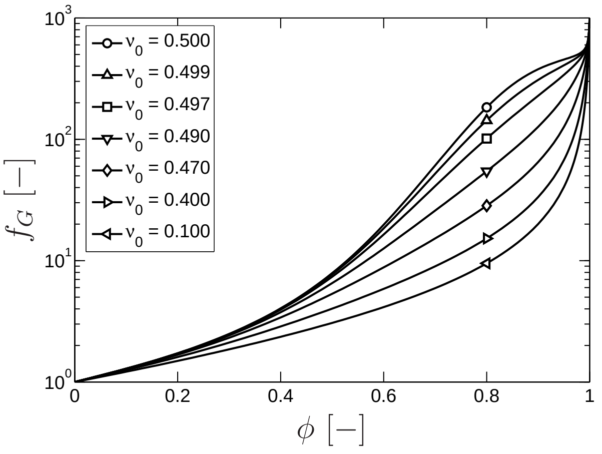

Figure 2.2: Influence of the Poisson ratio of the matrix on the relative modulus of an elastic suspension of spheres ($\mu = 10^3$, $\nu_1 = 0.5$).

effective medium as the matrix in the 2D generalized self-consistent method, which accounts for the influence of oriented crystallites.

2.3.2 Influence of phase properties

First of all, let us take a look at the original 3D generalized self-consistent method for elastic suspensions of spheres, according to which the relative shear modulus f_G is obtained from Eq. (2.40) with real coefficients A, B, and C. The curve of $\log(f_G)$ versus ϕ for $\mu = 10^3$ and $\nu_0 = \nu_1 = 0.5$, plotted in Figures 2.2 and 2.3, has two inflection points: one at $\phi \approx 0.70$ and the other at $\phi \approx 0.95$. In between these points the second derivative is negative,

$$\frac{\partial^2 \log(f_G)}{\partial \phi^2} < 0\,, \tag{2.42}$$

and consequently a 'shoulder' appears in the curve. Beyond $\phi \approx 0.95$, f_G swiftly approaches its final value $f_G(\phi = 1) = \mu$; note that f_G at $\phi = 0.95$ is still smaller than $\mu/2$.

The shape of the relative modulus curve depends most strongly on the Poisson ratio of the matrix and on the modulus ratio. Figure 2.2 shows that, upon lowering ν_0 while keeping $\nu_1 = 0.5$, f_G decreases and the shoulder vanishes quickly: at $\nu_0 = 0.49$ it is not recognizable anymore. Decreasing ν_1 while $\nu_0 = 0.5$ has a much weaker influence on f_G, as seen in Figure 2.3, and the shoulder remains. Thus, even at large volume fractions, compressibility of the matrix has a more profound influence on the results of the 3D generalized self-consistent method than compressibility of the particles. Furthermore, the shoulder diminishes at lower values of the modulus ratio, as shown in Figure 2.4. It should be noted that the logarithmic scale used on the vertical axes of these figures exaggerates the effects mentioned. For the

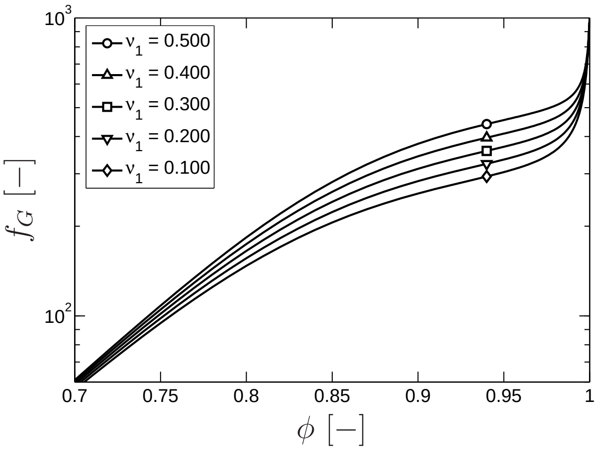

Figure 2.3: Influence of the Poisson ratio of the particles on the relative modulus of an elastic suspension of spheres ($\mu = 10^3$, $\nu_0 = 0.5$).

second derivative of f_G with respect to ϕ one finds

$$\frac{\partial^2 f_G}{\partial \phi^2} < \frac{1}{f_G}\left(\frac{\partial f_G}{\partial \phi}\right)^2 \tag{2.43}$$

if Eq. (2.42) is satisfied. Since the right-hand side of Eq. (2.43) is always positive, when f_G is plotted on a linear scale, a smaller decrease of ν_0 or μ suffices to make the shoulder vanish: it is already gone at a matrix Poisson ratio $\nu_0 = 0.498$ for $\nu_1 = 0.5$ and $\mu = 10^3$, and at a modulus ratio $\mu = 50$ for $\nu_0 = \nu_1 = 0.5$.

To our knowledge, this peculiar feature of the generalized self-consistent method has never been reported before. Looking at the material parameters in previous publications, it is easy to see why. Christensen and Lo [38] simulated suspensions with modulus ratios $\mu = 23.46$ and $\mu = 135.14$. According to Figure 2.4, the latter is high enough to cause an observable shoulder in a suspension with an incompressible matrix, but Christensen and Lo used a matrix with $\nu_0 = 0.35$, which is too low even when $\mu = 10^3$ (Figure 2.2). In the later work of Christensen [40], the compressibility effect was obscured because only rigid particles were considered ($\mu \to \infty$). The high end of the curve is then stretched to infinity, so that the shoulder is smoothed out. Segurado and Llorca [170] used the 3D generalized self-consistent method to simulate both suspensions of rigid spheres and suspensions of deformable spheres. In the latter case, the matrix was again too compressible ($\nu_0 = 0.38$) and the modulus ratio too low ($\mu = 26.83$). But apart from that, the maximum volume fraction used in their calculations was $\phi = 0.5$, which is below the range where the shoulder develops.

When the 2D generalized self-consistent method is used to calculate the relative transverse shear modulus of an elastic fiber-reinforced material, the results show the same dependence on the Poisson ratios and the modulus ratio. Applying the generalized self-consistent method to a suspension of linear viscoelastic materials, the same effects are observed in the storage

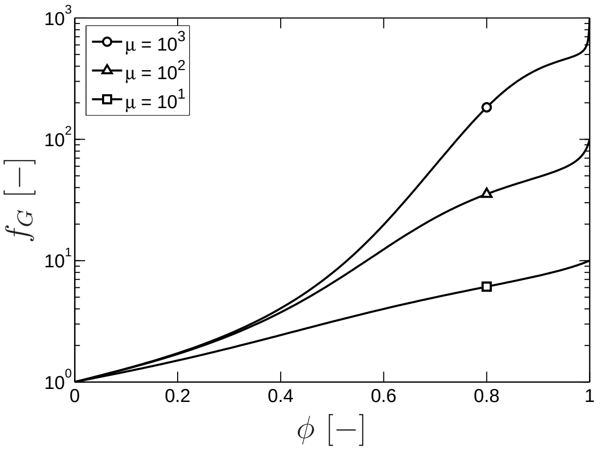

Figure 2.4: Influence of the modulus ratio on the relative modulus of an elastic suspension of spheres ($\nu_0 = \nu_1 = 0.5$).

modulus and the loss modulus.

2.3.3 Comparison to numerical and experimental data

As explained in Section 2.2.2, models for the effects of particles on the linear viscoelastic properties of a suspension, governed by the multipliers $k_{G,i}$ for the modulus and $k_{\lambda,i}$ for the relaxation time, can be validated by numerical simulations. Hwang *et al.* [102] presented results for a sheared 2D system, consisting of rigid discs suspended in an Oldroyd-B fluid. Their simulation method, based on sliding rectangular domains with periodic boundary conditions, was extended to three dimensions to describe suspensions of spherical particles [101]. It was also modified for 2D extensional flow, based on stretching rectangular domains with periodic boundary conditions [103]. An alternative method for 2D extensional flow, using a fixed grid, was developed recently by D'Avino *et al.* [47, 48]. The 2D shear results are considered here. Figure 2.5 shows the time-averaged steady-state first normal stress difference $\langle N_1 \rangle$ versus the steady-state shear stress $\langle \sigma_{12} \rangle$ (σ_{12} is the sum of the viscous mode and the viscoelastic mode in the Oldroyd-B model). Each line corresponds to the simulation results at a constant area fraction of disks, which is equivalent to a volume fraction of infinitely long parallel cylinders, and different shear rates.

Because of the rigidity of the particles, $k_{\lambda,i} = 1$ and $k_{G,i} = f_G$ is a real number, which is obtained from the 2D generalized self-consistent method. Irrespective of the shear rate, shifting $\tau_{12}(\phi = 0)$ to the right and $N_1(\phi = 0)$ upwards by the same factor $f_G(\phi)$, we should end up on the line corresponding to the area fraction ϕ (see Figure 2.1). The symbols in Figure 2.5 indicate the results of the 2D generalized self-consistent method at an arbitrary constant shear rate. It turns out that these agree with the simulations up to $\phi \approx 0.10$. At larger area fractions, the 2D generalized self-consistent method predicts a much stronger

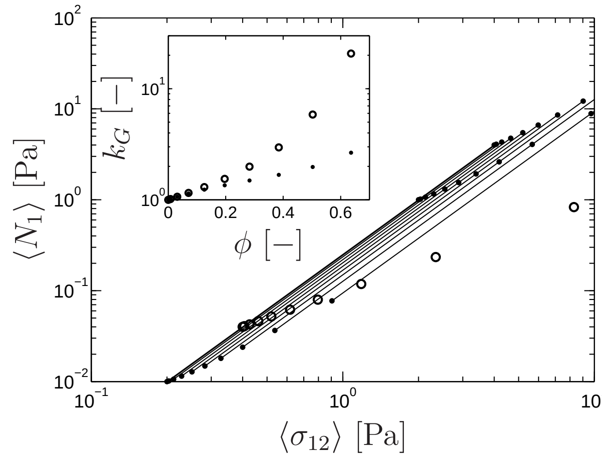

Figure 2.5: Steady-state first normal stress difference and shear stress from simulations (lines, [102]) and from the 2D generalized self-consistent method at an arbitrary shear rate (circles). **Inset:** $k_G(\phi)$ from simulations (dots) and from the generalized self-consistent method (circles). The angle brackets indicate that the steady-state properties were obtained from the simulations by averaging over time.

increase of f_G than the simulations. This is not entirely surprising, since Hwang *et al.* [102] determined the steady-state suspension properties from simulations with a single particle in a periodic domain. The authors already noted that this method does not give realistic results for highly concentrated systems. Nevertheless, an area fraction of ten percent is quite small.

We also compared the predictions of a single-mode upper convected Maxwell model, combined with the 3D generalized self-consistent method, to the experimental data of Mall-Gleissle *et al.* [140]. As seen in Figure 2.6, the data are underpredicted already for $\phi = 0.05$. Better results would probably have been obtained with a more advanced constitutive model. But even for relatively simple ones, like the Giesekus model or the PTT model, no analytical solutions can be derived for τ_{12} and N_1. The relaxation behavior of the matrix has to be known in order to calculate them numerically. Unfortunately, we do not have this information.

2.3.4 Application to crystallization experiments

We looked at two types of rheological measurements on crystallizing polymer melts, in order to investigate whether suspension models can indeed capture the phenomena observed in these experiments. In the first type of experiments, after different short periods of shear, the evolution of the linear viscoelastic properties was followed in time at a constant frequency [J.F. Vega, personal communication, similar to [198] for a different material]. In the second type, the linear viscoelastic properties were measured over a range of frequencies for different constant volume fractions of crystallites [28, 29, 43].

The results from these experiments were used to validate the generalized self-consistent

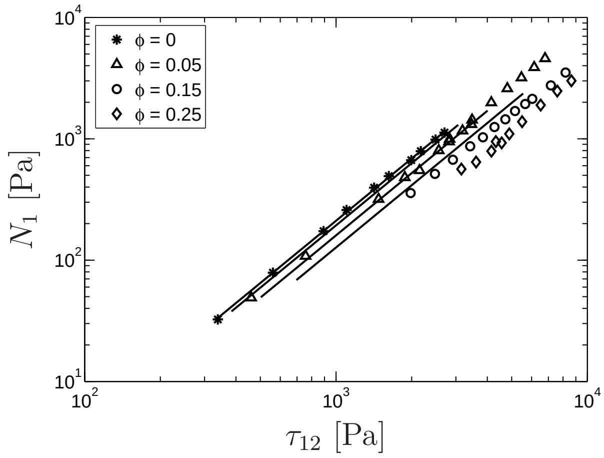

Figure 2.6: Steady-state first normal stress difference and shear stress from experiments (symbols, [140]) and from the 3D generalized self-consistent method (lines).

method as well as the interpolation method, which was described in Section 2.2.1. While the latter treats the highly filled polymer melt as a suspension of amorphous particles in a semicrystalline matrix, the former always takes the crystallites as particles. It has been mentioned in Section 2.3.1 that, in order to allow $\phi \to 1$, the generalized self-consistent method assumes a broad distribution of particle diameters. This is generally not the case in a crystallizing polymer melt, but there complete space filling is achieved in a different way. After impingement of the crystallites, further growth will be restricted to the directions in which amorphous material is still present, until all of it has been incorporated in the semicrystalline phase. Formally, since the crystallites become irregularly shaped, the generalized self-consistent method does not apply anymore. However, we do not expect the rheological properties of a highly concentrated suspension to be very sensitive to variations in particle shape.

Evolution of linear viscoelastic properties after short-term shear

Flow-induced crystallization experiments, carried out in our own group [J.F. Vega, personal communication] are considered first. An isotactic polypropylene melt (HD 120 MO, supplied by Borealis) was subjected to different short periods of shear. Subsequently, its linear viscoelastic properties were monitored in time by means of oscillatory shear measurements. The results are shown in Figure 2.7. It is clear that, immediately after the flow, the dynamic modulus of the material, which was then still largely amorphous, was already increased significantly. The first values of G' and G'' measured after the flow were used as G'_0 and G''_0 in the model calculations. The plateaus of G' and δ, reached in the late stage of

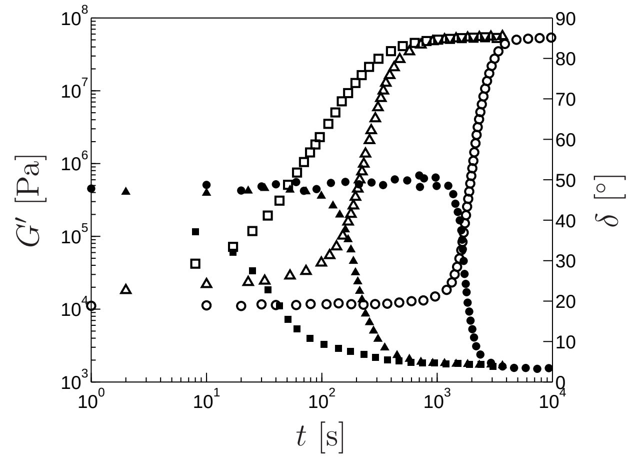

Figure 2.7: Evolution of the storage modulus (open symbols) and loss angle (filled symbols) during crystallization, measured under quiescent conditions (○,●) and after shearing at $\dot{\gamma} = 60\,\mathrm{s}^{-1}$ for $t_s = 3\,\mathrm{s}$ (△,▲) and $t_s = 6\,\mathrm{s}$ (□,■). Part of the data points were omitted for the sake of clarity.

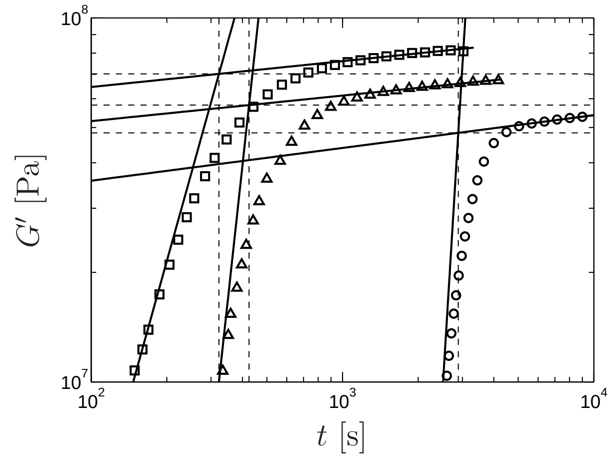

Figure 2.8: Close-up of the storage moduli from Figure 2.7. Part of the data points were omitted and the curves corresponding to $t_s = 3\,\mathrm{s}$ and $t_s = 6\,\mathrm{s}$ were shifted vertically by factors 1.2 and 1.5, respectively, for the sake of clarity. Solid lines: fits of the data in the plateau region and in the region of strong increase of G'. Dashed lines: t_1 and $G'_1(t_1)$.

crystallization, were extrapolated to the earlier stages by the functions

$$G'_1(t) = \begin{cases} G'_1(t_1) & \text{for } t \leqslant t_1 \\ G'_1(t_1)\left[\frac{t}{t_1}\right]^m & \text{for } t > t_1 \end{cases} \tag{2.44}$$

and

$$\delta_1(t) = \begin{cases} \delta_1(t_1) & \text{for } t \leqslant t_1 \\ \delta_1(t_1) + c_\delta \ln\left(\frac{t}{t_1}\right) & \text{for } t > t_1 \end{cases} \tag{2.45}$$

Table 2.2: Parameters for calculating the rheological properties and degree of crystallinity of the semicrystalline phase by means of Eqs. (2.44), (2.45), and (2.6).

t_s [s]	t_1 [s]	$G'_1(t_1)$ [Pa]	$\delta_1(t_1)$ [°]	$\chi_1(t_1)$ [$-$]
0	2.89×10^{3}	4.83×10^{7}	3.48	$-$
3	4.25×10^{2}	4.80×10^{7}	4.83	4.98×10^{-1}
6	3.22×10^{2}	4.68×10^{7}	4.97	5.40×10^{-1}

t_s [s]	m [$-$]	c_δ [°]	c_χ [s^{-1}]
0	9.00×10^{-2}	-1.29×10^{-1}	$-$
3	7.02×10^{-2}	-3.40×10^{-1}	6.67×10^{-5}
6	7.11×10^{-2}	-3.40×10^{-1}	0

and these extrapolations were used as the linear viscoelastic properties of the semicrystalline phase. The values of the parameters in Eqs. (2.44) and (2.45) are given in Table 2.2. The characteristic time t_1, indicating the transition from the space filling stage to the perfection stage, was defined as the intersection of the extrapolated linear fits of the log(G')–log(t) data in these stages, as shown in Figure 2.8.

In the experiments with 3 and 6 seconds of shear, oriented crystallites were observed. There the effect of the spherulites was calculated by the 3D generalized self-consistent method and the resulting effective rheological properties were used as matrix properties in the 2D generalized self-consistent method. The evolution of the volume fraction of spherulites was determined from optical micrographs taken during the flow and the subsequent crystallization [D.G. Hristova, personal communication]. The result for the quiescent melt is shown in Figure 2.9. The volume fraction of oriented crystallites could not be determined accurately in this way. Therefore, the degree of crystallinity χ, derived from in situ wide-angle X-ray diffraction (WAXD) measurements [D.G. Hristova, personal communication], was used to estimate the total semicrystalline volume fraction ϕ. By definition, ϕ and χ are related as

$$\phi(t) = \frac{\chi(t)}{\chi_1(t)}\,. \tag{2.46}$$

The integrated intensities X_{WAXD} of the diffraction peaks, which are normalized by the total integrated intensities, are included in Figure 2.9 for the quiescent and flow-induced crystallization experiments. Comparing the WAXD and optical microscopy results for the quiescent experiment, it is seen that X_{WAXD} is close to but slightly above ϕ up to $\phi = 0.3$. Since the degree of crystallinity is by definition always smaller than the degree of space filling, we conclude that $X_{WAXD} > \chi$. On the other hand, the values of t_1 derived from

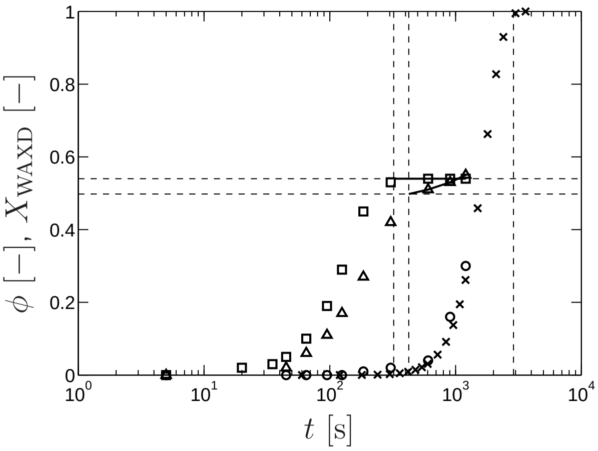

Figure 2.9: Space filling during quiescent crystallization, obtained from optical microscopy (×), along with the integrated WAXD intensity during quiescent crystallization (○) and after shearing at $\dot{\gamma} = 60\,\mathrm{s}^{-1}$ for $t_s = 3\,\mathrm{s}$ (△) and $t_s = 6\,\mathrm{s}$ (□). Solid lines: fits of the WAXD data in the plateau region. Dashed lines: t_1 and $\chi_1(t_1)$.

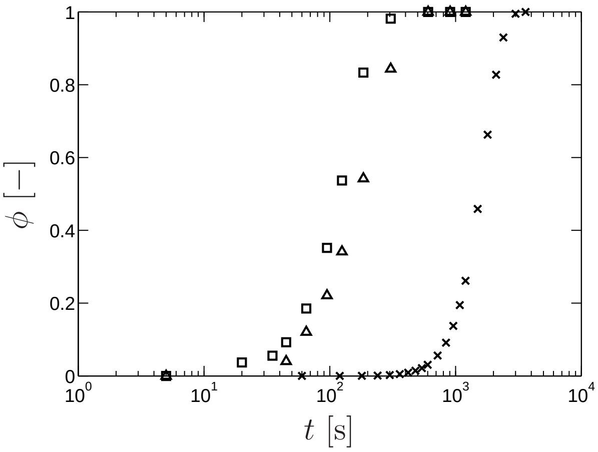

Figure 2.10: Space filling, estimated from WAXD for the flow-induced crystallization experiments, as explained in the text.

the storage modulus measured during flow-induced crystallization (Table 2.2) correlate well with the onset times of the plateaus in the WAXD data. So at least the time scale is correct, provided that t_1 corresponds to $\phi = 1$ as observed in the quiescent crystallization experiment. We assumed X_{WAXD} to be an adequate measure of the internal degree of crystallinity $\chi = \chi_1$ in the plateau region, where the highest signal to noise ratio was obtained. Unfortunately, however, the development of χ and χ_1 during the space filling process could not be reconstructed from these data.

The integrated WAXD intensity in the plateau region was fitted by a linear function of time and extrapolated to obtain $\chi_1(t > t_1)$. We assumed that no secondary crystallization took

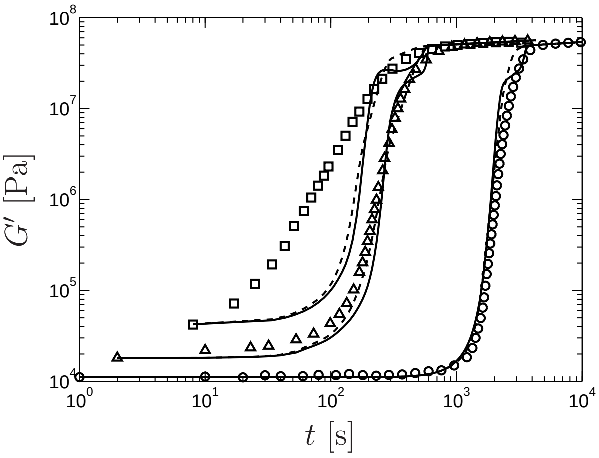

Figure 2.11: Evolution of the storage modulus under quiescent conditions (○) and after shearing at $\dot{\gamma} = 60\,\mathrm{s}^{-1}$ for $t_s = 3\,\mathrm{s}$ (△) and $t_s = 6\,\mathrm{s}$ (□). Dashed lines: interpolation method, Eq. (2.23), with a hyperbolic tangent function for $w(\phi)$. Solid lines: generalized self-consistent method, Eq. (2.41) with the coefficients from Table 2.4 and Eq. (2B7).

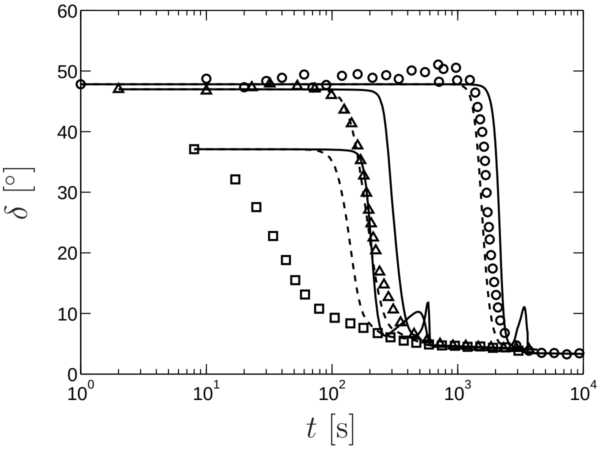

Figure 2.12: Evolution of the loss angle, measured under different conditions and calculated by the interpolation method and the generalized self-consistent method, indicated by the symbols and lines as in Figure 2.11.

place up to $t = t_1$ in any of the experiments considered here, so

$$\chi_1(t) = \begin{cases} \chi_1(t_1) & \text{for } t \leqslant t_1 \\ \chi_1(t_1) + c_\chi\,[t - t_1] & \text{for } t > t_1 \end{cases} . \tag{2.47}$$

Furthermore, for lack of better experimental data, X_{WAXD} was taken as χ and the experimental data were scaled according to Eqs. (2.46) and (2.47) to obtain the total volume fraction. The results are shown in Figure 2.10.

The volume fraction of spherulites ϕ_{sph} was determined from optical microscopy, in the same way as for the quiescent experiment. The volume fraction of spherulites in the amorphous

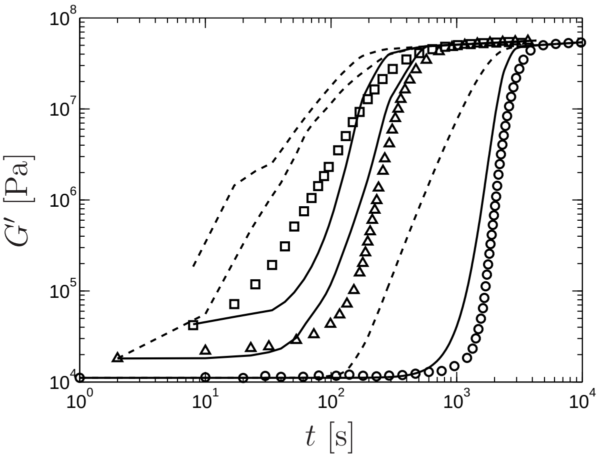

Figure 2.13: Evolution of the storage modulus, measured under different conditions, indicated by the symbols as in Figure 2.11. Dashed lines: linear scaling law, Eq. (2.50). Solid lines: logarithmic scaling law, Eq. (2.51).

phase,

$$x_{sph} = \frac{\phi_{sph}}{1 - \phi + \phi_{sph}} , \tag{2.48}$$

was used in the 3D generalized self-consistent method to calculate the linear viscoelastic properties of the effective matrix in the 2D generalized self-consistent method. There the volume fraction of oriented crystallites,

$$\phi_{ori} = \phi - \phi_{sph} , \tag{2.49}$$

was used to calculate the linear viscoelastic properties of the crystallizing melt.

The results of the generalized self-consistent method are compared to those of the interpolation method in Figure 2.11. The main difference is that $G'(t)$ according to the generalized self-consistent method goes through two inflection points before reaching the plateau $G' = G'_1$. This is due to the shoulder in $f^*_G(\phi)$, as discussed in Section 2.3.2. The shoulder is followed by a decreasing G' for the experiment with 6s of shear. This is caused by our estimate of the volume fraction of oriented crystallites, which goes through a maximum and then drops back to zero. The effect of the shoulder is enhanced when plotting the loss angle, which is more sensitive to changes in the volume fraction (Figure 2.12). For the interpolation method as well as the generalized self-consistent method, the data for the highest shear time are not captured. This can be explained by the lack of information about the shape and orientation of particles in the interpolation method, and by incertainties in the estimate of the oriented volume fraction used in the generalized self-consistent method.

The degree of space filling is often estimated by a linear scaling of the storage modulus

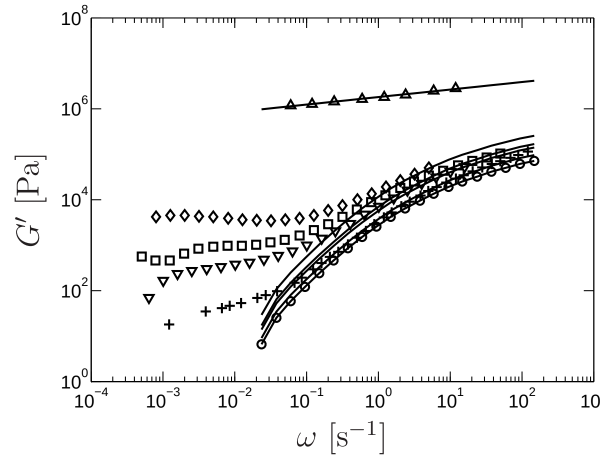

Figure 2.14: Storage modulus measured by Coppola *et al.* [43] for crystallizing melts (open symbols) and an amorphous melt containing glass beads (crosses). Lines: 3D generalized self-consistent method.

[67, 115]. This can be rewritten as

$$G'(t) = G'_0(t) + [G'_1(t) - G'_0(t)]\,\phi(t)\,. \tag{2.50}$$

Figure 2.13 shows that the rheological data are not reproduced from the microscopic images by Eq. (2.50). Also plotted is the logarithmic scaling law,

$$G'(t) = G'_0(t)\left[\frac{G'_1(t)}{G'_0(t)}\right]^{\phi(t)}, \tag{2.51}$$

which was used by Pogodina *et al.* [162]. It performs much better than the linear scaling law, though not as well as the generalized self-consistent method and the interpolation method.

Frequency sweeps at different volume fractions

We first consider the experiments of Coppola *et al.* [43]. They cooled down a poly(1-butene) melt to a temperature T_c below the nominal melting temperature T_m and let it crystallize at T_c for a controlled amount of time. Then they applied an inverse quench [2] to a temperature T_{iq} close to, but still below T_m and measured the rheological properties by means of a multiwave technique, which extended the experimentally accessible range of frequencies down to the order of $10^{-3}\,\mathrm{Hz}$. This revealed that the plateau in the storage modulus, observed at low frequencies, did not continue all the way down to zero, as in a chemical or physical gel, but fell off at a certain frequency. This seems to support the idea that crystallization precursors and/or crystalline nuclei act as physical crosslinks, but are too far apart to form a percolating network [212, 213]. However, if the quiescent crystallization

Table 2.3: Volume fraction of spherulites, as obtained from the linear scaling of $G'(t)$, Eq. (2.50), from differential scanning calorimetry (DSC), and from the 3D generalized self-consistent method (ϕ_{GSCM}) for the two sets of experiments.

Coppola *et al.* [43]		Boutahar *et al.* [28, 29]	
$\phi_{G'(t)}$	ϕ_{GSCM}	ϕ_{DSC}	ϕ_{GSCM}
0.0058	0.25	0.1	0.06
0.0129	0.30	0.2	0.11
0.0280	0.40	0.3	0.16
1	1	0.4	0.23
ϕ_{beads}		0.5	0.32
0.12	0.12	0.6	0.41
		0.7	0.55
		0.8	0.73

process was as usual heterogeneous [59], no new precursors were created. Only existing (dormant) precursors were nucleated, so the plateau in $G'(\omega)$ should already be observed in the amorphous melt, according to this explanation.

The results of Coppola et al. are reproduced in Figure 2.14. Different volume fractions of spherulites were obtained by varying the duration of crystallization at T_c. The rheological properties of the partially crystallized melts were compared to those of an amorphous melt containing, according to the authors, a much larger volume fraction of solid spheres. The effect observed in the low-frequency rheology was much smaller than in the partially crystallized melts, from which the authors concluded that indeed the behavior of the latter cannot be explained by gelation. However, they determined the volume fraction by means of the linear scaling law, Eq. (2.50). Based on the results discussed in the previous section, we believe that the actual volume fraction was much larger and we expect it to be more accurately estimated by the generalized self-consistent method. The results of this model are included in Figure 2.14. The low-frequency behavior is obviously not captured for the partially crystallized melts, nor for the particle-filled melt. Therefore the model is fitted to the data at high frequencies. The volume fractions obtained through both approaches are listed in Table 2.3. According to the generalized self-consistent method, the samples were highly filled with spherulites. Unfortunately, no optical data are available to validate this result.

Experiments on two fundamentally different materials were published by Boutahar *et al.* [28, 29]. One material was a heavily nucleated polyethylene melt, whose morphology looked like that of a colloid. The crystalline nuclei were very small, close together, and highly imperfect. The other was an isotactic polypropylene melt, containing large, well separated spherulites. We will consider the data for this suspension-like material here.

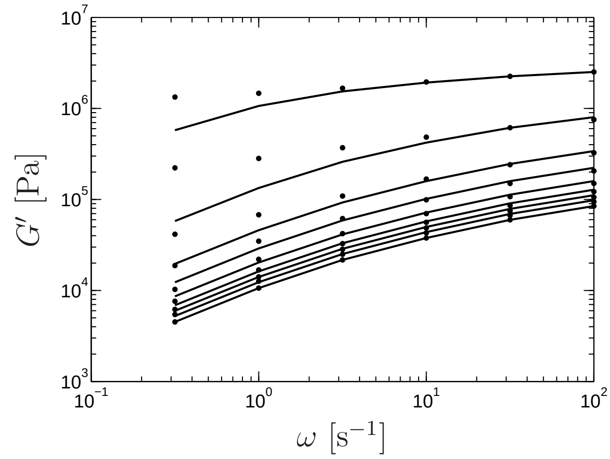

Figure 2.15: Storage modulus measured by Boutahar *et al.* [28, 29] (dots) and obtained from the 3D generalized self-consistent method (lines).

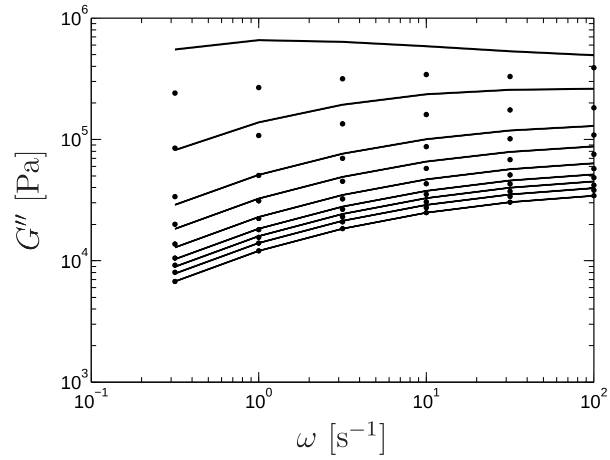

Figure 2.16: Loss modulus measured by Boutahar *et al.* [28,29] (dots) and obtained from the 3D generalized self-consistent method (lines).

The evolution of the storage modulus and the loss modulus is depicted in Figures 2.15 and 2.16, respectively. From Boutahar *et al.* [28], we estimated $G'_1 = 10^7\,\mathrm{Pa}$ and $G''_1 = 6 \times 10^5\,\mathrm{Pa}$. The results are not very sensitive to the values used. Although, at the largest volume fraction, G'' exceeds G''_1 around $\omega = 1\,\mathrm{s}^{-1}$, the absolute value $|G^*|$ is always smaller than $|G^*_1|$, as it should be. The generalized self-consistent method was again fitted to the data at high frequencies. Also for these experiments, the model fails to capture the observed strong increase of the storage and loss moduli with increasing volume fraction at low frequencies. However, the fitted volume fractions correspond very well to the values obtained by Boutahar et al. from differential scanning calorimetry (DSC, Table 2.3).

Modeling of low-frequency suspension rheology

A few models describe the development of a low-frequency plateau in G' and G''. In the Palierne model, it is governed by the surface tension. However, since spherulites behave like solid particles rather than liquid drops, the surface tension is probably negligible in a crystallizing melt, at least for the relatively large volume fractions (corresponding to large radii of spherulites) where the plateau is first observed. Van Ruth *et al.* [197] carried out quiescent crystallization experiments, similar to those of Boutahar *et al.* [28, 29]. They used the Palierne model with an equilibrium modulus,

$$G_{eq} = c\,(\phi - \phi_0)^m \ , \tag{2.52}$$

added to G', which could be fitted to the experimental data with realistic values of the parameters ϕ_0 and m. However, the results of the Palierne model for G'' were not shown. A Cross model was used to fit the dynamic viscosity $|\eta^*|$ for each volume fraction separately.

The self-consistent method predicts a percolation threshold, where the modulus rises or drops steeply, approaching the threshold from below or above, respectively. It diverges to infinity, respectively zero, when both phases are incompressible and the particles are much stiffer than the matrix. This happens at $\phi = 0.4$ for spheres [93] and at $\phi = 0.5$ for cylindrical fibers [94]. When applied to a linear viscoelastic suspension by means of the correspondence principle, the effect is mainly observed at low frequencies as a plateau in G'. This was shown by Wilbrink *et al.* [207]. However, the self-consistent method did not agree quantitatively with their suspensions, for which the percolation threshold was around $\phi = 0.10$.

Albérola and Mélé [5] incorporated the concept of percolation in the generalized self-consistent method. In their modified unit cell, the part of the matrix trapped inside particle clusters is represented by a sphere, which is surrounded by two concentric shells, representing the particles and the non-trapped matrix. This double-coated sphere is surrounded by the effective medium. Hervé and Zaoui [90, 91] extended the generalized self-consistent method to particles coated by an arbitrary number of layers. Their model was used by Albérola et al. to calculate the rheological properties of a suspension with clustering deformable particles. According to the simulation results of Hwang *et al.* [101, 102, 104], extensional stresses between particles in a sheared viscoelastic matrix enhance their tendency to form clusters. Therefore we applied the modified generalized self-consistent method to the experiments described in the previous section. However, it turned out that the percolation threshold shifts f_G^* similarly for all frequencies. Hence the shoulder, observed experimentally at low frequencies, is not reproduced by this model.

2.4 Conclusions

The approach to suspension-based rheological modeling of crystallizing polymer melts, presented in this chapter, has several advantages. Linear viscoelastic suspension models are available to obtain the modulus and relaxation time multipliers $k_{G,i}$ and $k_{\lambda,i}$. These account for the influence of crystallites on the relaxation spectrum used in the constitutive model for the melt. The fact that crystallites can be described as non-rigid particles prevents problems at high degrees of space filling. The phenomenological nonlinear viscoelastic suspension model qualitatively captures phenomena observed in numerical simulations, but is much less expensive computationally and can therefore easily be used in industrial processing simulations. Only standard rheological experiments are needed to quantify the phenomenological parameter k_L.

After considering several linear viscoelastic suspension models, we used the generalized self-consistent method [38–40] because of its simplicity and because, in combination with the nonlinear viscoelastic model, it satisfies all the requirements stated in the Introduction. Combined rheometry and optical microscopy showed that a widely used linear scaling of the storage modulus [67, 115] severely underpredicted the degree of space filling. The generalized self-consistent method described the evolution of linear viscoelastic properties during crystallization rather well, at least at moderate to high frequencies; the low-frequency behavior [28, 29, 43] was not captured. An extension of the generalized self-consistent method, including percolation [5], did not solve this problem; the relative dynamic modulus was merely shifted in a similar manner for all frequencies.

Appendices

2A 3D generalized self-consistent method and Bousmina's linear viscoelastic model

For the 3D generalized self-consistent method, the coefficients are summarized in Table 2.4. Some of the expressions given by Bousmina [27] as first-order approximations of A, B, and C contain errors, most of which are due to misprints in Christensen and Lo [38]. Bousmina's equations 54-59 should read

$$A = K_1\left[24K_2 - 150K_3\phi\right] , \tag{2A1}$$

$$B = \frac{1}{2}K_1\left[9K_2 + 375K_3\phi\right] , \tag{2A2}$$

$$C = \frac{1}{4}K_1\left[-114K_2 - 675K_3\phi\right] , \tag{2A3}$$

$$K_1 = \left[\frac{5}{2}\left(\frac{G_1^* + \alpha/R}{G_0^*} - 8\right)\right. \tag{2A4}$$

$$\left. + \ 7\left(\frac{G_1^* + \alpha/R}{G_0^*}\right) + 4\right] , \tag{2A5}$$

$$K_2 = \left(\frac{G_1^* + \alpha/R}{G_0^*} + \frac{3}{2}\right) , \tag{2A6}$$

$$K_3 = \left(\frac{G_1^* + \alpha/R}{G_0^*} - 1\right) . \tag{2A7}$$

2B 2D generalized self-consistent method

Under the assumption of transverse isotropy, Hooke's law for an elastic fiber suspension can be written in matrix form according to

$$\begin{bmatrix} \tau_{11} \\ \tau_{22} \\ \tau_{33} \\ \tau_{12} \\ \tau_{13} \\ \tau_{23} \end{bmatrix} = \begin{bmatrix} C_{11} & C_{12} & C_{13} & 0 & 0 & 0 \\ C_{12} & C_{22} & C_{23} & 0 & 0 & 0 \\ C_{13} & C_{23} & C_{22} & 0 & 0 & 0 \\ 0 & 0 & 0 & C_{44} & 0 & 0 \\ 0 & 0 & 0 & 0 & C_{44} & 0 \\ 0 & 0 & 0 & 0 & 0 & C_{22} - C_{23} \end{bmatrix} \begin{bmatrix} \epsilon_{11} \\ \epsilon_{22} \\ \epsilon_{33} \\ 2\epsilon_{12} \\ 2\epsilon_{13} \\ 2\epsilon_{23} \end{bmatrix} \tag{2B1}$$

with the index 1 corresponding to the direction of the fiber axes and the indices 2 and 3 corresponding to perpendicular directions in the transverse plane.

Table 2.4: Parameters used in the 3D generalized self-consistent method [38–40].

Shear modulus G, Eq. (2.40)			
$\left.\begin{matrix}A\\B\\C\end{matrix}\right\}$	$= c_1\left(\frac{G_1}{G_0}-1\right)\eta_1\phi^{10/3}+c_2\left[63\left(\frac{G_1}{G_0}-1\right)\eta_2+2\eta_1\eta_3\right]\phi^{7/3}+c_3\left(\frac{G_1}{G_0}-1\right)\eta_2\phi^{5/3}+c_4\left(\frac{G_1}{G_0}-1\right)\eta_2\phi+c_5\eta_2\eta_3$		
with...	... for A:	... for B:	... for C:
c_1	$8\,(4-5\nu_0)$	$-4\,(1-5\nu_0)$	$-4\,(7-5\nu_0)$
c_2	-2	4	-2
c_3	252	-504	252
c_4	$-50\,(7-12\nu_0+8\nu_0^2)$	$150\,(3-\nu_0)\,\nu_0$	$-25\,(7-\nu_0^2)$
c_5	$4\,(7-10\nu_0)$	$-3\,(7-15\nu_0)$	$-\,(7+5\nu_0)$
η_1	$\left(\frac{G_1}{G_0}-1\right)(7-10\nu_0)\,(7+5\nu_1)+105\,(\nu_1-\nu_0)$		
η_2	$\left(\frac{G_1}{G_0}-1\right)(7+5\nu_1)+35\,(1-\nu_1)$		
η_3	$\left(\frac{G_1}{G_0}-1\right)(8-10\nu_0)+15\,(1-\nu_0)$		

Table 2.5: Parameters used in the composite cylinders model [82] and the 2D generalized self-consistent method [38–40].

Longitudinal Young's modulus E_{11}, Eq. (2B9)					
D_1	$1-\nu_1$	D_4	$2\nu_0^2\frac{\phi}{1-\phi}$		
D_2	$\frac{1+\phi}{1-\phi}+\nu_0$	F_1	$\frac{\nu_0\phi\frac{E_1}{E_0}+\nu_1(1-\phi)}{\nu_1\phi\frac{E_1}{E_0}+1-\phi}$		
D_3	$2\nu_1^2$	F_2	$\frac{\nu_1}{\nu_0}F_1$		
Poisson ratio ν_{12}, Eq. (2B11)					
L_1	$2\nu_1\left(1-\nu_0^2\right)\phi+\nu_0\left(1+\nu_0\right)\left(1-\phi\right)$				
L_2	$\left(1-\nu_1-2\nu_1^2\right)\phi$				
L_3	$2\left(1-\nu_0^2\right)\phi+\left(1+\nu_0\right)\left(1-\phi\right)$				
Transverse shear modulus G_{23}, Eq. (2.40)					
A	$3c_1c_2\phi\left(1-\phi\right)^2+\left(c_2\eta_0-c_3\phi^3\right)\left(c_1\eta_0\phi-c_4\right)$				
B	$-6c_1c_2\phi\left(1-\phi\right)^2+\left[c_2\left(\eta_0-1\right)-2c_3\phi^3\right]\left(c_1\phi+c_4\right)$				
C	$3c_1c_2\phi\left(1-\phi\right)^2+\left(c_2+c_3\phi^3\right)\left(c_1\phi+c_4\right)$				
c_1	c_2	c_3	c_4	η_0	η_1
$\frac{G_1}{G_0}-1$	$\frac{G_1}{G_0}+\eta_1$	$\frac{G_1}{G_0}\eta_0-\eta_1$	$\frac{G_1}{G_0}\eta_0+1$	$3-4\nu_0$	$3-4\nu_1$

Hashin and Rosen [82] conveniently selected the following moduli to describe the mechanical behavior of the suspension: the plane-strain bulk modulus

$$K_{23}=\frac{C_{22}+C_{23}}{2}\,, \tag{2B2}$$

the transverse shear modulus

$$G_{23}=\frac{C_{22}-C_{23}}{2}\,, \tag{2B3}$$

the longitudinal shear modulus

$$G_{12}=G_{13}=C_{44}\,, \tag{2B4}$$

the longitudinal Young's modulus

$$E_{11}=C_{11}-\frac{2C_{12}^2}{C_{22}+C_{23}}\,, \tag{2B5}$$

and C_{11}. In the case of a random arrangement of the fibers across the 23-plane they found

$$\frac{K_{23}}{K_0} = \frac{(1+2\nu_0\phi)\frac{K_1}{K_0}+2\nu_0(1-\phi)}{(1-\phi)\frac{K_1}{K_0}+2\nu_0+\phi}, \tag{2B6}$$

$$\frac{G_{12}}{G_0} = \frac{(1+\phi)\frac{G_1}{G_0}+1-\phi}{(1-\phi)\frac{G_1}{G_0}+1+\phi}, \tag{2B7}$$

$$\frac{E_{11}}{E_0} = \left[\left(\frac{E_1}{E_0}-1\right)\phi+1\right] \tag{2B8}$$

$$\times \left[\frac{D_1-D_3F_1+(D_2-D_4F_2)\frac{E_1}{E_0}}{D_1-D_3+(D_2-D_4)\frac{E_1}{E_0}}\right], \tag{2B9}$$

and

$$C_{11} = E_{11}+4\nu_{12}^2K_{23}\,, \tag{2B10}$$

where

$$\nu_{12} = \nu_{13} = \frac{L_1\phi\frac{E_1}{E_0}+L_2\nu_0(1-\phi)}{L_3\phi\frac{E_1}{E_0}+L_2(1-\phi)} \tag{2B11}$$

is the Poisson ratio for uniaxial stress in the direction of the fiber axes. The parameters D_1, D_2, D_3, D_4, F_1, F_2, L_1, L_2, and L_3 depend on the properties of the individual phases and on ϕ and are given in Table 2.5. The same effective properties follow from the 2D generalized self-consistent method, which additionally gives the relative transverse shear modulus G_{23}/G_0 from Eq. (2.40) with the parameters A, B, and C from Table 2.5.

CHAPTER THREE

Local formulation of flow-enhanced nucleation coupled with rheology

---

Abstract

A new modeling framework for flow-enhanced nucleation of polymer melts is introduced. The local influence of flow-induced precursors and nuclei on the rheology of the surrounding melt and, consequently, on the creation of new flow-induced precursors is described as well as convection of these species in flow. A preliminary test of this framework, with respect to a small set of experimental data, shows that it should be improved. Nevertheless, the experimental observation that the number density of spherulites is determined by the strength and duration of flow, remaining essentially constant afterwards, follows naturally from the local formulation including convection, in contrast to the more empirical model in Chapter 4, where this phenomenon is enforced in an artificial way.

3.1 Introduction

A considerable amount of experimental work has been done, especially over the course of the last decade, to unravel the origins of the phenomena observed in flow-induced crystallization (FIC) of polymers; see for example the recent reviews by Kumaraswamy [122] and Somani *et al.* [174]. From the point of view of predicting structure formation and the resulting properties of semicrystalline polymers, there is a need for improved models. The results of the experimental work mentioned are of direct importance in this respect, since the FIC models proposed so far exhibit essential differences in their key assumptions. Crystallizing melts have been described as molecular mixtures [34, 52–57, 193, 196], as suspensions [28, 29, 35, 183, 184], and as physically crosslinking networks [95, 96, 160–163, 208] or locally physically crosslinking melts [157, 158, 182, 212, 213].

In contrast to the molecular mixture concept, the picture of a suspension is in better agreement with the commonly observed microstructure, which consists of large-scale crystallites dispersed throughout an amorphous matrix. It has been shown in Chapter 2 that the linear viscoelastic behavior of crystallizing melts with a spherulitic morphology can be described by a simple suspension model, except at low frequencies. Elevated storage and loss moduli, observed immediately after strong short-term flow [97, 198], cannot be explained based on space filling, as for example with a suspension model. The flow in such experiments is generally applied above the nominal melting temperature or in the early stage of crystallization, when the volume fraction of transformed material is negligible. The change in the initial rheological properties occurs in conjunction with the transition to oriented crystallization [97]. This transition, and the increase in number density of pointlike nuclei, which already takes place under less severe flow conditions, must originate from structural changes in the amorphous phase, although in a later stage typical suspension effects, such as increased molecular stretch between particles, could play a role [104].

In an attempt to illustrate this, Coppola *et al.* [43] carried out rheological measurements on isotactic poly-1-butene (iPB) samples with different constant volume fractions of spherulites as well as on amorphous iPB filled with glass beads. The experimental procedure for the semicrystalline melts consisted of cooling them to a constant temperature $T_c < T_m$, where T_m is the nominal melting point, staying at that temperature for a certain waiting time, then applying the inverse quenching technique [2] to 'freeze in' the semicrystalline morphology, and performing oscillatory rheometry at $T_c < T_{iq} < T_m$. This was done for different waiting times, i.e. different amounts of space filling. The storage modulus increased relative to that of the purely amorphous melt, already by a greater amount for the most weakly crystalline melt, containing 0.58 volume percent spherulites according to the authors, than for the particle-filled melt, containing 12 volume percent glass beads. However, the fraction of spherulites was estimated by a linear normalization of the storage modulus, measured at a fixed frequency, between the values at zero and maximum crystallinity. Volume fractions higher than that of the glass beads (and 14 to 43 times higher than the values obtained by linear normalization of $G'(t)$, see Table 2.3) were predicted by the linear viscoelastic suspension model used in Chapter 2. This model was validated by optical microscopy and DSC measurements of Boutahar *et al.* [29]. Moreover, as Coppola *et al.* pointed out themselves, the increase of the storage modulus as a function of time depends on the frequency. Any scaling method is therefore ambiguous when measurements at different frequencies are considered.

Network formation in the amorphous phase was proposed by Winter and coworkers [95, 96, 160–163, 208]. In their experiments, the rheology of different polymers, prior to impingement of crystallites, looked similar to that of a chemical gel: a plateau in G' developed at low frequencies. In the rheological measurements of Coppola *et al.* [43], discussed above and shown in Figure 2.14, the plateau fell off at a previously unaccessible low frequency. This implies that the gel-like behavior is the result of an evolving slow relaxation process. It is unclear whether this is related to the crystallites acting as particles or to structure formation in the amorphous phase. It is worthwile to repeat the experimental protocol of Coppola *et al.* with shorter times of crystallization at T_c, so that the melts after inverse quenching to T_i are indeed in the early stage, where suspension effects are negligible. Nevertheless, since the average distance between spherulites in the experiments of both groups [43, 95, 96, 160–163, 208] is huge compared to the size of a single molecule, the formation of a percolating network is highly unlikely [107, 108].

Zuidema *et al.* [212, 213] developed a FIC model, in which both the creation and the longitudinal growth of threadlike nuclei were driven by the recoverable strain of the high-end tail of the molecular weight distribution. This was quantified by the second invariant of the deviatoric elastic Finger strain tensor, or equivalently the conformation tensor, of the slowest mode in a multi-mode rheological constitutive equation. The relaxation time of this mode was taken proportional to the number density of flow-induced nuclei, based on the idea that these act as physical crosslinks if different molecules are involved in each nucleus. The model thus captures, in an averaged sense, the strong influence of high-molecular weight (HMW) chains on the overall rate of crystallization [18, 88, 146, 171, 203, 210] and the formation of an oriented morphology [1, 195]. Reasonable agreement with pressure-driven flow experiments of Jerschow [111] was obtained in terms of the transitions between morphological layers. A recent modification of the model by Custódio *et al.* [44] was validated in more detail with respect to injection molding prototype flows. The most striking result was that the onset of an experimentally observable oriented skin layer could be correlated with a critical relative volume fraction of oriented crystalline material, for which the same value was computed in isothermal as well as in nonisothermal simulations.

The hypothesis that nuclei act as physical crosslinks, which was a key element of the successes of the recoverable strain-based FIC model, remains unproven. Swartjes [181] and Sentmanat [172] reported a slower relaxation of the stress after fast short-term flow of undercooled melts. But it is not sure whether the amount of HMW chains involved in nuclei (at least in those that actually become spherulites, which is a very small fraction of all molecules [107, 108]) can explain this phenomenon, which may also be caused by shish formation. Coppola *et al.* [43] suggested that the evolution of a slow relaxation process in their inverse-quenched melts might be interpreted as evidence in favor of Zuidema *et al.*'s hypothesis. However, again referring to Chapter 2, the samples were more highly filled than estimated by the authors, so the behavior observed may have been due to the spherulites acting as fillers rather than physical crosslinks. Moreover, since the number density of quiescent spherulites well below the nominal melting point only depends on the temperature [59], it is believed that quiescent nuclei are intrinsically present in the melt. From this point of view, no new nuclei were made in the experiments of Coppola *et al.* unless sporadic nucleation became significant at the temperature T_{iq} where the rheological measurements were performed, which was only slightly below the nominal melting point.

Several other FIC models with different levels of description exist. Examples are the continuum thermodynamics-based approaches of Doufas *et al.* [34, 52, 53] and Van Meerveld *et al.* [193, 196], the introduction of a flow-induced free energy change in the Doi–Edwards model by Grizzuti and coworkers [3, 42], and kinetic Monte Carlo simulations by Graham and Olmsted [73, 75]. All these models describe an effect of molecular orientation and/or stretch on the kinetics of nucleation, but none of them contain an effect of nuclei on the (local) relaxation dynamics. Doufas *et al.* and Van Meerveld *et al.* did incorporate changes in the rheology as a function of the degree of crystallinity or space filling, respectively, but these effects do not play a role in the early stage of crystallization. In general, agreement with FIC experiments was obtained in terms of the change in time scale of crystallization. Only the simulations of Graham and Olmsted were validated with respect to direct morphological evidence, namely with microcopic observations of the number density of spherulites during continuous shear flow [41]. The shear rates in these experiments were very low, up to $\dot{\gamma} = 0.3\,\mathrm{s}^{-1}$. Under much more severe flow conditions, the coupling between nucleation and the relaxation dynamics of the HMW fraction of the melt, as offered by the recoverable strain-based FIC model, was necessary to predict oriented structure development [44, 212, 213]. It will be shown in Chapter 4 that this also holds for the spherulitic crystallization in moderate to strong flows. Therefore we focus on the recoverable strain-based model and try to adapt it to flow-enhanced pointlike nucleation.

3.2 Objective and outline

Physical crosslinking in the early stage of FIC was hypothesized by Zuidema *et al.* [212, 213] and in later work from the same group [44, 157, 158, 182] without providing a detailed theoretical argumentation. It was mainly an empirical way to capture the highly nonlinear effects of the rate and duration of flow on (in their case oriented) structure formation. Following the basic hypothesis, the probability of nucleation in the immediate vicinity of already existing nuclei is higher than in the bulk of the amorphous melt. Reasoning further

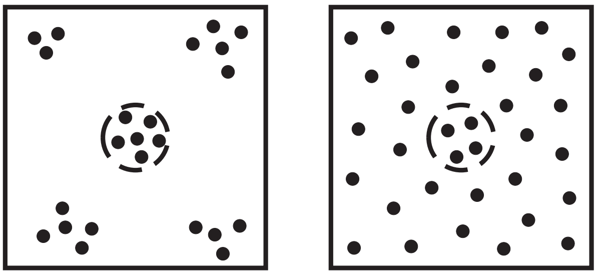

Figure 3.1: Preferential creation of flow-induced precursors in each other's vicinity. **Left:** Structure requiring a local description. **Right:** Structure allowing a global description.

along this line, one has to conclude that nuclei appear in clusters, as depicted on the left side of Figure 3.1. If the relaxation times of chains within these clusters are increased, since they are connected by nuclei, then this increase should not depend on the global number density of flow-induced nuclei, as Zuidema *et al.* proposed, but on the local number within each cluster. Only if the entire space is covered by clusters, as depicted on the right side of Figure 3.1, the local number density within one of these (indicated by the circle) equals the global number density. Taking a typical value of $N_n \sim 10^{15}\,\mathrm{m}^{-3}$ nuclei for isotactic polypropylene [59], we obtain for the average distance between these nuclei $d_{avg} = N_n^{-1/3} \sim 10\,\mu\mathrm{m}$. This is three orders of magnitude higher than the radius of gyration [17], which is a reasonable measure for the range of influence of a nucleus, hence for the size of a cluster. A more detailed analysis is given in Section 3.5, but it is clear that the right side of Figure 3.1 does not correspond to experimental nucleation densities.

The objective of this chapter is to test the hypothesis that flow-induced nuclei locally act as physical crosslinks. We start with the necessary theoretical background on rheology and spherulitic structure formation in Sections 3.3 and 3.4, respectively. In Section 3.5 a local formulation of flow-enhanced nucleation is developed, where the relaxation times (reptation time and stretch relaxation time) of the HMW fraction are related to the local number of nuclei in a cluster. Results of this model are compared to a small set of experimental data. The conclusions are summarized in Section 3.7.

3.3 Rheological modeling

The Cauchy stress tensor for a polymer melt is written in the form

$$\boldsymbol{\sigma} = -p\boldsymbol{I} + \sum_{i=1}^{M} G_i \left(\boldsymbol{B}_{e,i} - \boldsymbol{I}\right) , \tag{3.1}$$

Table 3.1: Slip tensors of the Giesekus [69, 70], XPP [202], and Rolie-Poly [130] models.

	$\boldsymbol{A}_i = c_{1,i}\boldsymbol{B}_{e,i} + c_{2,i}\boldsymbol{B}_{e,i}^{-1} + c_{3,i}\boldsymbol{I}$		
	$c_{1,i}$	$c_{2,i}$	$c_{3,i}$
Giesekus	$\frac{\alpha_i}{2\lambda_{d,i}}$	$-\frac{(1-\alpha_i)}{2\lambda_{d,i}}$	$\frac{1-2\alpha_i}{2\lambda_{d,i}}$
XPP	$\frac{\alpha_i}{2\lambda_{0b,i}}$	$-\frac{(1-\alpha_i)}{2\lambda_{0b,i}}$	$\frac{1-\alpha_i-3\alpha_i\Lambda_i^4\boldsymbol{S}_i:\boldsymbol{S}_i}{2\lambda_{0b,i}\Lambda_i^2} + \frac{1}{\lambda_{s,i}}\left(1-\frac{1}{\Lambda_i^2}\right)$
Rolie-Poly	0	$-\frac{1}{2\lambda_{d,i}} - \frac{\beta_i\Lambda_i^{2\delta_i}}{\lambda_{R,i}}\left(1-\frac{1}{\Lambda_i}\right)$	$\frac{1}{2\lambda_{d,i}} + \frac{1+\beta_i\Lambda_i^{2\delta_i}}{\lambda_{R,i}}\left(1-\frac{1}{\Lambda_i}\right)$

where $i = M$ indicates the mode with the longest relaxation time. The elastic Finger tensor $\boldsymbol{B}_{e,i}$ of mode i follows from

$$\overset{\triangledown}{\boldsymbol{B}}_{e,i} = -\boldsymbol{A}_i \cdot \boldsymbol{B}_{e,i} - \boldsymbol{B}_{e,i} \cdot \boldsymbol{A}_i^T \, . \tag{3.2}$$

The triangle denotes the upper convected derivative and $\boldsymbol{A}_i$ is the slip tensor of mode i, which describes the non-affine deformation of the corresponding molecules. Several constitutive models can be written in this form with different expressions for $\boldsymbol{A}_i$ [156]. Just a few, referred to in this thesis, are listed in Table 3.1.

The elastic Finger tensor is taken equivalent to the conformation tensor, following Leonov [126–128]. The orientation tensor

$$\boldsymbol{S}_i = \langle \vec{n}_i \vec{n}_i \rangle = \frac{\boldsymbol{B}_{e,i}}{\mathrm{tr}\left(\boldsymbol{B}_{e,i}\right)} \tag{3.3}$$

gives the average molecular orientation; $\vec{n}_i$ is a unit vector, tangent to the primitive path of a chain, and the angle brackets indicate an average over the orientation distribution. If the stretch of the primitive path is assumed homogeneous, it is described by the scalar stretch parameter

$$\Lambda_i = \sqrt{\frac{\mathrm{tr}\left(\boldsymbol{B}_{e,i}\right)}{3}} \, , \tag{3.4}$$

which follows from $\boldsymbol{B}_{e,i} = 3\Lambda_i^2 \boldsymbol{S}_i$ [164].

The Rolie-Poly model [130] is used throughout this thesis. More advanced rheological constitutive models, like the Graham–Likhtman and Milner–McLeish (GLaMM) model [72], of which Rolie-Poly is a simplified version, and the slip-link model [167] offer more detail, for example a stretch increasing from the ends of a molecule to the center, but are computationally more expensive.

3.4 Spherulitic structure formation

We focus on spherulitic crystallization. The evolution of the morphology then follows from the rate equations derived by Schneider *et al.* [168],

$$\begin{aligned}
\dot{\Psi}_3 &= 8\pi \dot{N}_n & (\Psi_3 &= 8\pi N_n)\,, & (3.5)\\
\dot{\Psi}_2 &= \dot{R}\Psi_3 & (\Psi_2 &= 8\pi R_{tot})\,, & (3.6)\\
\dot{\Psi}_1 &= \dot{R}\Psi_2 & (\Psi_1 &= S_{tot})\,, & (3.7)\\
\dot{\Psi}_0 &= \dot{R}\Psi_1 & (\Psi_0 &= V_{tot})\,. & (3.8)
\end{aligned}$$

All quantities in these equations are expressed per unit volume in the hypothetical case of unrestricted nucleation and growth, meaning that nuclei can appear in the space already covered by the semicrystalline phase and that spherulites can grow through each other unhindered; N_n is the number of nuclei, R_{tot} is the sum of the radii of the spherulites, S_{tot} is their total surface area, V_{tot} is their total volume, and $\dot{R}$ is the lamellar growth rate. The degree of space filling ϕ, i.e. the real total volume of the semicrystalline phase per unit volume of the material, is obtained from the Kolmogorov–Avrami model [8–10, 117],

$$\phi = 1 - e^{-\Psi_0}\,. \tag{3.9}$$

For a recollection of Kolmogorov's derivation, see Ref. [59]. The real nucleation density follows from

$$N_{n,real}(t) = \int_{-\infty}^{t} \dot{N}_n(s)\left[1-\phi(s)\right] ds\,. \tag{3.10}$$

Eder and coworkers [58, 129] developed a similar set of differential equations for the evolution of the oriented shish-kebab morphology, in which the rates of creation and longitudinal growth of threadlike nuclei were assumed proportional to the square of the shear rate. Zuidema *et al.* [212, 213] adopted this model, but replaced the shear rate dependencies by linear functions of the second invariant of the deviatoric elastic Finger tensor, associated with the longest relaxation time,

$$\begin{aligned}
J_2\left(\boldsymbol{B}^d_{e,M}\right) &= \frac{1}{2}\boldsymbol{B}^d_{e,M} : \boldsymbol{B}^d_{e,M}\,, & (3.11)\\
\boldsymbol{B}^d_{e,M} &= \boldsymbol{B}_{e,M} - \frac{1}{3}\mathrm{tr}\left(\boldsymbol{B}_{e,M}\right)\boldsymbol{I}\,, & (3.12)
\end{aligned}$$

thus focusing on the molecules in the flow, rather than on the flow itself. This invariant, which they obtained from a multi-mode Leonov model, is a measure of the conformation, i.e. orientation and stretch, of the high molecular weight (HMW) chains in the melt.

The modified Eder rate equations were used in parallel with the Schneider rate equations. Specifically, spherulitic and oriented nucleation and growth were supposed to be additive in terms of their unrestricted volume fractions: $\Psi_0 = \Psi_{0,sph} + \Psi_{0,ori}$. The effect of flow on the spherulitic crystallization process was thus not described. Peters *et al.* [157] and Swartjes *et al.* [182] used the XPP model in the same FIC framework, called the SJ$_2$ model (i.e. Schneider-J$_2$).

It has been known for a long time that the HMW fraction of a polydisperse melt most strongly affects the acceleration of crystallization by flow [203] and the transition from spherulitic to oriented morphology [1]. Studies on bimodal blends [18,20,88,146,171,210] have confirmed the role of HMW chains in the formation of threadlike nuclei. Interestingly, the fact that the shish structure consists of chains of all lengths [116] suggests that only the nucleation rate (and/or the initiation of longitudinal growth from a pointlike nucleus) primarily depends on the conformation of the HMW fraction. Therefore, in the recent extension of the SJ$_2$ model by Custódio *et al.* [44], the effect of flow on the longitudinal growth rate was formulated in terms of the average conformation.

3.4.1 Precursors of crystalline nuclei

The physics of early-stage crystallization are still a matter of debate. For example, Olmsted *et al.* [151] suggested that a *bicontinuous* structure of amorphous and mesomorphic domains is formed by spinodal decomposition and that crystallization occurs in the more dense, conformationally ordered mesophase. Strobl [177–179] developed a fundamentally different theory, based on lateral growth and simultaneous thickening of *isolated* mesomorphic layers. Crystallization occurs where the layer thickness exceeds a critical size, resulting in a granular structure and eventually a fully crystalline lamella. Both views have been challenged by Lotz [132,133]. Based on the helical handedness in thin crystalline films of chiral polymers, he advocated the classical nucleation and growth theory [125]. According to Cheng and Lotz, however, the purely enthalpic nucleation barrier in the classical theory should be modified to include entropic effects [36].

Ryan and coworkers [86, 87, 165, 186] analyzed several polymers in terms of the Cahn–Hilliard theory of spinodal decomposition. From small-angle X-ray scattering (SAXS) patterns during quiescent and flow-induced crystallization, they determined the growth rate of density fluctuations as a function of the magnitude of the scattering vector, $k = |\vec{k}|$. Typical Cahn–Hilliard behavior was observed, except for small k, which was attributed to interference from stray light [21]. However, Muthukumar and Welch [145] found the same behavior with Langevin dynamics simulations, from which they concluded that the underlying process was not spinodal decomposition. Based on structural observations in these simulations, Muthukumar [144] derived an alternative expression for the growth rate of density fluctuations. Although it may be seen as an improvement, the author's claim that the new model is 'fully consistent' with the experiments and simulations mentioned, is not supported. (Compare the theoretical growth rate of density fluctuations in Fig. 2 of [144] to the numerical result in Fig. 4 of [145].)

It must be noted that Muthukumar and Welch used a single-chain description. Simulations with multiple chains were discussed in an earlier paper by Liu and Muthukumar [131] but were not analyzed in terms of density fluctuations. However, molecular dynamics simulations by Gee *et al.* [68] qualitatively confirmed the single-chain Langevin dynamics results of Muthukumar and Welch. Curiously, Gee *et al.* interpreted this as a confirmation of the spinodal-assisted crystallization model.

Baert and Van Puyvelde [15] reviewed small-angle light scattering (SALS) studies of polymer crystallization. These typically exhibit density fluctuations in the early stages, whereas orientation fluctuations are observed significantly later. Combining SALS with polarized optical microscopy during flow-induced crystallization of poly-1-butene, Baert and Van Puyvelde showed that the onset of density fluctuations coincided with the appearance of spherulites. From the absence of orientation fluctuations in these early stages, they concluded that the spherulites initially had a low crystalline content. Their results are indicative of nucleation, followed by growth and perfection of the internal structure of the spherulites, rather than spinodal decomposition into a dense mesophase.

Panine *et al.* [154, 155] reported simultaneous SAXS and wide-angle X-ray diffraction (WAXD) measurements during quiescent crystallization of isotactic polypropylene, using a very sensitive wide-angle detector. Sharp WAXD peaks, corresponding to the crystalline α phase, developed around the same time as SAXS. Previous studies had shown a time lag between SAXS and WAXD and incited a discussion whether this was due to the lower sensitivity of the latter or a fingerprint of spinodal decomposition [87]. The results of Panine *et al.* do not agree with the spinodal decomposition model, but suggest that crystalline nuclei are formed in the amorphous phase.

In the case of oriented crystallization, the combined SAXS and WAXD measurements of Balzano *et al.* [19] show that, at high shear rates, crystalline fibrillar nuclei are already formed during flow, whereas at lower shear rates, only metastable fibrillar precursors appear during flow, which nucleate after cessation of flow.

We use the term precursor to refer to a subcritical nucleus. Details of the structure of precursors, i.e. their degree of crystallinity, the number of chain segments involved, and the number of molecules to which these segments belong, are not considered. It is assumed that a precursor may nucleate due to a fluctuation in its size. As will become clear in Section 4.3.1, flow has a severe effect on this process. For detailed simulations of nucleation in flow, we refer to Graham and Olmsted [73, 75]. In our model, the number of precursors obeys the evolution equation

$$\dot{N}_p = I_p + \dot{T}\frac{\partial N_p}{\partial T} - \frac{N_p}{\tau_{pn}} - \frac{N_p}{\tau_{pd}}\,, \tag{3.13}$$

where the dot denotes the material time derivative and I_p corresponds to the mentioned sporadic creation process, driven by thermal fluctuations. The second term on the right-hand side represents athermal activation [63]. This is not due to fluctuations, but involves dormant precursors, which only become active (i.e. able to nucleate) when the temperature is lowered sufficiently. The third term is the nucleation rate and the fourth represents an additional process through which precursors may disappear, namely dissolution into the disordered bulk of the melt. The parameters τ_{pn} and τ_{pd} are characteristic time scales associated with these processes.

The nucleation rate is thus related to the number of precursors according to the expression

$$\dot{N}_n = \frac{N_p}{\tau_{pn}}\,, \tag{3.14}$$

which was introduced by Avrami [8]. However, in his theory, N_p only changes due to nucleation; no new precursors are created and the existing ones do not dissolve.

3.4.2 Quiescent and flow-induced precursors

The total number of precursors consists of 'quiescent' precursors, i.e. those that would have been obtained after the same temperature history but without any deformation history, and flow-induced precursors:

$$N_p = N_{pq} + N_{pf}\,. \tag{3.15}$$

Nuclei are divided into quiescent and flow-induced nuclei accordingly and the corresponding nucleation rates are

$$\dot{N}_n = \dot{N}_{nq} + \dot{N}_{nf} = \frac{N_{pq} + N_{pf}}{\tau_{pn}}\,. \tag{3.16}$$

We assume that $\dot{N}_{pf}$ is independent on $\dot{N}_{pq}$, so that both are described by uncoupled expressions analogous to Eq. (3.13) and the corresponding nucleation rates in Eq. (3.16) are also uncoupled. In this respect, our model differs from that of Coppola *et al.* [42]. They proposed an additive decomposition of the free energy difference between the phases into a quiescent term and a flow-induced term, $\Delta G = \Delta G_q + \Delta G_f$. This was inserted in the classical nucleation theory, where $\dot{N}_n$ is an exponential function of ΔG. Thus the quiescent and flow-induced nucleation rates are inseparable; $\dot{N}_{nf}$ depends on ΔG_q and hence on $\dot{N}_{nq} = \dot{N}_n\,(\Delta G_f = 0)$.

In quiescent melts at high degrees of undercooling, N_{nq} is a unique function of the temperature [59]. In the context of our model, this means that only athermal precursors are formed ($I_p = 0$) and that these are immediately nucleated ($\tau_{pn} = 0$). Eqs. (3.13) and (3.14) can then be rewritten into the single expression $\dot{N}_n = \dot{T}\partial N_p/\partial T$; see Appendix 3A. The minimum temperature for sporadic nucleation was estimated by Janeschitz-Kriegl to lie approximately 50K below the equilibrium melting point for isotactic polypropylene, which corresponds to the nominal melting point of this material (typically between 160 and 165°C) [105, 106, 108].

In this chapter, the sporadic creation of quiescent precursors is not taken into account. This is reasonable for most processing applications and common experimental protocols, where the corresponding regime of low degrees of undercooling is passed by very rapidly. Eq. (3.13) is then split into

$$\dot{N}_{pq} = \dot{T}\frac{\partial N_{pq}}{\partial T} - \frac{N_{pq}}{\tau_{pn}} - \frac{N_{pq}}{\tau_{pd}} \tag{3.17}$$

and

$$\dot{N}_{pf} = I_{pf} + \dot{T}\frac{\partial N_{pf}}{\partial T} - \frac{N_{pf}}{\tau_{pn}} - \frac{N_{pf}}{\tau_{pd}}\,. \tag{3.18}$$

In Section 4.3.1, it is shown that during flow $\tau_{pn} > 0$. Therefore the distinction between precursors and nuclei is retained. The second term on the right-hand side of Eq. (3.18) accounts for the activation of dormant flow-induced precursors, which are initially too small to nucleate. These add to the part of the number density distribution $\partial N_p/\partial T$ that lies below the actual temperature and are activated upon sufficient cooling. If the model is to be used to simulate nonisothermal flow-induced crystallization, information about the distribution of flow-induced precursors must be incorporated. A recommended first investigation is to apply different short-term flows above the nominal melting temperature, cool down to different temperatures for crystallization, and measure the nucleation density by means of optical microscopy.

Following the SJ$_2$ model, the flow-induced creation rate I_{pf} in Eq. (3.13) would be

$$I_{pf} = g_p J_2\left(\boldsymbol{B}_e^d\right), \tag{3.19}$$

where $J_2(\boldsymbol{B}_e^d)$ is the second invariant of the deviatoric elastic Finger tensor. The subscript M (see Eq. (3.11)) will be omitted in the remainder of this chapter, but it is important to keep in mind that we only use the mode with the longest relaxation time in the model of FIC kinetics.

3.5 Local formulation of flow-enhanced nucleation

In the SJ$_2$ model, Zuidema *et al.* [212, 213] introduced the idea that flow-induced nuclei act as physical crosslinks on the HMW chains, allowing them to be deformed more easily in flow and to relax more slowly after the flow has stopped. This was accounted for by an increase of the longest relaxation time of the linear viscoelastic spectrum, proportional to the number density of flow-induced nuclei: $\lambda/\lambda_0 = 1 + aN_{nf}$ with a scaling parameter a in units of volume. They showed that the strong effect of flow on the crystallization half-time, $t_{1/2} = t(\phi = 0.5)$, in the duct flow experiments of Jerschow and Janeschitz-Kriegl [112] could only be reproduced with $a > 0$. Both the nucleation rate and the shish growth rate became strongly self-enhancing due to this coupling, as opposed to the recent revision of the SJ$_2$ model by Custódio *et al.* [44]. They made the nucleation rate dependent on the stretch Λ of the slowest mode, based on the work presented in Chapters 4 and 5, but related the shish growth rate to $J_2(\boldsymbol{B}^d_{e,avg})$, given by an additional viscoelastic mode with the viscosity-averaged relaxation time of the melt. The latter was inspired by the small-angle neutron scattering experiments of Kimata *et al.* [116], who applied deuterium labeling to low, medium, and high molecular weight fractions of a polydisperse isotactic polypropylene. They showed that all fractions gave the same flow-induced equatorial scattering, representative of shish formation, which suggests that HMW chains are not present in higher concentrations in the shish than in the rest of the material. A distinction between precursors and nuclei was made neither in the SJ$_2$ model, nor in the model of Custódio *et al.*

The physical crosslinking concept is adopted here, but its formulation is modified in three ways with respect to the works mentioned above. First, obviously, flow-induced precursors as well as nuclei are included. Secondly, their influence on the slow relaxation dynamics is expressed in terms of their average number *per HMW chain involved*. And finally, swallowing of HMW chains by growing nuclei is taken into account.

Flow-induced precursors are divided into two populations: one with number density N_{0pf}, being created in the (locally) undisturbed melt, and one with number density N_{1pf}, being created in the presence of other flow-induced precursors or nuclei. Eq. (3.18) is therefore decomposed into

$$\dot{N}_{0pf} = I_{0pf} + \dot{T}\frac{\partial N_{0pf}}{\partial T} - \frac{N_{0pf}}{\tau_{pn}} - \frac{N_{0pf}}{\tau_{pd}} \tag{3.20}$$

and

$$\dot{N}_{1pf} = nvI_{1pf} + \dot{T}\frac{\partial N_{1pf}}{\partial T} - \frac{N_{1pf}}{\tau_{pn}} - \frac{N_{1pf}}{\tau_{pd}}\,. \tag{3.21}$$

Here n is the number density of domains where the creation rate is increased due to the presence of both populations; v is the volume of such a domain, called an *incubator*, which is expected to have a radius on the order of the mean squared radius of gyration $\langle r_g^2\rangle^{1/2}$

of the HMW chains. The third term on the right-hand side of Eq. (3.20) or (3.21) is the nucleation rate of the corresponding population:

$$\dot{N}_{0nf} = \frac{N_{0pf}}{\tau_{pn}}\,, \tag{3.22}$$

$$\dot{N}_{1nf} = \frac{N_{1pf}}{\tau_{pn}}\,. \tag{3.23}$$

The shorthand notation

$$N_{0f} = N_{0pf} + N_{0nf} \tag{3.24}$$

is used to denote the combined number density of flow-induced precursors of population 0, created in the undisturbed melt, and nuclei formed out of them. Similarly, for population 1,

$$N_{1f} = N_{1pf} + N_{1nf}\,. \tag{3.25}$$

The total number density of flow-induced species is then

$$N_f = N_{0f} + N_{1f} = N_{pf} + N_{nf}\,. \tag{3.26}$$

The rate of change of the number density n of incubators is given by

$$\dot{n} = I_{0pf} + \dot{T}\frac{\partial N_{0pf}}{\partial T} = \dot{N}_{0f} + \frac{N_{0pf}}{\tau_{pd}} \tag{3.27}$$

under the assumption $\tau_{pd} \gg 1/I_{1pf}$. Then each precursor of population 0 initiates a new incubator, which remains when that precursor dissolves because population 1 has formed around it in the meantime. Eqs. (3.20) and (3.21) add up to Eq. (3.18) with the overall creation rate

$$I_{pf} = I_{0pf} + nvI_{1pf} = g_p f(\boldsymbol{B}_{e0}) + nvg_p f(\boldsymbol{B}_e)\,, \tag{3.28}$$

where $\boldsymbol{B}_{e0}$ is the elastic Finger tensor of the original (undisturbed) slowest relaxation mode, while $\boldsymbol{B}_e$ is the elastic Finger tensor of the slowest relaxation mode, influenced by the presence of flow-induced precursors and nuclei. The function f will be specified later.

The most straightforward modification of the SJ$_2$ model is to calculate the evolution of $\boldsymbol{B}_e$ with the time dependent relaxation time multiplier

$$\frac{\lambda_k}{\lambda_{0k}} = 1 + \frac{aN_f}{n} \quad ; \quad k \in \{d, R\}\,, \tag{3.29}$$

where λ_d and λ_R are the reptation (or disengagement) time and the stretch relaxation (or Rouse) time of the HMW chains, respectively. The subscript 0 refers to their values in the (locally) undisturbed melt. Now the scaling parameter a is dimensionless. The relaxation times increase proportional to the average number of flow-induced precursors and nuclei per incubator, rather than their total number density. Thus the idea of a local effect on relaxation dynamics, proposed by Zuidema *et al.* [212, 213], is now consistently formulated in a local sense. However, the nuclei in one incubator will have merged into a single spherulite by the time they are large enough to be seen through an optical microscope, $R \approx 1\,\mu\mathrm{m} \gg \langle r_g^2 \rangle^{1/2}$. Therefore the observable flow-enhanced nucleation rate is just $\dot{N}_{0nf}$. This is independent on $\boldsymbol{B}_e$ and consequently not influenced by the physical crosslinking effect, Eq.(3.29). It will be shown in Section 4.3 that number densities of spherulites after moderate to strong flows cannot be captured by a function of $\boldsymbol{B}_{e0}$ alone.

3.5.1 Influence of convection

If flow-induced precursors and nuclei are loosely connected to the initiating HMW chains and to each other, some of them may be convected out of their incubators. This is illustrated in Figure 3.2. Presuming that these convected species are slowly relaxing structures themselves, it is even conceivable that they form new incubators. Some of the precursors within these domains will then in turn be convected at a higher velocity $\Delta\vec{v}$ relative to the original HMW chain, depending on their position $\Delta\vec{x}$ with respect to it and on the velocity gradient $\vec{\nabla}\vec{v}$. At a short distance ($\Delta\vec{x} \to 0$) or in a homogeneous flow field, $\Delta\vec{v} = \Delta\vec{x} \cdot \vec{\nabla}\vec{v}$. In uniaxial elongation, the velocity difference increases with the component of $\Delta\vec{x}$ parallel to the flow direction, in planar shear with the component perpendicular to the flow direction. The result of this combined creation and convection is an expanding oblong ‘nebula’ of incubators. The space covered by such nebulae and the number density of separate spherulites obtained can only be calculated if convection of precursors and nuclei is included in our FIC model.

A simple scaling analysis is possible if enhanced creation around convected species is neglected. Then half the length of a nebula is at most equal to the maximum distance traversed by a precursor or nucleus relative to its incubator (upstream or downstream). After a strain γ, this is $d_{max} \sim \gamma \langle r_g^2 \rangle^{1/2}$. Fetters *et al.* [62] reported the following relation between the mean squared end-to-end distance and the molecular weight, $\langle r^2 \rangle / M = 0.694\,\mathrm{\mathring{A}}^2\mathrm{mol/g}$, for isotactic polypropylene (iPP). With a molecular weight $M \sim 10^5\,\mathrm{g/mol}$, a common weight average for polydisperse iPPs, we find $\langle r_g^2 \rangle = \frac{1}{6}\langle r^2 \rangle \sim 10^4\,\mathrm{\mathring{A}}^2$. With $\gamma \sim 10^2$, a typical strain applied in FIC experiments, $d_{max} \sim 1\,\mu\mathrm{m}$. Precursors and nuclei, created in the same incubator, will then still grow into a single spherulite. It could be that only chains of much higher molecular weight, say $M \sim 10^7\,\mathrm{g/mol}$, are responsible for creation of precursors. In that case $d_{max} \sim 10\,\mu\mathrm{m}$, which is just enough for nuclei to grow into (at least initially) separate spherulites. However, after 100 strain units, this only holds for those nuclei whose precursors were created at the very beginning of flow. Furthermore, this small convection is not sufficient to eventually generate a homogeneous distribution of spherulites. Enhanced creation of flow-induced precursors around convected species, as explained above,

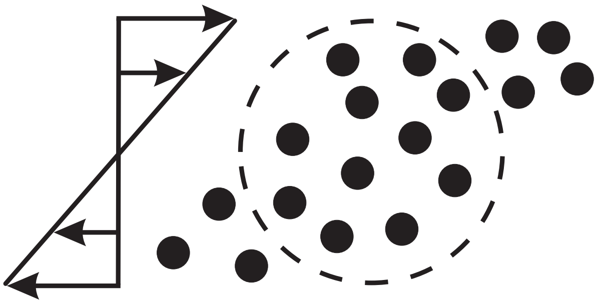

Figure 3.2: Flow-induced precursors, created in an incubator (dashed line) and convected out of it. Connections, either direct by shared chains or indirect through entanglements, are not depicted.

leads to a more explosive covering of the material volume. Before continuing the analysis to include this effect, we first discuss some experimental results concerning the critical molecular weight of chains, able to form precursors.

Since it is related to relaxation dynamics, the critical molecular weight for precursor creation should decrease with increasing flow rate. The molecular weight distribution might also play a role via constraint release. According to Struglinski and Graessley [180], for bimodal linear-linear blends the effect of constraint release on long-chain relaxation is negligible if $Z_{HMW}/Z_{LMW}^3 \ll 0.1$, where Z_{HMW} and Z_{LMW} are the molecular weights of the long (HMW) and short (LMW)chains, respectively, in units of the average molecular weight between entanglements. The polydispersity of the components of the blends, investigated by Struglinski and Graessley, was very low. No similar criterion is available for melts with a broad distribution. For an iPP with weight average $M_w = 4.81 \times 10^5\,\mathrm{g/mol}$ and polydispersity index $PDI = M_w/M_n = 6.4$, Graham and Olmsted [74] found the critical molecular weight to be at least $M^* = 4.20 \times 10^6\,\mathrm{g/mol}$, comparing kinetic Monte Carlo simulations of flow-enhanced nucleation [73, 75] to measured nucleation rates during slow shearing (up to $\dot{\gamma} = 0.3\,\mathrm{s}^{-1}$ at $T = 140^\circ\,\mathrm{C}$ [41]).

Seki *et al.* [171] studied the crystallization of iPP-iPP blends in a pressure-driven slit flow at almost the same temperature, $T = 137^\circ\,\mathrm{C}$. They found that the addition of chains with $M_w = 9.23 \times 10^5\,\mathrm{g/mol}$ and $PDI = 1.3$ to the base material ($M_w = 1.86 \times 10^5\,\mathrm{g/mol}$, $PDI = 2.3$) resulted in an oriented skin layer starting at a greater distance from the wall, where the stress (or, equivalently, the average molecular conformation) was lower. The molecular weight distributions of the two blend components were well separated and the long chain concentrations were $< 2\,\mathrm{wt}\%$, comparable to the work of Bashir and Keller [20]. The constant wall shear stresses ranged from 70 to $140\,\mathrm{kPa}$. Estimating the viscosity to lie between 1 and $10\,\mathrm{kPa\,s}$, shear rates near the wall (before crystallization) on the order of 10 to $10^2\,\mathrm{s}^{-1}$ are found. Pointlike nucleation is enhanced by chains that are on average shorter than those initiating shish growth [195]. Consequently, the critical molecular weight M^* for flow-enhanced nucleation must have been on the order of $10^5\,\mathrm{g/mol}$ or lower, which yields a concentration of chains above M^* much higher than the few $\mathrm{wt\%}$ of long ones added. This explains why no influence of blend composition on the spherulitic structure below the skin of their samples was observed.

The results of Graham and Olmsted [74] (using the experimental data of Coccorullo *et al.* [41]) and Seki *et al.* [171] demonstrate that the critical molecular weight indeed decreases with increasing flow rate. A difference in M^* of one decade is found at nearly the same temperature. If the shear rates in the experiments of Seki *et al.* were on the order of $10\,\mathrm{s}^{-1}$, the difference in $\dot{\gamma}$ is two decades. This suggests that pointlike precursor creation is enhanced by a HMW fraction for which the stretch-based Weissenberg number exceeds a critical value, defined as

$$Wi_R^* = \dot{\gamma}\lambda_R(M^*) \sim \dot{\gamma}M^{*2}\,. \tag{3.30}$$

Alternatively, estimating shear rates on the order of $10^2\,\mathrm{s}^{-1}$ in the experiments of Seki *et al.*, a reptation-based criterion is found,

$$Wi_d^* = \dot{\gamma}\lambda_d(M^*) \sim \dot{\gamma}M^{*3}\,, \tag{3.31}$$

which is in accordance with the analysis of a large number of FIC experiments by Van Meerveld *et al.* [195].

Coming back to our scaling analysis of convection out of incubators, it turns out that $d_{max} \sim 10\,\mu\mathrm{m}$, based on $M^* \sim 10^7\,\mathrm{g/mol}$, is a rather generous estimate. Nevertheless, it is still very small. Optical micrographs after flow, in the regime of pointlike nucleation, often exhibit a (seemingly) homogeneous distribution of spherulites [13, 110, 163]. In order to create such a morphology from nuclei, confined to domains of about $10\,\mu\mathrm{m}$ in radius, either these domains would have to overlap, leading to number densities many orders of magnitude higher than those observed, or the nuclei in each domain would have to merge into a single spherulite. The latter again makes N_{0nf} the number density of separate spherulites, which does not agree with experimental data for moderate to fast flows; see Section 4.3. Examples of inhomogeneous pointlike nucleation densities can be seen in optical micrographs of Elmoumni *et al.* [60, 61] and Azzurri and Alfonso [12], showing trains of spherulites aligned in the flow direction, typically hundreds of micrometers long. This can certainly not be explained by convection of flow-induced precursors and nuclei out of incubators, unless the environments of these convected species act as new incubators. Rodlike structures of about 100μm were observed by Acierno *et al.* [1] and Baert and Van Puyvelde [13]. It is hard to tell from their pictures whether these were also trains of spherulites, impinged because they were closer together than the ones in the previously cited works, or short shish-kebabs. Trains and rodlike structures were observed under flow conditions where no clearly recognizable shish-kebabs were formed yet, but pointlike nucleation was already enhanced.

In summary, the scenario proposed so far cannot agree with observations in FIC experiments as long as accelerated creation of precursors in the vicinity of convected species is not taken into account. Appendix 3B presents a formal description of precursors and nuclei being convected out of (and forming new) incubators. The question whether this hypothetical phenomenon is sufficient to explain a homogeneous spherulitic structure is left open for the time being. It is incorporated in the model here, taking an empirical approach, but the result is compatible with the framework presented in Appendix 3B.

The assumption is made that precursors and nuclei, convected out of an incubator, contain the same HMW fraction as the chain on which the precursors were created. This implies that M^* is sufficiently low for the coils of HMW chains to overlap. The creation rate is thus determined by the same function $f(\boldsymbol{B}_e)$ in all incubators, which have the same volume v. The model can easily be reformulated to describe precursors and nuclei as being composed of faster relaxing chains besides the initial one from the HMW fraction, which gave rise to the creation of the precursor of population 0. This will require an expression for the relaxation dynamics, equivalent to Eq. (3.29) but with shorter initial relaxation times λ_{0k}, for the convected species. Mode $M-1$ or an average over all modes might be used. The average volume of the corresponding incubators will be smaller. The choice made here yields the strongest enhancement of the final spherulitic number density and has a minimum number of free parameters.

The history of individual incubators is neglected, by assigning the average number of flow-induced species N_f/n to all of them. As explained in Appendix 3B, Eq. (3.27) should then be replaced by

$$\dot{n} = I_{0pf} + \dot{T}\frac{\partial N_{0pf}}{\partial T} + c\zeta\left(N_f - n\right) , \tag{3.32}$$

where $c \in [0,1]$ is a dimensionless connectivity parameter. The last term of Eq. (3.32) represents the creation of new incubators due to convection of flow-induced precursors and nuclei out of the existing ones. Hence ζ [s^{-1}] depends on the surface area through which outward convection occurs, and consequently on the type of flow. If the incubators are assumed spherical, in a simple shear flow

$$\zeta = \frac{\dot{\gamma}}{\pi} . \tag{3.33}$$

The derivation is given in Appendix 3B.

Suppose that flow-induced precursors and nuclei are very well connected to the initializing HMW chain of an incubator, i.e. $c \to 0$ in Eq. (3.32). A natural choice is then to use a rheological model for branched polymers to calculate the deformation of the slowest relaxation mode and to replace Eq. (3.29) by a similar expression for the number of arms per HMW backbone. It is demonstrated in Appendix 3C that this approach does not yield the desired behavior, namely an increase of the reptation and stretch relaxation times of the backbone, because it is diluted by an increasing amount of arm material.

Because every nucleated incubator grows into a single spherulite, Eq. (3.5) is replaced by

$$\frac{\dot{\Psi}_3}{8\pi} = \dot{N}_{nq} + \begin{cases} \dot{N}_{nf} & \text{if} \quad N_{nf} \leqslant n \\ \dot{n} & \text{if} \quad N_{nf} > n \end{cases} , \tag{3.34}$$

considering the flow-induced nuclei to de distributed evenly among the incubators. If the history of individual incubators were resolved by the model, each incubator would contain a different number of nuclei, based on its lifetime.

With n appearing in Eq. (3.29) and its evolution given by Eq. (3.32) instead of Eq. (3.27), FIC in the spherulitic regime is governed by a subtle interplay of phenomena. Creation of new flow-induced precursors increases the relaxation times λ_d and λ_R of the HMW fraction, which makes it a self-enhancing process via $f(\boldsymbol{B}_e)$ in Eq. (3.28). Convection decreases these relaxation times, which has a negative effect on I_{1pf} and hence on N_f, the source of the convection term in Eq. (3.32). On the other hand, the increased volume fraction nv, where I_{1pf} is active according to Eq. (3.28), has a positive effect on the creation rate.

Dormant flow-induced precursors, i.e. ones that are unable to nucleate at the temperature at which the crystallization is taking place, are not included as physical crosslinks in Eq. (3.29). In an extended model, some of these might be created in the incubators, initially formed by active flow-induced precursors, while others might form their own incubators, in which also active precursors could be created. Thus the numerator as well as the denominator in Eq. (3.29) would change. Such an extended model is beyond the scope of this work, because it cannot be validated with the experimental data currently available. As explained earlier, short-term flow followed by crystallization at different temperatures, combined with in-situ optical microscopy, should be a straightforward method to relate incremental changes in the strength or duration of flow to changes in the distribution $\partial N_{pf}/\partial T$.

3.5.2 Swallowing of HMW chains by growing nuclei

Now the final modification of the SJ$_2$ model's coupling between structure and relaxation dynamics is made. The underlying idea is that, as precursors nucleate and grow, the HMW chains are gradually incorporated in the crystalline structure. Their amorphous ends become shorter and less entangled with other amorphous chains. The reptation and stretch relaxation times of these ends consequently decrease. It seems reasonable to assume that precursors are predominantly created close to the center of the chain, since that is where the largest stretch occurs. The resulting nuclei are therefore conveniently lumped into a single crystalline particle at the center. Its radius is given by

$$R_c = \frac{\Psi_{2f}}{8\pi n} , \tag{3.35}$$

where Ψ_{2f} follows from Eq. (3.6) with Ψ_3 replaced by $\Psi_{3f} = 8\pi N_{nf}$. The remaining amorphous part is described as a random walk of Z_{am} segments of length l between entanglements. Neglecting flow-induced anisotropy, its mean squared radius of gyration is

$$\langle r^2_{g,am} \rangle = \frac{Z_{am} l^2}{6} \tag{3.36}$$

with $\langle \ldots \rangle$ indicating an average over all conformations. The mean squared radius of gyration of the partly crystalline chain is

$$\langle r^2_g \rangle = \langle (R_c + r_{g,am})^2 \rangle = R^2_c + \langle r^2_{g,am} \rangle \tag{3.37}$$

since, by definition, $\langle r_{g,am} \rangle = 0$. Small-angle neutron scattering studies of isotactic polypropylene [17] have shown that quiescent crystallization hardly affects $\langle r^2_g \rangle$. This is probably not true when highly oriented shish structures are formed, but may be a considered a reasonable assumption in the pointlike nucleation regime. Therefore we take

$$\langle r^2_g \rangle \approx \frac{Z l^2}{6}, \tag{3.38}$$

which, using Eqs. (3.36) and (3.37), leads to

$$R^2_c \approx \frac{Z_c l^2}{6} \tag{3.39}$$

with $Z_c = Z - Z_{am}$ the number of Kuhn segments incorporated in the crystalline phase. The fraction of amorphous segments is then

$$\frac{Z_{am}}{Z} = 1 - \frac{Z_c}{Z} = 1 - \frac{R^2_c}{\langle r^2_g \rangle}. \tag{3.40}$$

Considering that the reptation time of the amorphous part scales with Z^3_{am} and the Rouse time of the amorphous part with Z^2_{am}, we get

$$\frac{\lambda_d}{\lambda_{0d}} = \left[1 - \frac{R^2_c}{\langle r^2_g \rangle} \right]^3 \left[1 + \frac{a N_f}{n} \right] \mathcal{H}\left(\langle r^2_g \rangle - R^2_c \right) \tag{3.41}$$

and

$$\frac{\lambda_R}{\lambda_{0R}} = \left[1 - \frac{R^2_c}{\langle r^2_g \rangle} \right]^2 \left[1 + \frac{a N_f}{n} \right] \mathcal{H}\left(\langle r^2_g \rangle - R^2_c \right), \tag{3.42}$$

in which $\mathcal{H}$ is the Heaviside step function.

Swallowing of chain segments by the growing crystalline phase was also described by Doufas *et al.* [52, 53]. They used a single-chain formulation, taking the fraction of crystallized segments equal to the overall degree of crystallinity χ, obtained from a modified Nakamura equation. The relaxation time of the amorphous part of the chain was assumed to decrease proportional to $(1-\chi)^2$. They used a Giesekus model with finite extensibility, in which the nonlinear force factor was also related to the degree of crystallinity. This is similar to the model of Van Meerveld *et al.* [193] who, instead of the degree of crystallinity, used the semicrystalline volume fraction ϕ, obtained from a modified set of Schneider equations. The relaxation time was not modified in their model. Not only the nucleation rate, but also the radial growth rate depends on the conformation of the amorphous part, according to both Doufas *et al.* and Van Meerveld *et al.* This is a debatable feature of the single-chain approach, since the growth process at the interface between the phases involves many chains with crystallized fractions ranging from zero to one. Polydispersity is also neglected. This may be justified for flow-enhanced nucleation, which favors the high-end tail of the molecular weight distribution, but not for flow effects on the radial growth rate.

3.6 Results

The local flow-enhanced nucleation model is compared to a subset of the flow-enhanced nucleation experiments, discussed in Chapter 4. Isotactic polypropylene was subjected to short-term shear at a rate of $60\,\mathrm{s}^{-1}$ and shear times varying between 1 and 6 seconds [98]. Based on experimental observations that the distribution in sizes of spherulites is very narrow, it is assumed that the characteristic time of nucleation in flow is much longer than the shear time, whereas in the absence of flow it is very small. Therefore we take

$$\tau_{pn} = \begin{cases} \infty & \text{for} \quad \dot{\gamma} \neq 0 \\ 0 & \text{for} \quad \dot{\gamma} = 0 \end{cases} \tag{3.43}$$

with the consequence that precursors are created during flow and instantaneously nucleated after flow. This is discussed in relation with other published experimental observations in Chapter 4. Thus the effective number density of flow-induced nuclei, to be substituted in Eq. (3.5), determining the number density of separately observable spherulites, equals 0 during flow and n afterwards. See also Eq. (3.34).

Due to Eq. (3.43), swallowing of HMW chains occurs only after flow. It is interesting to speculate that, with a large but finite value of τ_{pn} during flow, Eqs. (3.41) and (3.42) might be able to explain the experimentally observed saturation of flow-enhanced nucleation [14, 97], discussed in Section 4.1.2. The GENERIC analysis of phase transformation by Hütter [99] is important in this respect. He found that, for conditions under which the nucleation rate vanishes, the growth rate also vanishes. This suggests that a large but finite value of τ_{pn} would be accompanied by a low growth rate, which might be sufficient to swallow those incubators that are nucleated, without leading to observable spherulites

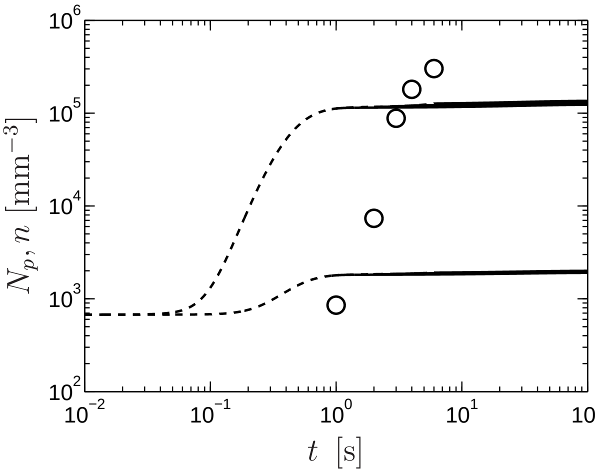

Figure 3.3: Number densities of precursors (dashed lines) and nucleated incubators (solid lines) for the model with constant g_p. Measured spherulite densities, which were constant and observed after shearing ($\dot{\gamma} = 60\,\mathrm{s}^{-1}$), are plotted versus shear time (symbols).

during flow. We do not explore these ideas further here.

Simulation results are shown in Figure 3.3. The incubator volume $v = 3.63 \times 10^{-14}\,\mathrm{mm}^3$ was used, based on a radius $\langle r_g^2 \rangle = \frac{1}{6}\langle r^2 \rangle = 0.116M$ Å^2 [62] with $M = M_w = 365 \times 10^3\,\mathrm{g/mol}$ [97]. The creation rates I_{0pf} and I_{1pf} were expressed analogous to Eq. (3.19). The physical crosslinking parameter $a = 10^3$ and the connectivity parameter $c = 1$ were kept fixed, while g_p was varied: $g_p = 1\,\mathrm{mm}^{-3}\,\mathrm{s}^{-1}$ and $g_p = 10^2\,\mathrm{mm}^{-3}\mathrm{s}^{-1}$. Dashed lines in the figure represent the number density of precursors $N_p = N_{pq} + N_{pf}$, whereas solid lines represent the number density of nucleated incubators n after flow, which is nearly the same for all shear times. The relative amounts of flow-induced species (precursors and nuclei) of populations 0 and 1 can be checked by storing them separately or by running an additional simulation with $c = 0$, while keeping the other parameters the same. In the latter case, due to the absence of convection, the flow-induced number density N_{0f} of population 0 is equivalent to that of the incubators, n. We find that mainly population 0 is formed. Consequently, the number of flow-induced species per incubator is close to one. When g_p decreases, the upturn of N_{pf} shifts to longer times, but also a smaller N_{pf} (and therefore a smaller n) is reached at the end of flow. Changing a has no effect on these results. The reason is that the volume fraction nv, in which population 1 is created, is too small to generate a significant amount of this population.

According to Chapter 5, g_p follows the temperature dependence of the relaxation dynamics, $g_p \sim a_T$. Therefore we introduce a difference in this kinetic parameter between the undisturbed melt and the incubators,

$$\frac{g_{1p}}{g_{0p}} = \frac{\lambda_k}{\lambda_{0k}} \quad ; \quad k \in \{d, R\}\,, \tag{3.44}$$

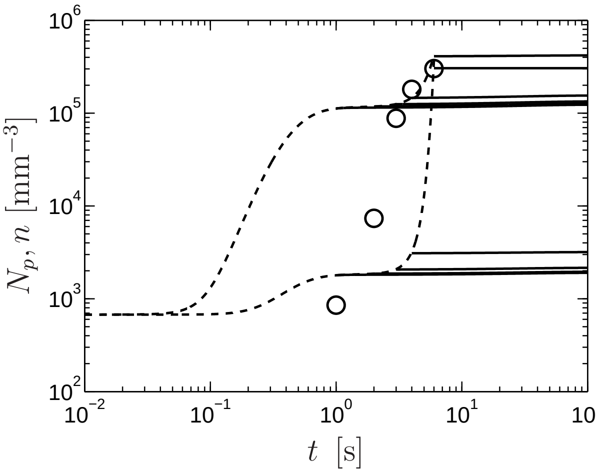

Figure 3.4: Number densities of precursors (dashed lines) and nucleated incubators (solid lines) for the model with constant g_{0p} and changing g_{1p}. Measured spherulite densities, which were constant and observed after shearing ($\dot{\gamma} = 60\,\mathrm{s}^{-1}$), are plotted versus shear time (symbols).

where λ_k is given by Eq. (3.29) and Eq. (3.28) is replaced by

$$I_{pf} = I_{0pf} + nvI_{1pf} = g_{0p}f(\boldsymbol{B}_{e0}) + nvg_{1p}f(\boldsymbol{B}_e)\,. \tag{3.45}$$

The results of the model with this modification are shown in Figure 3.4, again using the second invariant of the deviatoric part as the function f; see Eq. (3.19). Now population 1 kicks in on top of population 0 and there is a significant effect of the shear time on N_{pf}, and consequently on n. The experimental data dictate that we should have a small increase of population 0 and a large increase of population 1 on top of that. When g_{0p} is decreased, again the upturn of N_{pf} shifts to longer times, but also the level decreases. Therefore, keeping all other parameters the same as in the previous simulations, the physical crosslinking parameter is modified, $a = 2.4 \times 10^4$ for $g_{0p} = 1\,\mathrm{mm}^{-3}\mathrm{s}^{-1}$ and $a = 10^2$ for $g_{0p} = 10^2\,\mathrm{mm}^{-3}\mathrm{s}^{-1}$, to fit the data for the longest shear time. For the shorter shear times, the second upturn of N_{pf}, due to population 1, is still only mildly affected. This is again mainly due to the fact that the volume fraction nv appears as a factor in front of the creation rate I_{1pf} and, additionally, when we decrease g_{0p} to get the time scale right, g_{1p} decreases as well.

3.7 Conclusions

Consequences of the hypothesis of physical crosslinking in FIC have been investigated, since it lacks a clear theoretical foundation in previous publications [44,157,158,182,212,213]. A flow-enhanced nucleation model, based on a local formulation, literally following along the lines of this hypothesis, does not capture experimental flow-enhanced nucleation data. The reason is that the enhanced creation of flow-induced precursors in the spheres of influence of other flow-induced species (i.e. in what we call incubators) still depends on the rate of creation of incubators in the undisturbed melt. A low undisturbed creation rate and a very high enhanced creation rate might fit experimental data, but then the volume of incubators would have to be increased to (within the context of our model) unreasonably large values, specifically $v \gg 4\pi\langle r_g^2\rangle^{3/2}/3$.

When flow stops, the creation process within the incubators is still enhanced, but because new precursors and nuclei are no longer convected out of the incubators, the number density of spherulites only increases further due to the creation process in the undisturbed melt. This change is insignificant due to the relatively fast relaxation of the stretch of HMW chains that are not crosslinked. Thus the local flow-enhanced nucleation model naturally explains the experimental observation that the number density of spherulites is essentially constant after flow [13, 60, 175]; see also Chapters 4 and 5. In the global formulation, developed in the next chapter and used, slightly modified, by Custódio *et al.* [44], this phenomenon is incorporated by assuming that flow-induced precursors immediately stop acting as physical crosslinks when they are nucleated, which is unrealistic.

Appendices

3A Instantaneous nucleation of precursors

An alternative formulation of the (unrestricted) nucleation rate, Eq. (3.16),

$$\dot{N}_n = \frac{N_p}{\tau_{pn}}\,, \tag{3A1}$$

is derived here for $\tau_{pn} \downarrow 0$, which means that all precursors are immediately transformed into nuclei. It is obvious that Eq. (3A1) cannot be used in that case.

The rate of change of the number of precursors, Eq. (3.13), is conveniently rewritten as

$$\dot{N}_p = \hat{I}_p - \frac{N_p}{\tau_p}\,, \tag{3A2}$$

where $\hat{I}_p$ comprises the thermal and athermal creation rates,

$$\hat{I}_p = I_p + \dot{T}\frac{\partial N_p}{\partial T}\,, \tag{3A3}$$

and τ_p is the characteristic time of disappearance (nucleation and dissolution) of precursors,

$$\tau_p = \frac{\tau_{pn}\tau_{pd}}{\tau_{pn} + \tau_{pd}}\,. \tag{3A4}$$

If τ_p is constant, Eq. (3A2) becomes an ordinary differential equation with general solution

$$N_p(t \geqslant t_0) = \mathrm{e}^{-\frac{t-t_0}{\tau_p}} \left[N_p(t_0) + \int_{t_0}^{t} \hat{I}_p(t')\mathrm{e}^{\frac{t'-t_0}{\tau_p}}\, dt' \right]\,. \tag{3A5}$$

The number of nuclei is obtained by integrating Eq. (3A1) after substitution of Eq. (3A5),

$$N_n\,(t \geqslant t_0) = N_n(t_0) + \int_{t_0}^{t} \left[\frac{N_p(t_0)}{\tau_p}\mathrm{e}^{-\frac{t''-t_0}{\tau_p}} + \int_{t_0}^{t''} \frac{\hat{I}_p(t')}{\tau_p}\mathrm{e}^{-\frac{t''-t'}{\tau_p}}\, dt' \right] dt''\,. \tag{3A6}$$

Now consider the case that τ_{pn} drops to zero at $t = t_0$. Eq. (3A4) shows that the disappearance of precursors then becomes dominated by nucleation,

$$\lim_{\tau_{pn}\downarrow 0} \tau_p = \tau_{pn}\,, \tag{3A7}$$

so that dissolution can be neglected. Therefore taking $\tau_p \downarrow 0$ in Eq. (3A6) and using

$$\lim_{\theta\downarrow 0} \frac{1}{\theta}\mathrm{e}^{-\frac{t-t_0}{\theta}} = 2\delta\left(t-t_0\right) \quad \text{for} \quad t \geqslant t_0 \tag{3A8}$$

and

$$\int_{t_0}^{\infty} \delta\left(t-t_0\right)\, dt = \frac{1}{2}\,, \tag{3A9}$$

where δ is the Dirac function, it follows that

$$\begin{aligned} N_n\left(t \geqslant t_0\right) &= N_n(t_0) + 2\int_{t_0}^{t}\left[N_p(t_0)\delta(t''-t_0) + \int_{t_0}^{t''} \hat{I}_p(t')\delta(t''-t')dt'\right] dt'' \\ &= N_n\left(t_0\right) + N_p\left(t_0\right) + \int_{t_0}^{t} \hat{I}_p\left(t''\right)\, dt''\,. \end{aligned} \tag{3A10}$$

Thus, if $\tau_{pn} \downarrow 0$, the nucleation rate is equal to $\hat{I}_p$. If additionally $I_p = 0$, the nucleation process is purely athermal: no new nuclei appear unless the temperature is lowered.

The result obtained here allows for a description of crystallization processes involving fast nucleation, without using Eq. (3A1). In the example used above, where a transition from slow to fast nucleation kinetics takes place at t_0, we get:

$$t < t_0 \quad \begin{cases} \dot{N}_p\left(t\right) & = \hat{I}_p\left(t\right) - \frac{N_p(t)}{\tau_p(t)} \\ \dot{N}_n\left(t\right) & = \frac{N_p(t)}{\tau_{pn}(t)} \end{cases}$$

$$t \geqslant t_0 \quad \begin{cases} N_n(t_0) & \rightarrow N_n(t_0) + N_p(t_0) \\ N_p(t_0) & \rightarrow 0 \\ \dot{N}_n\left(t\right) & = \hat{I}_p\left(t\right) \end{cases}$$

The implementation of the inverse transition is trivial.

3B Creation in and convection out of incubators

First the balance of species (precursors and nuclei) is formulated for a single incubator of volume v. The local flow-induced number density is denoted by $\tilde{N}_f$ as opposed to the continuum average N_f. Since v is not a material volume, the total number within the incubator changes due to creation as well as convection across its surface s. We imagine an environment free of incubators, except the one under consideration and those formed by species convected out of it, and limit our attention to flows with a direction that does not change in time. Consequently, there is an outflow of species where the velocity component normal to s is pointing outward, but no inflow where it is pointing inward. If the convection of species is affine, according to the Reynolds transport theorem, the rate of change of the total number within the incubator is given by

$$\frac{d}{dt}\iiint_v \tilde{N}_f dv' = \iiint_v \frac{\partial \tilde{N}_f}{\partial t} dv' - \iint_s \vec{v}\cdot\vec{e}\left(\tilde{N}_f - 1\right) ds' \,. \tag{3B1}$$

Here $\vec{v}$ is the velocity relative to s and $\vec{e}$ is the unit vector normal to s, taken positive in the outward direction. The integrand in the second term on the right-hand side, which represents the convective flux through s, is proportional to $\tilde{N}_f - 1$ because the last remaining flow-induced precursor or nucleus defines the movement of the incubator as a whole.

A scalar parameter $c \in [0,1]$ is introduced to account for connectivity, which is assumed to be the same for flow-induced precursors and nuclei. Then Eq. (3B1) becomes

$$\frac{d}{dt}\iiint_v \tilde{N}_f dv' = \iiint_v \frac{\partial \tilde{N}_f}{\partial t} dv' - c\iint_s \vec{v}\cdot\vec{e}\left(\tilde{N}_f - 1\right) ds' \,. \tag{3B2}$$

A difference in connectivity of the species can be incorporated straightforwardly, substituting

$$c = \frac{c_p\tilde{N}_{pf}}{\tilde{N}_{pf}+\tilde{N}_{nf}} + \frac{c_n\tilde{N}_{nf}}{\tilde{N}_{pf}+\tilde{N}_{nf}} \tag{3B3}$$

in Eq. (3B2) with $\{c_p, c_n\} \in [0,1]$. Small values $(c \rightarrow 0)$ correspond to chemical crosslink-like behavior.

The model used in this chapter is obtained as the result of two simplifications. First, spatial variations of $\tilde{N}_f$, resulting from inhomogeneities in the creation rate $I_{1pf} = \partial\tilde{N}_f\partial t$ or convective redistribution of species, are not resolved within an incubator. Thus

$$\vec{\nabla}\tilde{N}_f(\vec{x},t) = 0 \quad \forall \quad \vec{x} \in v \,. \tag{3B4}$$

Secondly, the material is described as a melt containing n identical incubators per unit volume, to each of which the average number of species

$$\iiint_v \tilde{N}_f dv' = \frac{N_f}{n} \tag{3B5}$$

is assigned. This has the advantage that the creation rate, the first term on the right-hand side of Eq. (3B2), is the same in each incubator:

$$\iiint_v \frac{\partial \tilde{N}_f}{\partial t} dv' = vI_{1pf} \,, \tag{3B6}$$

where I_{1pf} is a function of one $\boldsymbol{B}_e$ representative of all incubators, whose evolution is determined by reptation and Rouse times depending on N_f/n; see Eqs. (3.28) and (3.29).

This averaging introduces a bias towards newly formed incubators, since they gain flow-induced precursors and nuclei at the expense of the ones already present. The alternative is to store, in each time step from t_k to $t_{k+1} = t_k + \Delta t_k$, a new subgroup of incubators Δn_k and to calculate the new number of species $\Delta \tilde{N}_{f,1 \leqslant j \leqslant k}(t_{k+1})$ for each subgroup $\Delta n_{1 \leqslant j \leqslant k}$, using separate rheological constitutive equations with relaxation times based on $\Delta \tilde{N}_{f,1 \leqslant j \leqslant k}(t_k)$. This multi-mode approach (with an increasing number of modes, equal to the number of time steps taken) is computationally more expensive, but still feasible since the relaxation times are always longer than those of the undisturbed slowest mode of the melt, so no exceedingly short time steps are necessary.

For the averaged description used here, the total number density of flow-induced precursors and nuclei changes according to

$$\dot{N}_f = I_{0pf} + nvI_{1pf} + \dot{T}\frac{\partial N_{pf}}{\partial T} - \frac{N_{pf}}{\tau_{pd}}\,, \tag{3B7}$$

where the populations 0 and 1 are distinguished, as explained in Section 3.5. If all species convected out of an incubator act as new incubators, we find

$$\dot{n} = I_{0pf} + \dot{T}\frac{\partial N_{0pf}}{\partial T} + c\zeta\left(N_f - n\right) \tag{3B8}$$

as in Eq. (3.32) with

$$\zeta = \frac{1}{v}\iint_s \vec{v}\cdot\vec{e}\,ds'\,. \tag{3B9}$$

For a spherical incubator of radius r_v at the center of a Cartesian coordinate system $\{x, y, z\}$,

$$\vec{e} = [e_x, e_y, e_z] = [\cos\theta\sin\phi, \sin\theta, \cos\theta\cos\phi] \tag{3B10}$$

if $\{r, \theta, \phi\}$ are spherical coordinates centered at the incubator, θ being the angle to the xz plane and ϕ the angle to the z axis in the xz plane. In a planar shear flow,

$$\vec{v} = [v_x, v_y, v_z] = [\dot{\gamma}y, 0, 0] = [\dot{\gamma}r\sin\theta, 0, 0] \tag{3B11}$$

and outflow of species occurs where $\{2\theta, \phi\} \in [0, \pm\pi]$. This leads to Eq. (3.33):

$$\begin{aligned}\zeta &= \frac{2}{v}\int_0^{\pi}\int_0^{\pi/2} \dot{\gamma}y\cos\theta\sin\phi\, r_v^2\cos\theta d\theta d\phi \\ &= \frac{2\dot{\gamma}r_v^3}{v}\int_0^{\pi}\int_0^{\pi/2}\sin\theta\cos^2\theta d\theta\sin\phi d\phi = \frac{4\dot{\gamma}r_v^3}{3v} = \frac{\dot{\gamma}}{\pi}\,.\end{aligned} \tag{3B12}$$

3C Evaluation of flow-induced precursors as branch points

This appendix explores the consequences of the idea that flow-induced precursors and nuclei can be described as branch points on the HMW fraction of the molecular weight distribution. This idea implies that chain ends, sticking out of a precursor, affect the motion of the backbone, on which the precursor was formed, as though they were chemically bonded to it. In a multi-mode rheological description of the melt, an expression similar to Eq. (3.29) may be used for the number of arms of the slowest mode,

$$q = q_0 + \Delta q = q_0 + \frac{aN_f}{n}\,. \tag{3C1}$$

Here N_f/n is the average number of flow-induced precursors and nuclei per HMW chain serving as a backbone, as explained in Section 3.5 and Appendix 3B, and a should be interpreted as the average number of arms connected to these branch points.

The molecular architecture of the HMW fraction is represented by a backbone of weight Z_{0b} (in units of M_e) with q_0 arms of equal weight Z_{0a}. The fractions of material in each part are given by

$$\varphi_{0b} = \frac{Z_{0b}}{2q_0Z_{0a}+Z_{0b}}\,, \tag{3C2}$$

$$\varphi_{0a} = \frac{2q_0Z_{0a}}{2q_0Z_{0a}+Z_{0b}}\,, \tag{3C3}$$

respectively. According to the tube theory for branched polymers, developed by McLeish and coworkers [45, 46, 143], the characteristic time of arm retraction is

$$\lambda_{0a} \sim \exp\left[\frac{15Z_{0a}}{4}\left(\frac{1}{2}-\frac{\varphi_{0a}}{3}\right)\right] \tag{3C4}$$

for pom-pom or comb molecules (if the order-one ‘dynamic dilution’ exponent, α in the references above, is chosen equal to one). The backbone reptation time is

$$\lambda_{0b} \sim Z_{0b}^2\varphi_{0b}^2q_0\lambda_{0a} \tag{3C5}$$

and, for pom-poms, the backbone stretch relaxation time

$$\lambda_{0s} \sim Z_{0b}\varphi_{0b}q_0\lambda_{0a}\mathrm{e}^{-\frac{2}{q_0}(\Lambda-1)}\,, \tag{3C6}$$

was derived by Blackwell *et al.* [24].

Now Δq pseudo-arms of equal weight Z_a, attached to precursors, are added. The ensemble is modeled as a pom-pom, containing q arms of averaged weight

$$\overline{Z}_a = \frac{\Delta q Z_a + q_0 Z_{0a}}{q} \,, \tag{3C7}$$

which gives the fractions

$$\overline{\varphi}_b \;=\; \frac{Z_b}{2q\overline{Z}_a + Z_b} \,, \tag{3C8}$$

$$\overline{\varphi}_a \;=\; \frac{2q\overline{Z}_a}{2q\overline{Z}_a + Z_b} \,. \tag{3C9}$$

With Eq. (3C4), the arm relaxation time is increased according to

$$\frac{\lambda_a}{\lambda_{0a}} = \exp\left[\frac{15}{8}\left(\overline{Z}_a - Z_{0a}\right) - \frac{15}{12}\left(\overline{Z}_a\overline{\varphi}_a - Z_{0a}\varphi_{0a}\right)\right] \,. \tag{3C10}$$

For the backbone reptation time, using Eq. (3C5), we find

$$\frac{\lambda_b}{\lambda_{0b}} = \frac{\varphi_b^2 q \lambda_a}{\varphi_{0b}^2 q_0 \lambda_{0a}} = \left(1 + \frac{2\Delta q Z_a}{2q_0 Z_{0a} + Z_b}\right)^{-2}\left(1 + \frac{\Delta q}{q_0}\right)\frac{\lambda_a}{\lambda_{0a}} \tag{3C11}$$

and the increase of the backbone stretch relaxation time follows with Eq. (3C6) as

$$\frac{\lambda_s}{\lambda_{0s}} = \frac{\varphi_b q \lambda_a}{\varphi_{0b} q_0 \lambda_{0a}} = \left(1 + \frac{2\Delta q Z_a}{2q_0 Z_{0a} + Z_b}\right)^{-1}\left(1 + \frac{\Delta q}{q_0}\right)\frac{\lambda_a}{\lambda_{0a}}\, \mathrm{e}^{\left(\frac{2}{q_0} - \frac{2}{q}\right)(\Lambda - 1)} \,. \tag{3C12}$$

Because of the rather crude averaging of arm weights, Eq. (3C7), only the limiting behavior for large Δq should be considered, where $q_0 Z_{0a}$ is unimportant. Then λ_b scales with $(\Delta q)^{-1}$, whereas λ_s becomes independent on Δq. Hence Eq. (3C1) yields a completely different effect on the relaxation time than Eq. (3.29). The fact that the results in Chapters 4 and 5 are largely due to a coupling similar to Eq. (3.29) suggests that flow-induced precursors and nuclei should not be seen as branch points, but rather as weak physical crosslinks. The linear dependence of the reptation and Rouse times on their number N_f/n, as in Eq. (3.29), is in line with the idea that these physical crosslinks generate a friction force on the backbone.

Chapter four

Validation of a global formulation of flow-enhanced nucleation

Abstract

A phenomenological model for flow-enhanced nucleation is developed and validated by short-term shear experiments. The two main conclusions of this chapter are, first, that the creation of flow-induced precursors is driven by stretch, not orientation, of the primitive path of chains in the HMW tail of the molecular weight distribution, and secondly, that nucleation of these precursors is impeded by flow.

4.1 Introduction and outline of the model

The formulation of the flow-enhanced nucleation model, used in this chapter, is discussed only briefly, since a detailed discussion has been given in Sections 3.3 and 3.4. For an introduction on modeling of FIC kinetics, we also refer to Chapter 3. The results of the local model, presented in Section 3.5, were unsatisfactory from a practical point of view, since the experimentally observed effect of flow on the number density of spherulites could not be reproduced. Therefore we take a step back to an earlier, more simplified approach, and use a modified version of the SJ_2 model [212, 213], in which a distinction is made between subcritical nuclei (called precursors) and supercritical nuclei (simply called nuclei). It is important to keep in mind, however, that their effect on the relaxation dynamics of the high molecular weight (HMW) fraction of the material lacks a clear theoretical foundation, as discussed in detail in Chapter 3.

4.1.1 Creation and nucleation of precursors

The nucleation rate is given by Eq. (3.16),

$$\dot{N}_n = \dot{N}_{nq} + \dot{N}_{nf} = \frac{N_{pq} + N_{pf}}{\tau_{pn}}\,, \tag{4.1}$$

where the number density of quiescent precursors changes according to Eq. (3.17),

$$\dot{N}_{pq} = \dot{T}\frac{\partial N_{pq}}{\partial T} - \frac{N_{pq}}{\tau_{pn}} - \frac{N_{pq}}{\tau_{pd}} \tag{4.2}$$

if the quiescent creation process is athermal, while the number density of flow-induced precursors changes independently according to Eq. (3.18),

$$\dot{N}_{pf} = I_{pf} + \dot{T}\frac{\partial N_{pf}}{\partial T} - \frac{N_{pf}}{\tau_{pn}} - \frac{N_{pf}}{\tau_{pd}}\,. \tag{4.3}$$

We again remark that, for example, in the models of Grizzuti and coworkers [3, 42] and Graham and Olmsted [73, 75], the quiescent and flow-induced creation rates are not decoupled.

The flow-induced creation rate depends on the elastic Finger tensor of the slowest relaxation mode,

$$I_{pf} = g_p f\left(\boldsymbol{B}_e\right). \tag{4.4}$$

The function f will be specified later. The Rolie-Poly model [130] is used to calculate $\boldsymbol{B}_e$.

Its upper convected derivative is then given by

$$\overset{\triangledown}{\boldsymbol{B}}_e = -\frac{1}{\lambda_d}\left(\boldsymbol{B}_e - \boldsymbol{I}\right) - \frac{2}{\lambda_R}\left(1 - \frac{1}{\Lambda}\right)\left(\boldsymbol{B}_e + \beta\Lambda^{2\delta}\left(\boldsymbol{B}_e - \boldsymbol{I}\right)\right) \tag{4.5}$$

with the stretch parameter

$$\Lambda = \sqrt{\frac{\operatorname{tr}\left(\boldsymbol{B}_e\right)}{3}} \tag{4.6}$$

according to Eq. (3.4). The last term represents convective constraint release, which is controlled by the parameters $\beta \in [0,1]$ and δ.

The reptation time λ_d and the Rouse time λ_R are linear functions of the number densities of flow-induced precursors and nuclei,

$$\frac{\lambda_k}{\lambda_{0k}} = 1 + a\left(N_{pf} + N_{nf,R<R^*}\right) \quad ; \quad k \in \{d, R\}\,, \tag{4.7}$$

where R^* is a critical radius, on the order of the radius of gyration of the HMW chains, which determines whether a flow-induced nucleus acts as a physical crosslink ($R < R^*$) or as a viscoelastic particle ($R \geqslant R^*$). This can be seen as a more empirical way to describe the swallowing of chain ends by the growing nuclei, as compared to the more detailed description in Section 3.5. There the swallowing phenomenon was incorporated in Eqs. (3.41) and (3.42) via the coarse-grained radius of the crystalline structure within an incubator. We have no concept of a structure that could cause the relaxation behavior described by Eq. (4.7), which was the reason to develop a more detailed model in Chapter 3. In order for the continuum-level $N_f = N_{pf} + N_{nf}$ to be a measure of the local $\tilde{N}_f$ (Appendix 3B) it would have to be many orders of magnitude higher than experimentally observed number densities of spherulites. See Section 3.2 and Figure 3.1. Conversely, $\tilde{N}_f$ being an average over v, this volume would have to be much larger than the expected range of influence of a flow-induced precursor or nucleus, $v \gg \langle r_g^2\rangle^{3/2}$, in order to obtain $\tilde{N}_f \sim N_f$. Without a clear concept, it is hard to build a well-founded model for the swallowing of chain ends. In the empirical approach taken here, it turns out that experiments are fitted most accurately with $R^* = 0$.

4.1.2 Saturation

Housmans *et al.* [97] recently studied three iPPs with different molecular weight distributions. Oscillatory shear measurements after short periods of steady shearing showed the fingerprints of different FIC regimes. Upon increasing the duration of flow, log(G') versus log(t) curves shifted to shorter times without changing shape, indicating that the number densities of pointlike nuclei were increased but remained constant after the flow was stopped. A saturation of this enhanced nucleation was clearly observed: identical results were obtained for longer shear times. A second acceleration occurred when the flow was maintained even longer. Not only did the log(G') versus log(t) curves shift to shorter times again, but their shape also changed, indicating a transition from spherulitic to oriented crystallization. These interpretations were confirmed by ex-situ micrographs of the final semicrystalline morphologies. In the saturation regime, the number densities of spherulites were indeed identical. This can be considered the first unambiguous evidence of a maximum pointlike nucleation density. Baert *et al.* [14] also reported a plateau in the time scale of crystallization as a function of shear rate, followed by a second acceleration at high shear rates. However, they compared experiments where the same strain was applied. This means that both the shear rate and the shear time varied, which confuses interpretation. The same strain with a different combination of rate and duration of flow does not yield the same molecular deformation (neither in the transient startup behavior nor in the steady state). Nevertheless, the acceleration following the saturation plateau was concurrent with an upturn of the birefringence during flow, related to the growth of threadlike precursors, in agreement with the work of Kumaraswamy *et al.* [120]. These results are further supported by the fact that, for one iPP subjected to two different shear rates, Housmans *et al.* [97] detected an upturn in the first normal stress difference during flow exactly at the times marking the transition from the saturated pointlike nucleation regime to the oriented crystallization regime.

Martins *et al.* [141] suggested that saturation of flow-enhanced nucleation is the result of the melt reaching its steady state. However, the first normal stress difference data of Housmans *et al.* [97] showed that, in all their FIC experiments, the steady state was reached about ten times later than the onset of the saturation plateau. This was confirmed by viscosity measurements [J.-W. Housmans, personal communication].

Saturation is implemented in the present model in a phenomenological way, writing g_p in Eq. (4.4) as

$$g_p = \left(1 - \frac{N_f}{N_{f,max}}\right) g_{0p} \, . \tag{4.8}$$

The saturated number density $N_{f,max}$ is expected to be related to a critical molecular weight for pointlike precursor creation, but is determined directly from nucleation data in Section 4.3.

4.2 Experiments

4.2.1 Flow-enhanced nucleation

We compare simulation results to experimental data of Hristova *et al.* [98] for the polydisperse linear iPP HD120MO from Borealis. Different aspects of the morphology,

Table 4.1: Number densities of spherulites N_{sph} and presence of oriented crystallites in iPP2 after different shear histories at $135\,^{\circ}\mathrm{C}$ [98]. Measured growth rate $\dot{R}$ and expected diameter D of largest spherulites at the end of flow.

$\dot{\gamma}$ $[\mathrm{s}^{-1}]$	t_s $[\mathrm{s}]$	$\dot{R}$ $[\mathrm{nm\,s}^{-1}]$	N_{sph} $[\mathrm{mm}^{-3}]$	Orient. cryst.	$D = 2\dot{R}t_s$ $[\mu\mathrm{m}]$
0	0	42	6.8×10^2	−	0
2	30	41	6.8×10^2	−	2.5
4	15	51	2.4×10^3	−	1.5
	60	39	2.5×10^5	+	4.7
	90	40	3.5×10^5	+	7.2
10	3	42	1.3×10^3	−	0.25
	6	43	1.7×10^3	−	0.52
	36	49	7.1×10^5	+	3.5
20	3	43	8.6×10^2	−	0.26
30	2	47	8.6×10^2	−	0.19
	3	46	1.6×10^3	−	0.28
	6	52	3.6×10^4	+	0.62
40	3	38	6.8×10^4	+	0.23
60	1	70	8.6×10^2	−	0.14
	2	48	7.4×10^3	+	0.19
	3	50	8.8×10^4	+	0.30
	4	37	1.8×10^5	+	0.30
	6	37	3.0×10^5	+	0.44

developing during and after different short-term shear flows, which were applied directly after cooling to a constant crystallization temperature, were investigated by means of different techniques. The pointlike nucleation densities, of interest here, were obtained from in-situ optical microscopy using a Linkam shear cell. The number density of spherulites was estimated from the number of spherulites per unit area of observation, for which the relation

$$N_{sph}\ \left[\mathrm{mm}^{-3}\right] = \left(N_{sph}\ \left[\mathrm{mm}^{-2}\right]\right)^{3/2} \tag{4.9}$$

was used [66]. This is based on the assumption that the square root of the number per unit area is a characteristic one-dimensional number density along a line, which is then cubed to obtain the three-dimensional volumetric number density. Spherulites out of focus were not counted, in order to get as close as possible to a number per unit area.

Simulation results are also compared to experimental data of Housmans *et al.* [97], which were obtained at a slightly different temperature for the same material and for two iPPs with a different molecular weight distribution: HD234CF from Borealis and 13E10 from DSM.

Table 4.2: Properties and longest reptation and Rouse time at 138°C of iPPs [97].

iPP	T_m [°C]	M_w [kg/mol]	M_w/M_n	$Z = M_w/M_e$	λ_{0d} [s]	λ_{0R} [s]
1	159	310	3.4	60	11.8	0.066
2	163	365	5.4	70	56.3	0.27
3	162	636	6.9	122	690	1.9

The number densities of spherulites were determined from rheological measurements after short-term shear, applying the Kolmogorov–Avrami equation, Eq. (3.9), in combination with the linear viscoelastic suspension model presented in Chapter 2. Molecular characteristics of the materials are given in Table 4.2. They are referred to as iPP1, iPP2, and iPP3 as indicated in the first column.

In both sets of experiments, the common short-term shearing protocol was applied. Samples were annealed above the equilibrium melting temperature to erase residual structures, cooled to a temperature were crystallization occurs ($135\,°\mathrm{C}$ [98] or $138\,°\mathrm{C}$ [97]). Directly after reaching this temperature, a shear flow was applied for a duration t_s at a constant rate $\dot{\gamma}$.

Hristova *et al.* determined the lamellar growth rate, $\dot{R}$ in Eqs. (3.6-3.8), from successive microscopic pictures of spherulites. While $\dot{R}$ turned out to be constant in each experiment, it varied considerably between experiments, from 37 to $70\,\mathrm{nm/s}$, as seen in Table 4.1. No correlation with the shear rate or shear strain was found. The experimental conditions, $\dot{\gamma}$ and t_s, and the number density of spherulites N_{sph} are also given in Table 4.1. Furthermore, the presence of oriented crystallites is indicated. Their numbers were orders of magnitude smaller than those of the spherulites. The nucleation density is thus dominated by the pointlike nuclei and can be used to validate our flow-enhanced nucleation model.

No noticeable space filling occurred during flow in any of the experiments of Hristova *et al.*, even for the longest shear time of 90 seconds. Furthermore, when the crystallites grew large enough to be detected, their number had already become constant. These observations confirm that the flow was always applied in the early stage of crystallization, characterized by unbounded creation and nucleation of precursors, as it should be in order to avoid disturbance of the flow, and hence of the crystallization kinetics, by growing crystallites.

4.2.2 Rheological characterization

The linear viscoelastic behavior of the three iPPs was measured and fitted with discrete relaxation spectra by Housmans *et al.* [97]. They estimated the Rouse time of the slowest mode using the Doi–Edwards result for monodisperse long linear chains [51],

$$\lambda_{0R} = \frac{\lambda_{0d}}{3Z}\,, \tag{4.10}$$

Table 4.3: Old relaxation spectrum of iPP2 at $T_{ref} = 135\,^{\circ}\mathrm{C}$.

T [°C]	a_T	b_T	i	G_i [$10^4\,\mathrm{Pa\,s}$]	$\lambda_{0d,i}$ [s]
135	1	1	1	7.96	0.01
145	0.72391	0.98122	2	3.998	0.06
155	0.51719	0.97277	3	1.533	0.36
165	0.38309	1.0216	4	0.344	2.16
175	0.26861	0.91455	5	0.0356	12.9
190	0.20227	0.93897	6	0.00368	77.8
205	0.15372	0.94554	WLF parameters		
220	0.11812	0.97183			
235	0.09547	0.89108	T_{ref} [°C]	c_1	c_2 [K]
250	0.07241	0.91455	135	3.159	198.1

in which they took $Z = M_w/M_e$ as a characteristic number of entanglements for the high-end tail of the molecular weight distribution; M_e is the average molecular weight between entanglements. The relaxation times of the three iPPs are reported in Table 4.2.

Eq. (4.10) is commonly applied in FIC studies, although it disregards the effect of shorter chains on the relaxation dynamics of the HMW fraction through constraint release. For bimodal blends, the Struglinski–Graessley criterion $Z_{HMW}/Z_{LMW}^3 \ll 0.1$ [180] can be used to justify Eq. (4.10) [18]. Here Z_{HMW} and Z_{LMW} are the molecular weights of the high and low molecular weight components, respectively, in units of M_e. A similar criterion for polydisperse melts is lacking. For a discussion of issues, related to the determination of characteristic HMW relaxation times in polydisperse melts, we refer to Van Meerveld *et al.* [195].

As an alternative to Eq. (4.10), the longest Rouse time is determined by fitting a multi-mode Rolie-Poly model to uniaxial extensional viscosity data for iPP2. These were supplied by Borealis. Inspection of the transient linear viscoelastic extensional viscosity, calculated with the relaxation spectrum reported by Housmans *et al.* [97], reveals a systematic underprediction of the data by approximately a factor of two. A previously determined spectrum for iPP2 [J.F. Vega, personal communication] does give a linear viscoelastic extensional viscosity curve in agreement with the data before strain hardening sets in. We attribute this to a difference between batches of the same iPP grade. Both relaxation spectra consist of six modes. The main differences are in the moduli, whereas the relaxation times are nearly identical. Vega's rheological measurements, summarized in Table 4.3, were done around the same time as the FIC experiments on iPP2 at 135°C [98], which are used here to compare model results with the longest Rouse time determined by the two different methods.

Likhtman and Graham [130] found that, to compensate for the overprediction of the steady-state shear stress and first normal stress difference in fast shear flows, they had to take $\beta = 0$.

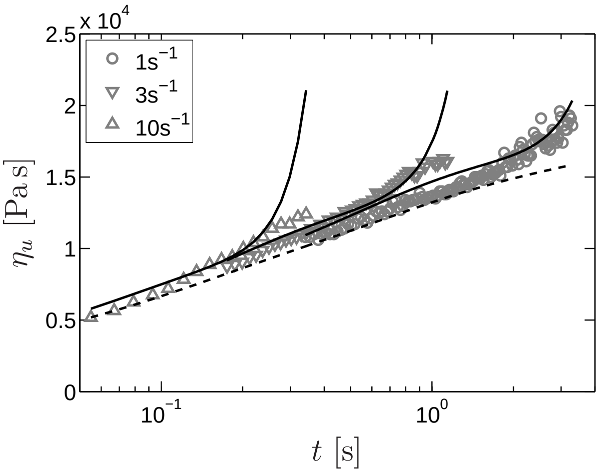

Figure 4.1: Symbols: uniaxial extensional viscosity data at $T = 180°$C for different strain rates. Lines: six-mode Rolie-Poly model with three stretching modes ($\lambda_{0R,4} = 0.04\,\mathrm{s}$, $\lambda_{0R,5} = 0.3\,\mathrm{s}$, $\lambda_{0R,6} = 2\,\mathrm{s}$). Dashed line: linear viscoelastic response.

This was not the case in the full Graham–Likhtman and Milner–McLeish (GLaMM) model [72] and therefore, according to the authors, it should not be concluded that convective constraint release was insignificant. We also find that $\beta = 0$ gives the best results. The remaining free parameters are then the Rouse times $\lambda_{0R,i}$.

The extensional viscosities, measured at four different strain rates, show minor strain hardening. The data for the lowest strain rate ($\dot{\epsilon} = 0.3\,\mathrm{s}^{-1}$) are excluded from the fitting procedure, since the calculated extensional viscosity always falls within the rather high scatter of these data. The other measurements are shown in Figure 4.1. The Rolie-Poly model predicts a much too strong strain hardening at the two highest rates ($\dot{\epsilon} = 3\,\mathrm{s}^{-1}$ and $\dot{\epsilon} = 10\,\mathrm{s}^{-1}$). The data for $\dot{\epsilon} = 1\,\mathrm{s}^{-1}$ can be fitted reasonably well when only the slowest mode is described by Eq. (4.5) while for the other modes the non-stretching Rolie-Poly model ([130] and Appendix 4A) is used. Two additional stretching modes are sufficient to improve the fits of the other data, in terms of the onset of strain hardening. The strong strain hardening, predicted at longer times, cannot be prevented. It turns out that the result for $\dot{\epsilon} = 1\,\mathrm{s}^{-1}$ is not affected much by these additional stretching modes, so we obtain a unique longest Rouse time, $\lambda_{0R,6} = 2\,\mathrm{s}$.

The uniaxial extension experiments were done at $T = 180\,°\mathrm{C}$. A time-temperature shift to $T = 138\,°\mathrm{C}$, with the Williams–Landel–Ferry (WLF) parameters given in Table 4.3, yields $\lambda_{0R,6} = 7\,\mathrm{s}$. This is much longer than the $0.27\,\mathrm{s}$ obtained from Eq. (4.10) and reported in Table 4.2. We have no physical explanation for this difference, but it is nevertheless interesting to test the effect of a variation in the Rouse time on the results of our flow-enhanced nucleation model.

4.3 Results and Discussion

The outline of this part is as follows. In Sections 4.3.1 to 4.3.3, we look at a few typical aspects of spherulitic structure development, as observed in the experiments described above and reported by other authors. The model from Section 4.1 is adapted based on these observations. It is validated by the experimental data for iPP2 from Table 4.1 and, in Appendix 4B, by the data of Housmans *et al.* [97] for all three materials. In Section 4.3.4, the sensitivity of the model parameters to the longest Rouse time estimate is investigated.

4.3.1 Interference of flow with nucleation

Microscopic pictures show that all spherulites became visible at approximately the same time (i.e. within a few seconds) shortly after the cessation of flow, and that their diameters were nearly equal. The same result was reported by Stadlbauer *et al.* [175] for short-term uniaxial extension of two different iPP melts. The data from our group, summarized in Table 4.1, prove that these observations are not simply a consequence of the shear time being too short to see any spherulites appear during flow and to end up with an observable distribution of diameters. The resolution of the optical microscope was $2\,\mu\mathrm{m}$. Four experiments can be identified in which the diameter of the earliest spherulites, grown from precursors nucleated directly after reaching the crystallization temperature at $t = 0$, would have exceeded this limit before the end of the shear period at $t = t_s$. The diameter of these spherulites at $t = t_s$ is given in the last column of Table 4.1. If indeed, as the model discussed in Section 4.1 states, the creation of precursors were a sporadic process and if $\tau_{pn} = 0$, as in the quiescent melt, these spherulites would have become visible during the flow. Moreover, at least in these four experiments and possibly in some others as well, depending on the amount of precursors created during relaxation of the stress after the cessation of flow, a clear distribution of diameters should have been observed.

On the basis of these results, we assume that nucleation is impeded by flow. A possible explanation is that the flow makes it more difficult for folded-chain lamellae to form, since the deformed ends of the long chains, attached to a precursor, have to relax before they can fold. Consequently, during the flow, the creation of precursors is enhanced but the precursors are less easily nucleated. This assumption is supported by the work of Blundell, Mahendrasingam, and others on film drawing of poly(ethylene terephthalate) [25, 26, 134–137], poly(lactic acid) [138], and poly(ethylene terephthalate-*co*-isophthalate) copolymers [139]. They observed that, for high strain rates, no crystallinity developed until the moment when the draw ratio became constant, i.e. when the strain rate became zero. For lower strain rates, crystallization did start during flow. The onset of the fast drawing regime was correlated with the dynamics of chain stretch in the melt: when the strain rate was higher than the inverse of the stretch relaxation time, crystallization did not start until after cessation of flow.

The shear rates in the experiments of Housmans *et al.* [97] were chosen such that the Weissenberg number Wi_R, based on the Rouse time for each material in Table 4.2 as determined by Eq. (4.10), was always greater than one. In the experiments of Hristova *et al.* [98] on iPP2, using the same Rouse time, $Wi_R > 1$ for all shear rates except $\dot{\gamma} = 2\,\mathrm{s}^{-1}$. Based on the Rouse time fitted to the extensional viscosity data, all experiments fall in the stretching regime, $Wi_R > 1$. We therefore implement a step function,

$$\tau_{pn} = \begin{cases} \infty & \text{for} \quad \dot{\gamma} \neq 0 \\ 0 & \text{for} \quad \dot{\gamma} = 0 \end{cases} \tag{4.11}$$

to model the effect of flow on the nucleation process. According to Eq. (4.11), during the flow, precursors are created but not nucleated. When the flow is switched off, these precursors, and all precursors created afterwards, immediately become nuclei and the model has to be reformulated as explained in Appendix 3A. Of course, if the flow is applied for a sufficiently long time, sporadic nucleation will eventually be observed. Otherwise no crystallinity would develop in a continuous strong flow, which contradicts experimental evidence. A more realistic model for the dependence of τ_{pn} on the shear rate (and on the temperature) should be used in that case. However, it will be shown that Eq. (4.11) is a suitable approximation for the experiments considered here.

4.3.2 Dissolution of precursors

After cessation of flow, according to Eq. (4.11) the instantaneous nucleation of precursors prevents them from dissolving. During flow, we take $\tau_{pd} \to \infty$ since the time scale of dissolution of iPP precursors is much longer, already above the nominal melting temperature, than the shear times used here [6, 58]. The same is true for other polymers, like isotactic poly-1-butene [11] and isotactic polystyrene [12].

4.3.3 Role of orientation and stretch

It has been suggested that, whereas molecules have to be stretched to form threadlike precursors, increased orientation already enhances the creation of pointlike precursors under moderate flow conditions. Here the terms stretch and orientation are defined on the level of the primitive path of a chain, described by Kuhn segments. The stretch corresponds to orientation on the level of chain segments.

Coppola *et al.* [42] extended the free energy in the classical nucleation theory with a term due to orientation, which they derived from the constitutive model of Doi and Edwards [51]. Changes in the time scale of crystallization were captured quite well by the model. Van Meerveld *et al.* [195] presented a classification scheme for FIC experiments, in which different regimes were defined, based on the Weissenberg numbers associated with orientation and

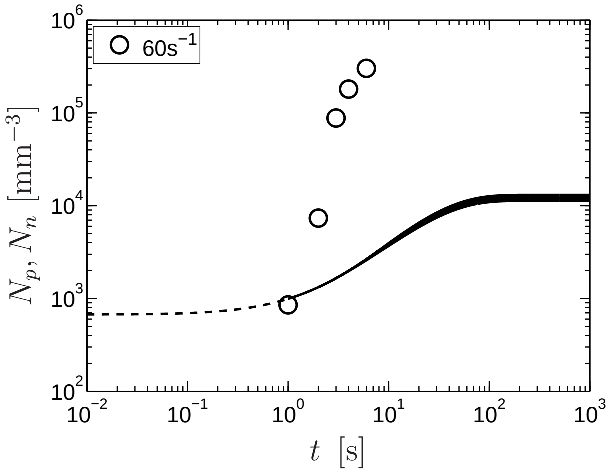

Figure 4.2: Number densities of precursors (dashed lines) and nuclei (solid lines) versus time and experimental number density of spherulites versus shear time (symbols) in iPP2 for $\dot{\gamma} = 60\,\mathrm{s}^{-1}$ at $T = 135\,^\circ\mathrm{C}$, according to the orientation-based creation model.

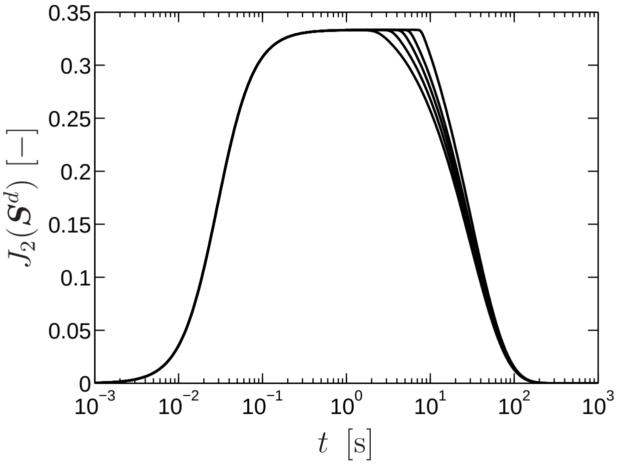

Figure 4.3: Evolution of orientation for the simulations in Figure 4.2.

stretch of the HMW tail of the melt (Wi_d and Wi_R, respectively). They discussed different methods to obtain the relevant relaxation times. Applying the classification scheme to a large number of experiments, they found that the number of spherulites was already increased for $Wi_d > 1-10$ while still $Wi_R < 1-10$. This seems to indicate that flow-induced orientation is indeed sufficient to create pointlike precursors. However, according to our model, the actual Weissenberg number related to the HMW chains, involved in the creation process, can increase tremendously during flow. Classification based on initial Weissenberg numbers should therefore be done with care, especially when long flow times are considered.

Based on the idea that orientation is sufficient to create flow-induced precursors, in Eq. (3.19) the second invariant of the deviatoric part of the elastic Finger tensor is replaced by the second invariant of the deviatoric part of the orientation tensor, see Eq. (3.3), which is

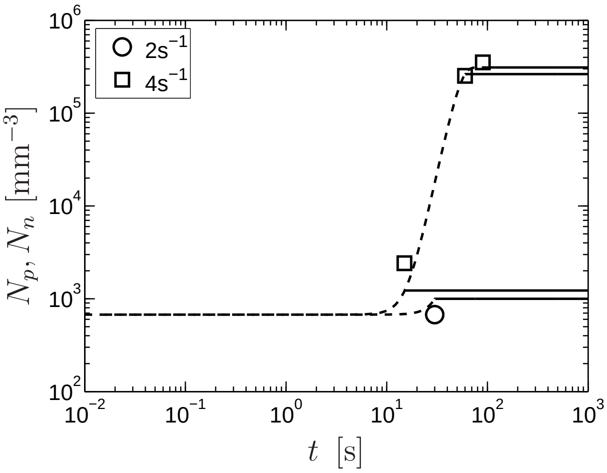

Figure 4.4: Number densities of precursors (dashed lines) and nuclei (solid lines) versus time and experimental number density of spherulites versus shear time (symbols) in iPP2 for $\dot{\gamma} = 2\,\mathrm{s}^{-1}$ and $\dot{\gamma} = 4\,\mathrm{s}^{-1}$ at $T = 135\,°\mathrm{C}$, according to the stretch-based creation model with the Rouse time estimated by Eq. (4.10).

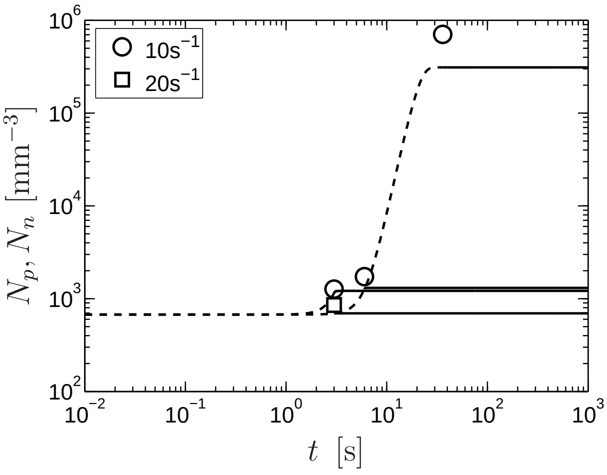

Figure 4.5: Number densities of precursors (dashed lines) and nuclei (solid lines) versus time and experimental number density of spherulites versus shear time (symbols) in iPP2 for $\dot{\gamma} = 10\,\mathrm{s}^{-1}$ and $\dot{\gamma} = 20\,\mathrm{s}^{-1}$ at $T = 135\,°\mathrm{C}$, according to the stretch-based creation model with the Rouse time estimated by Eq. (4.10).

given by

$$J_2\left(\boldsymbol{S}^d\right) = \frac{1}{2}\boldsymbol{S}^d : \boldsymbol{S}^d\,. \tag{4.12}$$

The results in Figure 4.2 show that the increase of the nucleation density as a function of shear time cannot be described in this way. As it turns out, even replacing the linear dependence of I_{pf} on $J_2\left(\boldsymbol{S}^d\right)$ by a power law does not make a noticeable difference. The reason can be deduced from Figure 4.3, showing the evolution of the orientation invariant.

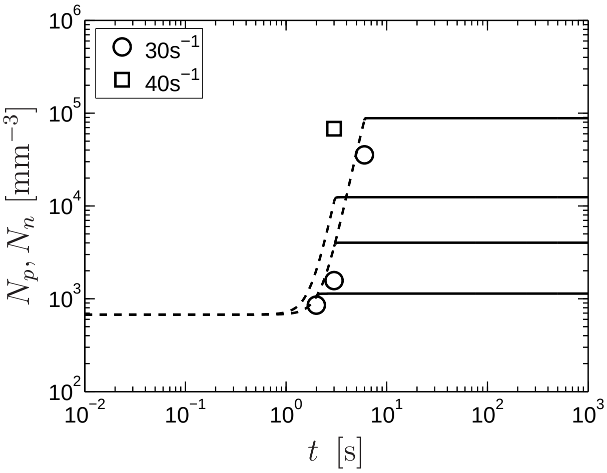

Figure 4.6: Number densities of precursors (dashed lines) and nuclei (solid lines) versus time and experimental number density of spherulites versus shear time (symbols) in iPP2 for $\dot{\gamma} = 30\,\mathrm{s}^{-1}$ and $\dot{\gamma} = 40\,\mathrm{s}^{-1}$ at $T = 135\,^\circ\mathrm{C}$, according to the stretch-based creation model with the Rouse time estimated by Eq. (4.10).

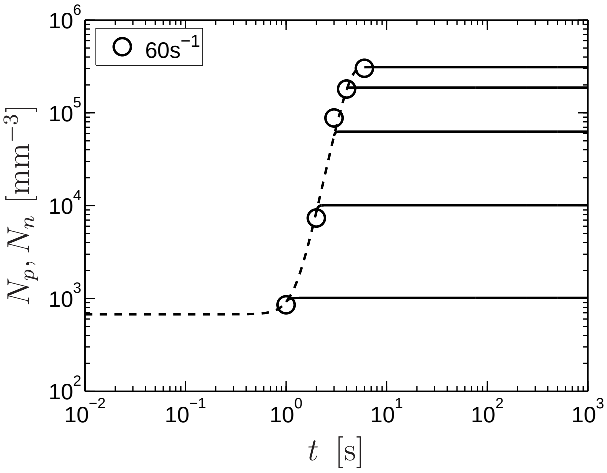

Figure 4.7: Number densities of precursors (dashed lines) and nuclei (solid lines) versus time and experimental number density of spherulites versus shear time (symbols) in iPP2 for $\dot{\gamma} = 60\,\mathrm{s}^{-1}$ at $T = 135\,^\circ\mathrm{C}$, according to the stretch-based creation model with the Rouse time estimated by Eq. (4.10).

The area under the curve, i.e. the flow-induced number density, is only mildly affected by an increase of the shear time. In Figures 4.2 and 4.3, $g_{0p} = 10^3\,\mathrm{mm}^{-3}\mathrm{s}^{-1}$ and $a = 10^2\,\mathrm{mm}^3$ were used. Similar results are obtained irrespective of the crosslinking parameter a. Hence, according to our model, orientation of the primitive path of the HMW chains is insufficient for the creation of flow-induced precursors.

In view of this result, Eq. (3.19) is replaced by

$$I_{pf} = g_p \left(\Lambda^m - 1 \right) \,, \tag{4.13}$$

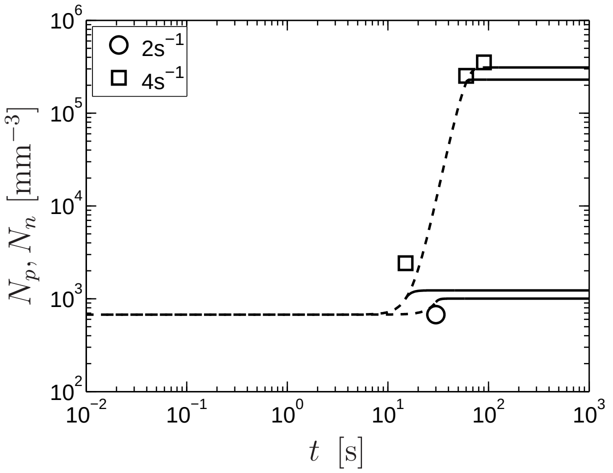

Figure 4.8: Number densities of precursors (dashed lines) and nuclei (solid lines) versus time and experimental number density of spherulites versus shear time (symbols) in iPP2 for $\dot{\gamma} = 2\,\mathrm{s}^{-1}$ and $\dot{\gamma} = 4\,\mathrm{s}^{-1}$ at $T = 135\,°\mathrm{C}$, according to the stretch-based creation model with the Rouse time fitted to extensional viscosity data.

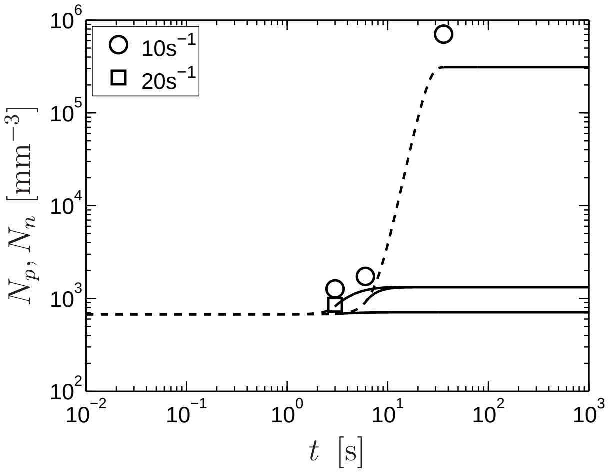

Figure 4.9: Number densities of precursors (dashed lines) and nuclei (solid lines) versus time and experimental number density of spherulites versus shear time (symbols) in iPP2 for $\dot{\gamma} = 10\,\mathrm{s}^{-1}$ and $\dot{\gamma} = 20\,\mathrm{s}^{-1}$ at $T = 135\,°\mathrm{C}$, according to the stretch-based creation model with the Rouse time fitted to extensional viscosity data.

with the stretch parameter Λ according to Eq. (3.4). Simulations with $m = 4$ give the best results (higher values do not lead to an improvement) and are shown in Figures 4.4 to 4.7. This stretch dependence agrees very well, up to $\Lambda \approx 3.5$, with the exponential relation found by Graham and Olmsted [73,75]. The parameters $g_{0p} = 1.4 \times 10^{-3}\,\mathrm{mm}^{-3}\mathrm{s}^{-1}$ and $a = 1.0 \times 10^3\,\mathrm{mm}^3$ were obtained by fitting all experiments simultaneously. $N_{f,max} = 3.1 \times 10^5\,\mathrm{mm}^{-3}$ was estimated from the experimental data for $\dot{\gamma} = 60\,\mathrm{s}^{-1}$ and used as a fixed input parameter.

For $m = 4$, the fit of the model to the experimental data is essentially the same as with Eq.

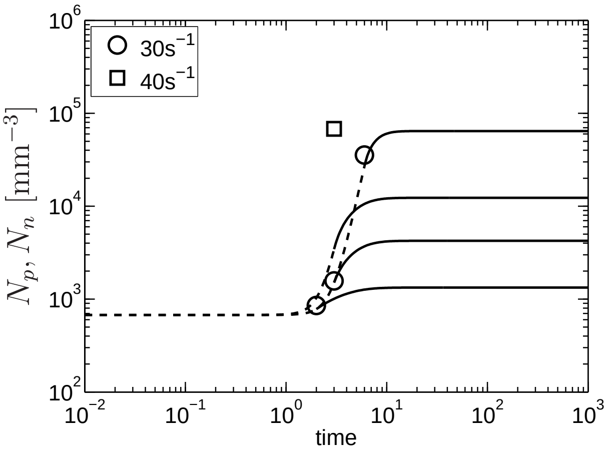

Figure 4.10: Number densities of precursors (dashed lines) and nuclei (solid lines) versus time and experimental number density of spherulites versus shear time (symbols) in iPP2 for $\dot{\gamma} = 30\,\mathrm{s}^{-1}$ and $\dot{\gamma} = 40\,\mathrm{s}^{-1}$ at $T = 135\,°\mathrm{C}$, according to the stretch-based creation model with the Rouse time fitted to extensional viscosity data.

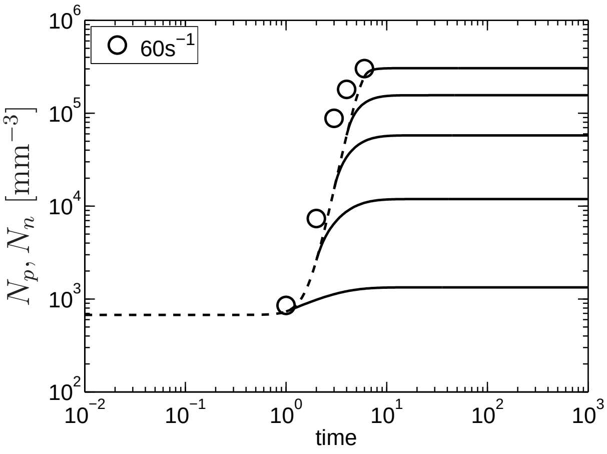

Figure 4.11: Number densities of precursors (dashed lines) and nuclei (solid lines) versus time and experimental number density of spherulites versus shear time (symbols) in iPP2 for $\dot{\gamma} = 60\,\mathrm{s}^{-1}$ at $T = 135\,°\mathrm{C}$, according to the stretch-based creation model with the Rouse time fitted to extensional viscosity data.

(3.19). This is because

$$J_2\left(\boldsymbol{B}_e^d\right) = 9\Lambda^4 J_2\left(\boldsymbol{S}^d\right) \tag{4.14}$$

and, as shown in Figure 4.3, $J_2\left(\boldsymbol{S}^d\right)$ hardly changes as a function of the shear time.

In Appendix 4B, the model with the stretch-based creation rate, Eq. (4.13) with $m = 4$, is applied to the experiments of Housmans *et al.* [97]. There also the relaxation times from Table 4.2 are used. For the experiments of Hristova *et al.* [98], we now investigate the influence of a difference in the characteristic Rouse time, estimated for the HMW fraction, on the simulation results.

4.3.4 Sensitivity to the longest Rouse time estimate

Figures 4.8 to 4.11 show the results of simulations with the longest reptation time from Table 4.3, which is approximately the same as the one obtained from the spectrum of Housmans *et al.* [97], and the longest Rouse time $\lambda_{0R} = 2\,\mathrm{s}$ as determined from the uniaxial extensional viscosity data. The parameters $g_{0p} = 2.5 \times 10^{-4}\,\mathrm{mm}^{-3}\mathrm{s}^{-1}$ and $a = 4.9\,\mathrm{mm}^3$ are obtained, again by fitting the number densities of spherulites for all shear rates. Especially the crosslinking parameter is very sensitive to a change in λ_{0R}. The results, in terms of the final number densities, are similar to those shown in Figures 4.4 to 4.7, obtained with the longest Rouse time determined by Eq. (4.10); see Table 4.2. The model parameters from both approaches are included in Table 4.5 in Appendix 4B for comparison.

The main difference occurs in the evolution of the number of flow-induced nuclei after flow. Due to Eq. (4.11) and the choice of the critical radius $R^* = 0$ in Eq. (4.7), the crosslinking effect vanishes at $t = t_s$. However, for a longer Rouse time, the stretch needs more time to relax (Figure 4.12) and consequently more flow-induced nuclei are formed after the flow has stopped. If $R^* > 0$, the flow-induced nuclei formed at times $t > t_s$ also act as physical crosslinks. The simulation results exhibit progressively worse agreement with the experimental data upon increasing R^*, in terms of the number densities as well as the distribution of sizes of spherulites, which becomes very broad, contrary to microscopic observations.

The local flow-enhanced nucleation model, presented in Chapter 3, predicts a negligible effect of the relaxing deformation after flow on the number density of spherulites, similar to the global model used here with $R^* = 0$. In the local description, flow-induced precursors as well as nuclei are allowed to act as physical crosslinks. However, after the cessation of flow, the enhanced creation is restricted to the spheres of influence of these flow-induced species (on the order of the coil volume of a HMW chain) and consequently does not lead to growth of separate spherulites.

4.4 Conclusions

A model for creation and nucleation of flow-enhanced precursors has been developed, based on a coupling of the characteristic reptation and Rouse times of the HMW chains with the number density of flow-induced precursors, similar to the recoverable strain-based model for oriented FIC [44,157,158,182,212,213]. The creation rate of flow-induced precursors is found to depend on the average stretch of the primitive path of the HMW chains. Thus the coupling

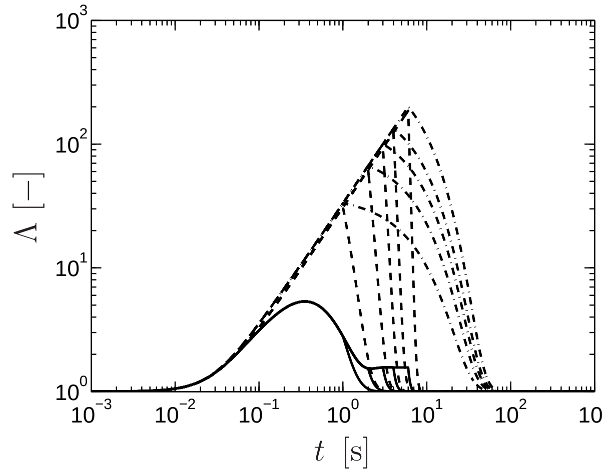

Figure 4.12: Evolution of stretch without flow-induced precursors (solid lines) and in the simulations of Figure 4.7 (dashed lines) and Figure 4.11 (dash-dotted lines) for iPP2, $\dot{\gamma} = 60\,\mathrm{s}^{-1}$ at $T = 135\,^{\circ}\mathrm{C}$.

of the relaxation time with early-stage structure development makes the creation of flow-induced precursors a self-enhancing process. This coupling is necessary to explain the effect of flow on the nucleation density. However, it leads to unrealistically high stretch values; the worst case is shown in Figure 4.12. A rheological model with finite extensibility [113, 176] might improve our results.

The global formulation of the flow-enhanced nucleation model (global in the sense that the HMW relaxation times are expressed as a function of the continuum average number density of flow-induced precursors) is not consistent with the original explanation that flow-induced species act as local physical crosslinks.

Experimental number densities of spherulites after short-term flow have been reproduced by the model with only two adjustable parameters. Thus it succeeds where the flow-enhanced nucleation model of Chapter 3, which is consistent with the concept of a local influence of flow-induced precursors and nuclei, fails. A possible explanation is that the number density of flow-induced precursors is much higher than that of the spherulites or, in other words, that most flow-induced precursors are dormant, i.e. unable to nucleate at the experimental temperature, but still affect the rheology of the melt. This is an interesting direction for future investigations.

In order to explain the absence of spherulites during flow as well as their narrow size distribution when they appear after cessation of flow, it must be concluded that the nucleation of precursors is impeded during flow. The fact that this is the case in the experiments considered here, with stretch-based Weissenberg numbers greater than one, is in accordance with experimental observations during film drawing of different polymers [25, 26, 134–139].

Appendices

4A Rolie-Poly and XPP constitutive equations

Eq. (4.5) gives the evolution equation for the elastic Finger tensor according to the Rolie-Poly model. Besides the reptation time λ_d and the Rouse time λ_R, it contains the parameters $\beta \in [0,1]$ and δ, controlling convective constraint release (CCR).

The eXtended Pom-Pom (XPP) model [199–202] is not used in this thesis, although Appendix 3C refers to pom-pom theories in general. Nevertheless, the derivation of a non-stretching version of the XPP model uncovers a few interesting analogies with other rheological models. The equations for the orientation tensor and the stretch parameter are given in Table 4.4a. These can be combined into one equation for the stress tensor (Table 4.4b). The version with modified stretching dynamics, as proposed by Van Meerveld [194], which has a higher numerical stability [199, 202], is presented here. The parameter α describes anisotropic relaxation similar to Giesekus [70].

Non-stretching Rolie-Poly model

For $\lambda_R \rightarrow 0$, the Rolie-Poly model reduces to [130]

$$\overset{\triangledown}{\boldsymbol{B}}_e + \frac{1}{\lambda_d}\left(\boldsymbol{B}_e - \boldsymbol{I}\right) + \frac{2}{3}\boldsymbol{D} : \boldsymbol{B}_e\left(\boldsymbol{B}_e + \beta\left(\boldsymbol{B}_e - \boldsymbol{I}\right)\right) = \boldsymbol{O}\,, \tag{4A1}$$

which is equivalent to the Doi−Edwards limit of Larson's partially extending convection model [123] if $\beta = 0$, i.e. if CCR is neglected.

Non-stretching XPP model

The limits

$$\lim_{\lambda_s \rightarrow 0} \dot{\Lambda} = 0 \quad \text{and} \quad \lim_{\lambda_s \rightarrow 0} \Lambda = 1 \tag{4A2}$$

are substituted in the orientation equation (Table 4.4) which then becomes

$$\overset{\triangledown}{\boldsymbol{S}} + 2\left(\boldsymbol{D} : \boldsymbol{S}\right)\boldsymbol{S} + \frac{1}{\lambda_{0b}}\left[3\alpha\boldsymbol{S}\cdot\boldsymbol{S} + \left(1 - \alpha - 3\alpha\boldsymbol{S} : \boldsymbol{S}\right)\boldsymbol{S} - \frac{1-\alpha}{3}\boldsymbol{I}\right] = \boldsymbol{O} \tag{4A3}$$

or, in terms of the extra stress tensor,

$$\overset{\triangledown}{\boldsymbol{\tau}} + \frac{2}{3G}\left(\boldsymbol{D} : \boldsymbol{\tau}\right)\left(\boldsymbol{\tau} + G\boldsymbol{I}\right) + \frac{\alpha}{\lambda_{0b}G}\left[\boldsymbol{\tau}\cdot\boldsymbol{\tau} - \frac{\boldsymbol{\tau} : \boldsymbol{\tau}}{3}\boldsymbol{I}\right] + \frac{\boldsymbol{\tau}}{\lambda_{0b}}\left[1 - \frac{\alpha\boldsymbol{\tau} : \boldsymbol{\tau}}{3G^2}\right] = 2G\boldsymbol{D}\,. \tag{4A4}$$

Table 4.4: The XPP model with modified stretch relaxation [199, 202].

a) Double-equation formulation

$$\boldsymbol{\tau} = G\left(3\Lambda^2 \boldsymbol{S} - \boldsymbol{I}\right)$$

$$\overset{\triangledown}{\boldsymbol{S}} + 2\left(\boldsymbol{D} : \boldsymbol{S}\right)\boldsymbol{S} + \tfrac{1}{\lambda_{0b}\Lambda^2}\left[3\alpha\Lambda^4 \boldsymbol{S}\cdot\boldsymbol{S} + \left(1 - \alpha - 3\alpha\Lambda^4 \boldsymbol{S} : \boldsymbol{S}\right)\boldsymbol{S} - \tfrac{1-\alpha}{3}\boldsymbol{I}\right] = \boldsymbol{O}$$

$$\dot{\Lambda} = \left(\boldsymbol{D} : \boldsymbol{S}\right)\Lambda - \tfrac{1}{\lambda_s}\left(\Lambda - \tfrac{1}{\Lambda}\right) \quad , \quad \lambda_s = \lambda_{0s}\mathrm{e}^{-\frac{2}{q}(\Lambda-1)}$$

b) Single-equation formulation

$$\overset{\triangledown}{\boldsymbol{\tau}} + \boldsymbol{\lambda}^{-1}\cdot\boldsymbol{\tau} = 2G\boldsymbol{D}$$

$$\boldsymbol{\lambda}^{-1} = \tfrac{1}{\lambda_{0b}\Lambda^2}\left[\tfrac{\alpha}{G}\boldsymbol{\tau} + f^{-1}\boldsymbol{I} + G\left(f^{-1} - 1\right)\boldsymbol{\tau}^{-1}\right]$$

$$\tfrac{1}{\lambda_{0b} f} = \tfrac{2}{\lambda_s}\left(1 - \tfrac{1}{\Lambda^2}\right) + \tfrac{1}{\lambda_{0b}\Lambda^2}\left[1 - \tfrac{\alpha\boldsymbol{\tau}:\boldsymbol{\tau}}{3G^2}\right]$$

$$\Lambda = \sqrt{1 + \tfrac{\mathrm{tr}(\boldsymbol{\tau})}{3G}} \quad , \quad \lambda_s = \lambda_{0s}\mathrm{e}^{-\frac{2}{q}(\Lambda-1)}$$

For $\alpha = 0$, the non-stretching XPP model also reduces to the Doi—Edwards limit of Larson's partially extending convection model [123]. The second term on the left-hand side of Eq. (4A4) is not immediately recognized in the single-equation XPP model (Table 4.4b). However, substitution of Eq. (4A2) in the stretch equation (Table 4.4a) yields

$$\lim_{\lambda_s \to 0} \frac{1}{\lambda_s}\left(1 - \frac{1}{\Lambda^2}\right) = \boldsymbol{D} : \boldsymbol{S}\,. \tag{4A5}$$

Using this result, Eq. (4A4) is easily derived from the single-equation XPP model.

On the other hand, when $\Lambda \to 1$ because the deformation remains small, but λ_s does not vanish, the stretch term in the relaxation function of the single-equation XPP model goes to zero. Then, if $\alpha = 0$, the upper convected Maxwell model is obtained [200]. In the double-equation XPP model, $\boldsymbol{D} : \boldsymbol{S} \to \frac{1}{3}\mathrm{tr}(\boldsymbol{D}) = 0$ because $\boldsymbol{S} \to \frac{1}{3}\boldsymbol{I}$ for small deformations.

4B Simulations of FIC experiments of Housmans et al.

For the three materials listed in Table 4.2, only those experiments are considered in which the transition to oriented structure formation did not yet occur. Attempts to fit the number

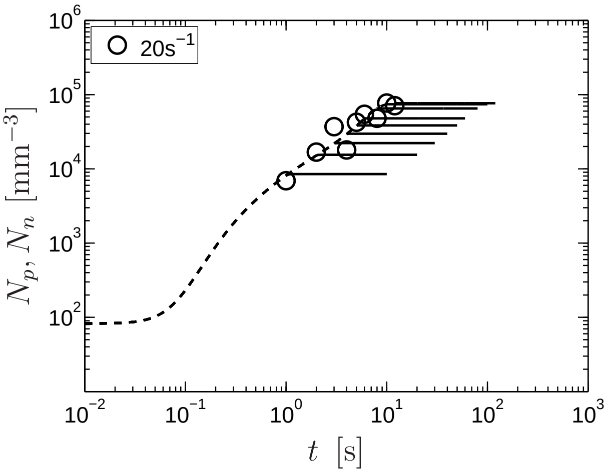

Figure 4.13: Number densities of precursors (dashed lines) and nuclei (solid lines) versus time and experimental number density of spherulites versus shear time (symbols) in iPP1.

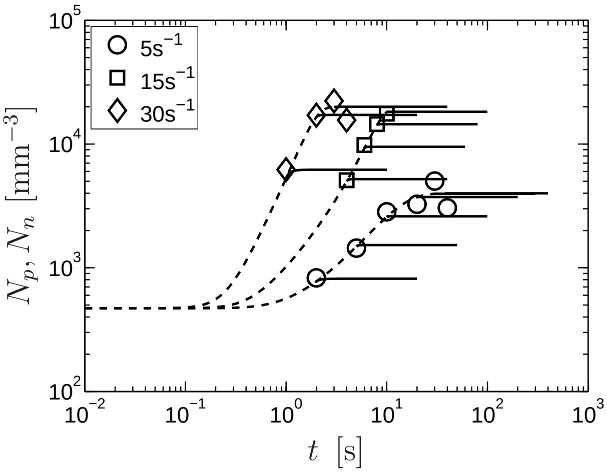

Figure 4.14: Number densities of precursors (dashed lines) and nuclei (solid lines) versus time and experimental number density of spherulites versus shear time (symbols) in iPP2.

densities of spherulites for all shear rates with the same parameters g_{0p} and a, as in Section 4.3 for the optical microscopy data of Hristova *et al.* [98], were not successful. Therefore individual results for each shear rate are presented in Figures 4.14 and 4.15. For iPP1 (Figure 4.13) only one shear rate is considered because, for the other one, the saturation regime was obscured by the transition to the oriented FIC regime and only one shear time was applied before this transition [97]. The model parameters are summarized in Table 4.5. The most conspicuous is g_{0p} for iPP1. This is much higher compared to the other materials due to the lower quiescent number density, determined by means of the suspension model of Chapter 2, for this material. Consequently, the flow-induced number densities in the experiments on iPP1 need a stronger increase relatively to the quiescent number density (governed by g_{0p}) than with respect to each other (governed by a).

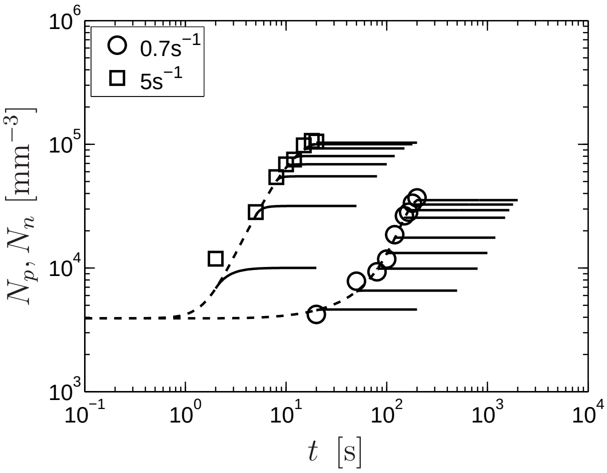

Figure 4.15: Number densities of precursors (dashed lines) and nuclei (solid lines) versus time and experimental number density of spherulites versus shear time (symbols) in iPP3.

Table 4.5: Model parameters for the three iPPs. Those at $T = 135\,°\mathrm{C}$ were fitted for all shear rates (Table 4.1) at once with $\lambda_{0R} = 0.29\,\mathrm{s}$ (top line) or $\lambda_{0R} = 7.7\,\mathrm{s}$ (bottom line) depending on the method to estimate the Rouse time, as explained in Section 4.2.2.

		$T = 138\,°\mathrm{C}$		$T = 135\,°\mathrm{C}$	
iPP	$\dot{\gamma}$ [s^{-1}]	g_{0p} [mm^{-3}s]	a [mm^3]	g_{0p} [mm^{-3}s]	a [mm^3]
1	20	2.0×10^3	4.0×10^{-4}		
2	5	39	7.3×10^{-3}	1.4×10^{-3} 2.5×10^{-4}	1.0×10^3 4.9
	15	23	2.8×10^{-3}		
	30	28	7.9×10^{-4}		
3	0.7	6.8	6.0×10^{-3}		
	5	28	6.0×10^{-5}		

Chapter five

Temperature effects on flow-enhanced nucleation and its saturation

---

Abstract

The flow-enhanced nucleation model from Chapter 4 is applied to short-term shear experiments on a poly-1-butene melt. Number densities for different combinations of shear rate, shear time, and temperature are reproduced quite well by the model with only two adjustable parameters. The influence of temperature on the creation and saturation of flow-induced precursors is investigated. In accordance with Chapter 4, the importance of stretch, rather than orientation, of the high-molecular weight (HMW) tail of the melt is evident.

Table 5.1: Properties of iP1B and experimental conditions [14, 16].

T_{m1} [°C]	M_w [kg/mol]	M_w/M_n	T [°C]	$\dot{\gamma}$ [s^{-1}]			λ_{0d} [s]	λ_{0R} [s]
				△	□	▽		
112.8	176	5.7	93	0.1	1	5	4.92	0.17
T_{m2} [°C]	$Z = M_w/M_e$	M_z/M_w	98	0.1	1	10	3.99	0.14
			100.5	1	5	10	3.61	0.12
110.7	9.78	2.1	103	1	5	10	3.26	0.11

5.1 Introduction and outline

Isotactic poly-1-butene (iP1B) has been used in several flow-induced crystallization studies [1,3,11,13,14,30,31,77–79,209]. Recent experiments by Baert [16] demonstrate that in iP1B the same kind of saturation of pointlike nucleation occurs as in isotactic polypropylene [97]. In this chapter, these experiments are compared to simulations with the model from Chapter 4. Similar results are obtained, but more insight is gained into the temperature dependencies of creation and saturation of flow-induced precursors.

The concept of a critical molecular weight, related to a critical Weissenberg number, for pointlike precursor creation is tested analytically. It turns out that, for temperatures below but not too close to the nominal melting point, the shear-rate dependence of the saturated number density of flow-induced precursors and nuclei $N_{f,max}$ agrees with a critical Weissenberg number based on stretching dynamics. This supports the concept of a stretch-dependent creation rate I_{pf}, combined with the idea that saturation is due to depletion of chains above the critical molecular weight. However, the number of these chains is many orders of magnitude higher than the experimental number densities of spherulites. This means that only a tiny fraction of those chains, long enough to be stretched by the flow, actually give rise to the creation of precursors.

5.2 Experiments

5.2.1 Flow-enhanced nucleation

Similar to the experiments of Hristova *et al.* [98], discussed in Chapter 4, the short-term shearing protocol was applied, using a Linkam shear cell, and number densities of spherulites were determined using Eq. (4.9) [66],

$$N_{sph}\ \left[\mathrm{mm}^{-3}\right] = \left(N_{sph}\ \left[\mathrm{mm}^{-2}\right]\right)^{3/2} . \tag{5.1}$$

Different combinations of shear rate, shearing time, and temperature were investigated. Oriented structures, typically about $100\,\mu\mathrm{m}$ in length, were observed at the highest shear rates. These were quickly overgrown by spherulites in greater numbers; see also Baert *et al.* [13]. Only the spherulites were counted. Quiescent number densities were not determined, since they are so low that this cannot be done accurately. In all simulations in this chapter, the initial, quiescent number density of precursors is taken equal to $10^{-1}\,\mathrm{mm}^{-3}$. The simulation results are very insensitive to variations in this value.

5.2.2 Rheological characterization

The iP1B used in this study, PB0400 from Basell, was characterized by Baert *et al.* [13]; see their supporting information. The reptation time of the HMW fraction was defined as the inverse of the frequency where the terminal regime ($G' \sim \omega^2$ and $G'' \sim \omega$) in small-amplitude oscillatory shear measurements was reached. The corresponding HMW Rouse time was estimated by Eq. (4.10),

$$\lambda_{0R} = \frac{\lambda_{0d}}{3Z}\,, \tag{5.2}$$

with $Z = M_w/M_e$. The relaxation times are included in Table 5.1.

5.3 Results and discussion

5.3.1 Flow-enhanced nucleation

The results of the globally formulated model, introduced in Chapter 4, are shown in Figures 5.1–5.4. The same conclusions can be drawn as in that chapter. Again it turns out that a dependence of the precursor creation rate on orientation of the HMW chains is unable to describe the effect of an increase in shear rate or shear time. The results shown are obtained with a fourth-order dependence on the stretch parameter, Eq. (4.13) with $m = 4$. A higher exponent m does not improve the results and a linear dependence on the second invariant of the deviatoric elastic Finger tensor works equally well.

As seen in Figures 5.1–5.4, the saturated number density increases as a function of the shear rate. The measured values of $N_{f,max}$ are used as input for the model. The kinetic parameter g_{0p} and the 'crosslinking' parameter a were first fitted to the experiments with $\dot{\gamma} = 0.1\,\mathrm{s}^{-1}$ at $T = 93\,^\circ\mathrm{C}$ and $T = 98\,^\circ\mathrm{C}$. The same a was enforced, whereas g_{0p} was allowed to take a different value for each temperature. The reason for this was that g_{0p} is a kinetic parameter, which is expected to be temperature-dependent, contrary to the structural parameter a. The values obtained suggested a temperature dependence, described by the rheological shift

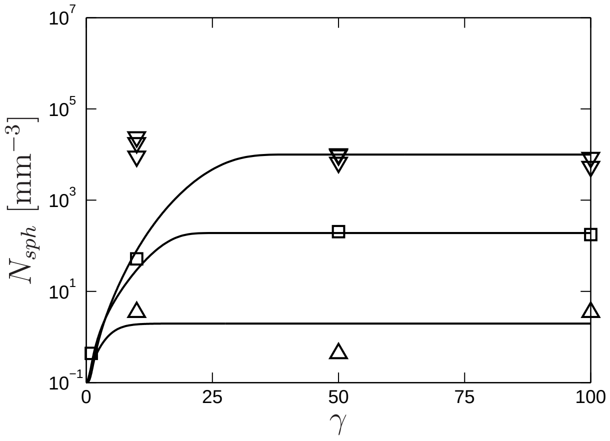

Figure 5.1: Final number density of spherulites as a function of shear strain for different shear rates (symbols, Table 5.1) at $T = 93\,°\mathrm{C}$. Lines: simulations.

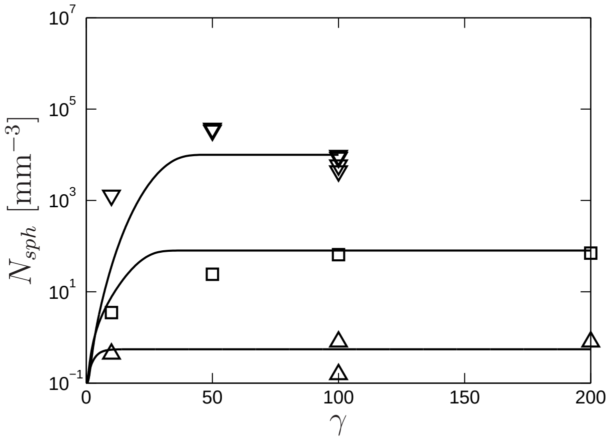

Figure 5.2: Final number density of spherulites as a function of shear strain for different shear rates (symbols, Table 5.1) at $T = 98\,°\mathrm{C}$. Lines: simulations.

factor,

$$g_{0p}(T) = a_T(T, T_{ref})g_{0p}(T_{ref})\,. \tag{5.3}$$

This temperature dependence was then prescribed and the same experiments were fitted again. The parameters thus obtained, $g_{0p}(93\,°\mathrm{C}) = 1.9\,\mathrm{mm}^{-3}\mathrm{s}^{-1}$ and $a = 1.4\,\mathrm{mm}^3$, are used in Figures 5.1–5.4 to predict the data at all other shear rates, shear times, and temperatures. It is seen that this works quite well, except for very fast flows, where saturation occurs almost immediately. This may be related to the appearance of short oriented crystallites in these experiments, which are eventually overgrown by spherulites, but which may locally alter the rheology of the melt. See also the optical micrographs by Baert and Van Puyvelde [13].

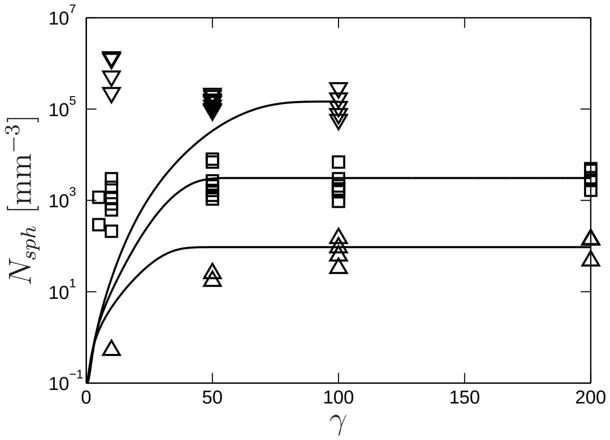

Figure 5.3: Final number density of spherulites as a function of shear strain for different shear rates (symbols, Table 5.1) at $T = 100.5\,°\mathrm{C}$. Lines: simulations.

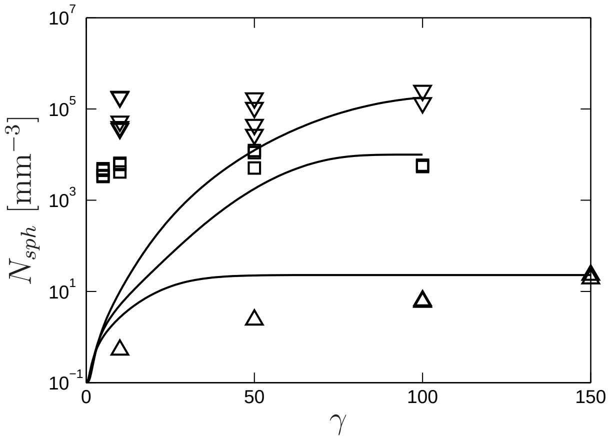

Figure 5.4: Final number density of spherulites as a function of shear strain for different shear rates (symbols, Table 5.1) at $T = 103\,°\mathrm{C}$. Lines: simulations.

5.3.2 Saturation

The objective of this section is to verify the idea that the saturation phenomenon observed is caused by depletion of chains above a critical molecular weight, which undergo sufficient orientation or stretching to create flow-induced precursors. If this is true, then $N_{f,max}$ should be proportional to the number density of chains in this HMW tail of the molecular weight distribution,

$$N_{HMW}(T,\dot{\gamma}) = \rho(T) N_A \int_{M^*(T,\dot{\gamma})}^{\infty} \frac{w(M)}{M} dM = \frac{\rho(T) N_A}{M_n} \int_{M^*(T,\dot{\gamma})}^{\infty} n(M) dM\,. \tag{5.4}$$

Here ρ is the density, N_A is Avogadro's number, $w(M)$ and $n(M)$ are the weight fraction and the number fraction of the distribution, respectively, and M^* is the critical molecular weight, marking the lower bound of the HMW tail, which should be related to a critical Weissenberg number.

Theoretical analysis

For a specific molecular weight M in a distribution, the initial Weissenberg number is written in the following form,

$$Wi_k(T,M) = \dot{\gamma}\lambda_{0k} = \dot{\gamma}\xi_k a_T(T,T_{ref})\lambda_e(T_{ref})\left(\frac{M}{M_e}\right)^{\frac{\xi_k+3}{2}} \quad ; \quad k \in \{d,R\}\ , \tag{5.5}$$

where $\lambda_e(T_{ref})$ is the relaxation time of a strand between two entanglements at a reference temperature T_{ref} and

$$\xi_d = 3\,, \tag{5.6}$$
$$\xi_R = 1\,, \tag{5.7}$$

for the reptation-based and stretch-based Weissenberg number, respectively. The exponent $(\xi_d+3)/2 = 3$ is accurate for long chains. With the critical value Wi_k^*, the critical shear rate for molecular weight M can be defined,

$$\dot{\gamma}_k^*(T,M) = \frac{Wi_k^*}{\xi_k a_T(T,T_{ref})\lambda_e(T_{ref})}\left(\frac{M}{M_e}\right)^{-\frac{\xi_k+3}{2}}\ . \tag{5.8}$$

Conversely, the critical molecular weight for a prescribed shear rate is then

$$M_k^*(T,\dot{\gamma}) = M_e\left(\frac{Wi_k^*}{\dot{\gamma}\xi_k a_T(T,T_{ref})\lambda_e(T_{ref})}\right)^{\frac{2}{\xi_k+3}}\ , \tag{5.9}$$

which can be used to calculate N_{HMW} as a function of temperature and shear rate with Eq. (5.4). A few data are needed for this. The density $\rho(T)$ of iP1B is documented in [211]. We fit the data above the melting point and extrapolate them to the experimental temperatures of the undercooled melts. The average molecular weight between entanglements is $M_e = 18\,\mathrm{kg/mol}$ [14]. The relaxation time λ_e is

$$\lambda_e = \frac{\lambda_{0d}}{3Z^3}\,. \tag{5.10}$$

Again, following Baert *et al.* [14], taking $Z = M_w/M_e$ as an average of the HMW tail, we find relaxation times on the order of $10^{-3}\,\mathrm{s}$ at the experimental temperatures. However, this Z is probably lower than the real average of the HMW tail. Therefore λ_e is used as an adjustable parameter, taking the estimates from Eq. (5.10) as a guideline. These are upper

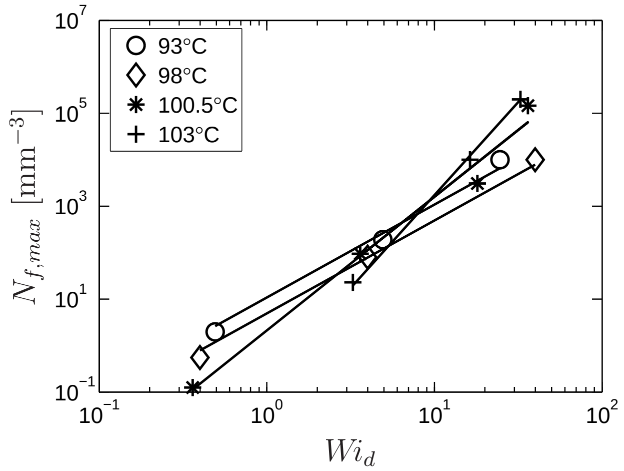

Figure 5.5: Saturated flow-induced number density versus reptation-based Weissenberg number at different temperatures. Lines are to guide the eye.

bounds if λ_{0d}, corresponding to the onset of the terminal regime as explained in Section 5.2.2, is an adequate measure of the reptation time of the HMW tail.

The unknown molecular weight distribution is assumed to be described by a log-normal distribution,

$$w(M) = \frac{1}{M\sigma\sqrt{2\pi}} \exp\left(\frac{-\left(\ln M - \mu\right)^2}{2\sigma^2}\right) , \tag{5.11}$$

which is completely determined by M_n and M_w. These are related to the mean μ and standard deviation σ as follows,

$$M_w = M_n \exp\left(\sigma^2\right) = \exp\left(\mu + \frac{\sigma^2}{2}\right) . \tag{5.12}$$

Since M_z is known (see Table 5.1) the second moment of the real $w(M)$ can be calculated, $M_w M_z = 6.51 \times 10^{10}$, and compared to the second moment of the log-normal distribution, $(\exp(\mu + \sigma^2))^2 = 1.77 \times 10^{11}$. Thus the log-normal distribution has a larger HMW tail. However, considering that ultra-HMW chains, present in very small amounts, are difficult to detect for example by gel permeation chromatography, and that our analysis is only qualitative, the agreement is reasonable.

Application to experiments

The modeling results in Chapter 4 and the present chapter suggest that flow-induced precursor creation is driven by stretch of the primitive path of a chain, i.e. orientation on the level of Kuhn segments, whereas mere orientation of the primitive path is insufficient.

This seems in contradiction with the analysis of a great number of FIC experiments by Van Meerveld *et al.* [195]. However, Figure 5.5 shows that $N_{f,max}$ is already increased by up to two decades for reptation-based Weissenberg numbers $1 < Wi_d < 10$. The corresponding stretch-based Weissenberg numbers are a factor $3Z = 29$ lower. The reason that the model correctly captures the strong effect of flow on the creation of precursors, even under these weak flow conditions, is that the reptation time and Rouse time of the HMW fraction are very sensitive to N_{pf}, according to Eq. (4.7), which feeds back into the creation rate. Initial Weissenberg numbers are therefore not representative of the orientation and stretching dynamics of this HMW fraction, which are enhanced tremendously. They can only be used to assess the critical initial conditions in the undisturbed melt, which are apparently related to orientation of the primitive path, in accordance with the results of Van Meerveld *et al.* [195].

Comparison of the experimental data for $\dot{\gamma} = 10\,\mathrm{s}^{-1}$ in Figures 5.1–5.4 reveals that the saturated number densities of spherulites at $T = 100.5\,^{\circ}\mathrm{C}$ and $T = 103\,^{\circ}\mathrm{C}$ are more than a decade higher than the one at $T = 98\,^{\circ}\mathrm{C}$. This seems in contradiction with the idea that saturation is caused by depletion of chains above a critical molecular weight M^*, since relaxation times are shorter at higher temperature, so the critical molecular weight would be higher, yielding a lower $N_{f,max}$; see Eq. (5.4). Figure 5.5 plots the saturation level as a function of the Weissenberg number (essentially the shear rate) for all four temperatures. A quadratic relation is found at $T = 93\,^{\circ}\mathrm{C}$ and $T = 98\,^{\circ}\mathrm{C}$, where, as expected, $N_{f,max}$ decreases with increasing temperature at the same shear rate. The quadratic shear rate dependence changes into a third-order power law at $T = 100.5\,^{\circ}\mathrm{C}$ and a fourth-order power law at $T = 103\,^{\circ}\mathrm{C}$. This causes a crossover in the temperature dependence, from a monotonic decrease of $N_{f,max}$ at low shear rates to a decrease followed by an increase at high shear rates.

For the two lowest temperatures, where the temperature dependence of $N_{f,max}$ is qualitatively as expected, the results of Eq. (5.4) are plotted, using Eqs. (5.5) and (5.9). With $k = R$, i.e. a stretch-based criterion, the quadratic shear rate dependence is predicted. See the solid curves in Figure 5.6. The entanglement relaxation time was set to $\lambda_e = 10^{-5}\,\mathrm{s}$ at $T = 93\,^{\circ}\mathrm{C}$. If Eq. (5.10) is used with the reptation time from Table 5.1, this corresponds to a molecular weight of $5.6M_w$, which seems a reasonable average for the HMW tail. The solid curves in Figure 5.6 had to be shifted up vertically by a factor 10^{-6} (for $T = 93\,^{\circ}\mathrm{C}$) and by a factor 5×10^{-7} (for $T = 98\,^{\circ}\mathrm{C}$) to fit the data. This implies that only a tiny fraction of chains above M_R^* take part in flow-induced precursors, or at least in active ones, which can nucleate at the temperature of the experiment. With $k = d$, i.e. a reptation-based criterion, the shear rate dependence is not predicted. The corresponding dashed curves were shifted up by one tenth of the factors used for the stretch-based criterion.

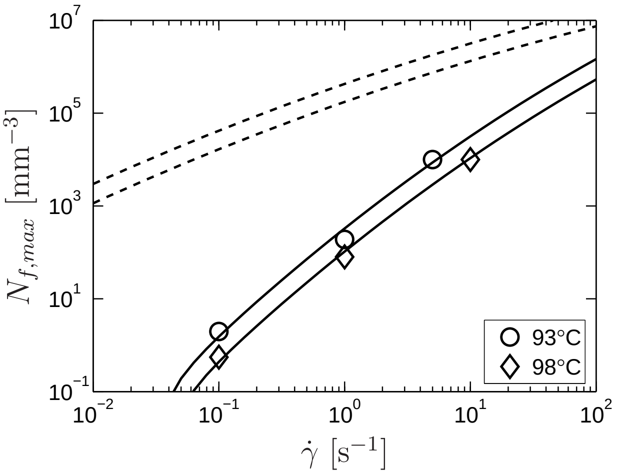

Figure 5.6: Saturated number density of flow-induced precursors and nuclei versus shear rate. Symbols: data from optical microscopy. Solid lines: stretch-based M_R^* criterion. Dashed lines: reptation-based M_d^* criterion.

5.4 Conclusions

Short-term shear FIC experiments on iP1B with different shear rates and shear times, applied at different temperatures, are simulated well by the model, developed in Chapter 4. The results are equivalent to those obtained in Chapter 4 for iPP. A few additional conclusions can be drawn, concerning the influence of temperature on the creation of flow-induced pointlike precursors.

First of all, the kinetic parameter g_{0p} (prefactor of the creation rate) scales with the rheological shift factor a_T. This suggests that segmental mobility plays an important role in the formation of flow-induced precursors. For a given stretch Λ, the creation rate is lower at higher temperature.

The saturated flow-induced number density $N_{f,max}$ increases as a function of the shear rate, which is expected, based on the idea that saturation occurs as a result of depletion of chains above a critical molecular weight. However, the shear rate dependence gradually changes from a second-order behavior at low temperatures to a fourth-order behavior at high temperatures, closer to the melting point of crystalline form II (T_{m2} in Table 5.1). This causes a crossover from a low shear rate regime, where the saturation level monotonically decreases as a function of temperature, to a high shear rate regime, where it passes through a minimum and starts to increase upon further increase of the temperature (Figure 5.5). The physical origin of this phenomenon, which has not been observed before, is unknown.

For the two lowest temperatures, the quadratic shear rate dependence agrees with a critical molecular weight criterion based on a critical stretch-based Weissenberg number.

Chapter six

Conclusions and prospects

6.1 Rheology of crystallizing melts in the late stages

The suspension-based modeling approach of Chapter 2 is able to capture, in a computationally inexpensive way, the evolution of rheological properties due to space filling. Only at low frequencies, at least to our knowledge, no adequate suspension model is available. This is an opportunity for future research. Another challenge is the development of an accurate method to determine the time-dependent volume fraction of oriented crystallites, which can be used as input in, for example, the 2D generalized self-consistent method.

An important conclusion is that the linear scaling of $G'(t)$ [67, 115], which is used very often in FIC studies, yields very inaccurate estimates of the degree of space filling. The logarithmic scaling [162] is comparable to the suspension modeling approach for spherulites, but does not discriminate between spherulitic and oriented volume fractions and cannot be improved to calculate both, or to use them as input and calculate $G'(t)$ and $G''(t)$.

6.2 Local versus global flow-enhanced nucleation

In Chapter 3, we developed a flow-enhanced nucleation model, in which the effect of flow-induced precursors and nuclei on the relaxation dynamics of the HMW chains is consistent with the idea that they act as physical crosslinks on these chains. Specifically, the longest reptation time and Rouse time are made dependent on the average number of flow-induced precursors and nuclei in domains with a radius r_v on the order of the radius of gyration of the HMW chains. This increase of relaxation times enhances the creation rate within these domains, which are therefore called incubators. The results in Section 3.6 show that the volume fraction of incubators nv is too small to explain the effect of flow on the experimental number density of spherulites N_{sph}. Since the final number of incubators n should correspond to N_{sph}, this can only be improved by increasing v.

In contrast to this local flow-enhanced nucleation model, the global model of Chapters 4 and 5 assumes that the creation of precursors is accelerated throughout the material, governed by a dependence of the longest reptation time and Rouse time on the continuum average number densities of flow-induced precursors and flow-induced nuclei with radius $R < R^*$. Thus, the global formulation implicitly assumes a homogeneous distribution, where the number densities inside and outside an incubator are equal, as depicted in Figure 3.1 on the right (i.e. the whole material acts as an incubator, $nv = 1$). Although, contrary to the local model, the global model successfully reproduces experimental number densities of spherulites, these are much too low to justify this assumption.

By setting $R^* = 0$, in combination with the instantaneous nucleation of precursors in the absence of flow, see Eq. (4.11), the creation process is practically switched off when the flow stops. The nearly constant N_{sph} observed in optical microscopy, see also [13,60,175], is thus imposed artificially in the global model, whereas it follows naturally from the local model of Chapter 3, because convection of flow-induced precursors and nuclei out of incubators is necessary for them to grow into separate spherulites.

It is important to note that, in the local formulation used in Chapter 3, the averaging of flow-induced precursors and nuclei over the incubators might have a large effect on the results. Essentially, in every time step, newly created incubators instantaneously gain a number of physical crosslinks at the expense of older incubators. However, due to the nonlinear effect of an increased relaxation time, a small number of incubators with many physical crosslinks might be much more effective than many incubators with few physical crosslinks. The multi-mode description, proposed in Appendix 3B, is therefore strongly recommended.

6.2.1 Role of dormant flow-induced precursors

At the end of Section 3.5, it was briefly explained how the local model for flow-enhanced nucleation may be generalized to include dormant flow-induced precursors, which do not nucleate until the temperature is lowered sufficiently. It is reasonable to assume that these have a similar effect on the HMW relaxation dynamics as active flow-induced precursors and nuclei, which could provide a foundation for the global model. If the average distance between adjacent dormant flow-induced precursors is on the order of the radius of gyration $\langle r_g^2 \rangle^{1/2}$ of the HMW chains or shorter, the physical crosslink density is the same locally and globally, as depicted on the right side of Figure 3.1, irrespective of the number density of active flow-induced precursors.

Janeschitz-Kriegl [108] plotted the logarithm of spherulite density versus temperature for different amounts of mechanical work, applied to an iPP melt in short-term shear. He then fitted linear curves through data for the same work, and extrapolated them towards lower temperatures. He found an approximate convergence of these ‘isoergons’ around $T = 75\,^\circ\mathrm{C}$, where $N_{sph} \sim 10^{18}\,\mathrm{m}^{-3}$, suggesting that this is the maximum amount of flow-induced precursors attainable at any temperature, dormant and active ones combined. The minimum average distance between nearest neighbors, based on this maximum number density, is then $d_{avg} = N_{sph}^{-1/3} = 1\,\mu\mathrm{m}$. This is still large compared to the radius of gyration $\langle r_g^2\rangle^{1/2} \sim 10\,\mathrm{nm}$. Therefore the presence of dormant flow-induced precursors seems insufficient to justify the global formulation of flow-enhanced nucleation, based on Eq. (4.7). Also note that the assumption of Janeschitz-Kriegl [108], that all dormant precursors are intrinsically present in the melt, does not fit in this picture, since then their effect on the relaxation dynamics would be there from the beginning.

Another possible explanation is that the HMW fraction forms a loose network, initially connected by entanglements only, which are partly replaced by flow-induced precursors, slowing down the relaxation of this network. This idea is certainly more plausible with $d_{avg} = 1\,\mu\mathrm{m}$, as derived here including dormant flow-induced precursors, then with $d_{avg} > 10\,\mu\mathrm{m}$, for typical number densities $N_{sph} < 10^{15}\,\mu\mathrm{m}$.

More experiments are needed to check whether $\log(N_{sph})$ is indeed linear in T for the same amount of work, especially at lower temperatures, since Janeschitz-Kriegl’s extrapolation to $T = 75\,^\circ\mathrm{C}$ was based on a limited amount of data in the relatively narrow range $140 \leqslant T \leqslant 160\,^\circ\mathrm{C}$. Crystallization during flow, causing changes in rheological properties as well as in the flow itself, becomes a problem when going to lower temperatures. Therefore the flow should be applied before cooling. Another problem at low temperatures may be that the number density of spherulites is too high to be determined with optical microscopy. The method of Housmans *et al.* [97], in which the number density is derived from rheological measurements by means of a suspension model, overcomes this problem.

For modeling of nonisothermal FIC processes, it is crucial to investigate how the distribution of dormant precursors versus activation temperature changes as a function of flow parameters, preferably ones closer related to molecular deformation than work.

6.3 FIC criteria: does work work for pointlike precursors?

The Weissenberg number has been used as a parameter to characterize transitions between FIC regimes, from quasi-quiescent crystallization (regime 1) to flow-enhanced pointlike nucleation (regime 2) and oriented structure formation (regime 3). See for example Acierno *et al.* [1] and Van Meerveld *et al.* [195]. Janeschitz-Kriegl and coworkers [107, 108, 175] showed that the number density of spherulites correlates with the mechanical work,

$$w(t) = \int_0^t \boldsymbol{\tau}(t') : \boldsymbol{D}(t')\,dt' \,. \tag{6.1}$$

While this definition of work is macroscopic, in the sense that it is related to the average conformation of all chains in the melt, it can be redefined in terms of the HMW chains by substituting the stress of the slowest mode $\boldsymbol{\tau}_M$ for the total stress $\boldsymbol{\tau}$ in Eq. (6.1).

Mykhaylyk *et al.* [146] showed that the onset of regime 3 can be characterized by a critical work w^*, which is independent on the strain rate as long as the latter exceeds the inverse Rouse time of the HMW chains, i.e. $Wi_R > 1$. The critical work was found to decrease with increasing concentration of these chains. These observations are supported by results of Housmans *et al.* [97]. Compared to a critical Weissenberg number, w^* has the advantage that it contains the effect of flow time in addition to the strain rate.

Kumaraswamy *et al.* [121] studied crystallization during and after pressure-driven shear flow. The stress, increasing linearly from the center to the wall of the flow cell, could be controlled to reach a constant level within $50\,\mathrm{ms}$ [119]. The same stress was applied at different temperatures. Consequently, the strain rate was constant but different at each temperature. Their results for isotactic polypropylene ($M_w \approx 300\,\mathrm{kg/mol}$, $6 < M_w/M_n < 8$) show an upturn in the birefringence during flow at $t = t_u \sim a_T$. This was correlated with the appearance of oriented crystallites in WAXD.

Under constant stress, the mechanical work is

$$w(T,t) = \boldsymbol{\tau} : \boldsymbol{D}(T)\, t = \frac{\boldsymbol{\tau} : \boldsymbol{\tau}\, t}{2\eta\,(T)}\,. \tag{6.2}$$

The time needed to reach a critical work w^* is then

$$t^*(T) = \frac{2\eta(T) w^*}{\boldsymbol{\tau} : \boldsymbol{\tau}} \sim \frac{a_T(T)}{b_T(T)}\,, \tag{6.3}$$

in accordance with the temperature dependence of t_u observed by Kumaraswamy *et al.* [121] if the variation of b_T over their experimental temperature range of 35 degrees was relatively small, as is normally the case. Although shear thinning is ignored, the viscosity being expressed as a function of temperature only, this simple result is remarkable.

When the same constant strain rate is applied at different temperatures,

$$w(T, t > t_{su}) = \left[\int_0^{t_{su}} \boldsymbol{\tau}(T,t')\, dt' + 2\eta(T)\boldsymbol{D}\,(t - t_{su})\right] : \boldsymbol{D}\,, \tag{6.4}$$

in which t_{su} is the startup time and $\boldsymbol{\tau}_{ss}$ is the stress in the steady state. Neglecting startup behavior, the work criterion yields

$$t^*(T) \approx \frac{w^*}{2\eta(T)\boldsymbol{D} : \boldsymbol{D}} \sim \frac{b_T(T)}{a_T(T)}\,. \tag{6.5}$$

This agrees with the temperature dependence of the creation rate prefactor in our global flow-enhanced nucleation model, $g_{0p} \sim a_T$, as obtained from simulations in Section 5.3.1.

Mykhaylyk *et al.* [146] explained the critical work for shish formation as follows. Again neglecting startup behavior, for a constant strain rate, mechanical work is the product of stress and strain: $w = \tau\gamma$. When $Wi_R > 1$, the role of stress is to stretch the HMW chains, while sufficient strain can bring these stretched chains together, allowing them to aggregate and form the shish structure. The local flow-enhanced nucleation model of Chapter 3 offers a different explanation. There strain is required for the convection of flow-induced precursors out of their incubators, after which they serve as incubators themselves. Large strain thus results in long, slender rows of incubators, while high stress (i.e. fast local creation processes) leads to high number densities of precursors along these rows. When these closely spaced precursors nucleate, they will grow into kebab-like lamellae. For lower number densities, the lamellae will have more freedom to splay and the resulting morphology will look like rows of spherulites. Examples can be seen in the works of Azzurri and Alfonso [12] and Elmoumni *et al.* [60], and Elmoumni and Winter [61] and were also observed in the optical microscopy experiments used in Chapter 4. Finally, as shown in Chapter 3, convection of flow-induced species out of incubators is also necessary to generate the kind of spherulite densities observed experimentally in regime 2.

6.4 Bimodal blends

Bimodal blends of low and high molecular weight components are often used in FIC studies, since they can reveal details about the role of HMW chains [18, 20, 88, 146, 171, 210]. Modeling of FIC of bimodal systems was done by Acierno *et al.* [3], based on the double reptation concept [49]. An alternative, based on work of Giesekus, is presented here.

Giesekus [69] wrote the evolution equation for the extra stress tensor $\boldsymbol{\tau}$ as

$$\overset{\triangledown}{\boldsymbol{\tau}} + \frac{1}{2\lambda_d}\left(\boldsymbol{\beta}\cdot\boldsymbol{\tau} + \boldsymbol{\tau}\cdot\boldsymbol{\beta}^T\right) = 2G\boldsymbol{D} \tag{6.6}$$

Here $\boldsymbol{\beta}$ is the mobility tensor, which is proportional to the inverse of the friction tensor in a bead-spring description of the chains [70]. The neo-Hookean expression, Eq. (3.1) with

$$\boldsymbol{\tau} = G\left(\boldsymbol{B}_e - \boldsymbol{I}\right) = G\left(3\Lambda^2\boldsymbol{S} - \boldsymbol{I}\right), \tag{6.7}$$

is used. The orientation tensor $\boldsymbol{S}$ and stretch parameter Λ are given by Eqs. (3.3) and (3.4), respectively. With Eq. (6.7), Eq. (6.6) can be split into separate evolution equations for the stretch,

$$\dot{\Lambda} = \Lambda\left(\boldsymbol{D}:\boldsymbol{S}\right) - \frac{1}{6\lambda_d\Lambda}\boldsymbol{\beta}:\left(3\Lambda^2\boldsymbol{S} - \boldsymbol{I}\right), \tag{6.8}$$

and the orientation,

$$\begin{aligned}\overset{\triangledown}{\boldsymbol{S}} &+ 2\left(\boldsymbol{D}:\boldsymbol{S}\right)\boldsymbol{S} - \frac{1}{3\lambda_d\Lambda^2}\boldsymbol{\beta}:\left(3\Lambda^2\boldsymbol{S}-\boldsymbol{I}\right)\boldsymbol{S}\\ &+ \frac{1}{6\lambda_d\Lambda^2}\left(\boldsymbol{\beta}\cdot\left(3\Lambda^2\boldsymbol{S}-\boldsymbol{I}\right)+\left(3\Lambda^2\boldsymbol{S}-\boldsymbol{I}\right)\cdot\boldsymbol{\beta}^T\right)=\boldsymbol{O}\,,\end{aligned} \tag{6.9}$$

in which Eq. (6.8) has been applied.

Departing from the evolution equation for $\boldsymbol{B}_e$, Eq. (3.2), we get

$$\dot{\Lambda} = \Lambda\left(\boldsymbol{D}-\boldsymbol{A}\right):\boldsymbol{S} \tag{6.10}$$

and

$$\overset{\triangledown}{\boldsymbol{S}} + 2\left[\left(\boldsymbol{D}-\boldsymbol{A}\right):\boldsymbol{S}\right]\boldsymbol{S} + \boldsymbol{A}\cdot\boldsymbol{S} + \boldsymbol{S}\cdot\boldsymbol{A}^T = \boldsymbol{O}\,. \tag{6.11}$$

See also Verbeeten *et al.* [200, 202]. This gives the following relation between the mobility tensor and the slip tensor,

$$\boldsymbol{A} = \frac{1}{2\lambda_d}\boldsymbol{\beta}\cdot\left(\boldsymbol{I}-\frac{1}{3\Lambda^2}\boldsymbol{S}^{-1}\right). \tag{6.12}$$

6.4.1 Multi-mode Giesekus model

Giesekus argued that the mobility tensor of any mode $i \in [1, M]$ should depend on the conformations of all modes $j \in [1, M]$. He proposed a linear relation,

$$\boldsymbol{\beta}_i = \boldsymbol{I} + \sum_{j=1}^{M} \alpha_{ij}\left(3\Lambda_j^2\boldsymbol{S}_j - \boldsymbol{I}\right)\,. \tag{6.13}$$

An M-mode model with interactions among chains of all lengths, hence among all modes, contains M^2 nonzero parameters α_{ij}. Since this is generally not practical, Giesekus restricted himself to the single-mode model. However, for bimodal blends of (nearly) monodisperse polymers, a two-mode model with at most four coupling parameters is attractive.

6.4.2 Multi-mode XPP model

Since the XPP model performs better than the Giesekus model for linear as well as branched polymer melts in different types of flow [200–202], it is worthwhile to formulate a coupled multi-mode XPP model. The mobility tensor of the single-mode (or uncoupled multi-mode) version is

$$\begin{aligned}\boldsymbol{\beta} &= \alpha\left(3\Lambda^2\boldsymbol{S}-\boldsymbol{I}\right)+\left(\frac{2\lambda_{0b}}{\lambda_s}\left[1-\frac{1}{\Lambda^2}\right]\right.\\ &+ \left.\frac{1}{3\Lambda^2}\left[3-\alpha\left(3\Lambda^2\boldsymbol{S}-\boldsymbol{I}\right):\left(3\Lambda^2\boldsymbol{S}-\boldsymbol{I}\right)\right]\right)\left(\boldsymbol{I}+\left(3\Lambda^2\boldsymbol{S}-\boldsymbol{I}\right)^{-1}\right)\\ &- \left(3\Lambda^2\boldsymbol{S}-\boldsymbol{I}\right)^{-1}\,. \end{aligned} \tag{6.14}$$

If this is substituted in Eqs. (6.8) and (6.9), the double-equation formulation of the single-mode XPP model is obtained (Table 4.4a). If it is substituted in Eq. (6.6), the single-equation formulation of the single-mode XPP model is obtained (Table 4.4b).

We derive the mobility tensor of mode i in an M-mode XPP model by demanding that it reduces to Eq. (6.14) for $M = 1$ and, additionally, that the stretch evolution of mode i is not affected directly by the other modes, i.e. that it is still described by the stretch equation in Table 4.4a. Using Eq. (6.8), this requirement can be expressed as

$$\boldsymbol{\beta}_i : \left(3\Lambda_i^2\boldsymbol{S}_i-\boldsymbol{I}\right)=\frac{6\lambda_{0b,i}}{\lambda_{s,i}}\left(\Lambda_i^2-1\right) \tag{6.15}$$

It is important to note that the other modes do influence Λ_i indirectly, through the orientation tensor $\boldsymbol{S}_i$, whose evolution is coupled to the orientation tensors of the other modes. The resulting mobility tensor is

$$\begin{aligned}\boldsymbol{\beta}_i &= \sum_{j=1}^{M}\alpha_{ij}\left(3\Lambda_j^2\boldsymbol{S}_j-\boldsymbol{I}\right)+\left(\frac{2\lambda_{0b,i}}{\lambda_{s,i}}\left[1-\frac{1}{\Lambda_i^2}\right]\right.\\ &+ \left.\frac{1}{3\Lambda_i^2}\left[3-\sum_{j=1}^{M}\alpha_{ij}\left(3\Lambda_j^2\boldsymbol{S}_j-\boldsymbol{S}_j-\boldsymbol{I}\right):\left(3\Lambda_i^2\boldsymbol{S}_i-\boldsymbol{I}\right)\right]\right)\left(\boldsymbol{I}+\left(3\Lambda_i^2\boldsymbol{S}_i-\boldsymbol{I}\right)^{-1}\right)\\ &- \left(3\Lambda_i^2\boldsymbol{S}_i-\boldsymbol{I}\right)^{-1}\,. \end{aligned} \tag{6.16}$$

With Eq. (6.12), this can be converted to an expression for the slip tensor A_i, which reduces to the result of Verbeeten *et al.* [202] for the uncoupled multi-mode XPP model.

If a very low concentration of HMW chains (mode 2) is added to a matrix of LMW chains (mode 1), so that both components are mainly surrounded by LMW chains, then $\alpha_{12} = \alpha_{22} = 0$. If, moreover, the LMW component is only weakly anisotropic, we may take $\alpha_{11} = 0$. The behavior of the resulting 2-mode XPP model in simple shear flow is illustrated in Figures 6.1 and 6.2. It is seen that mode 2 becomes more shear thinning as the coupling parameter α_{21} increases (Figure 6.1). The effect on the first normal stress difference is negligible (Figure 6.2).

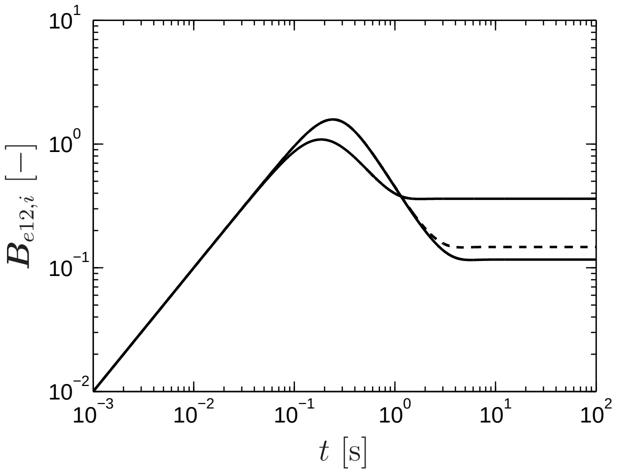

Figure 6.1: Shear component of the elastic Finger tensor for $\dot{\gamma} = 10\,\mathrm{s}^{-1}$ in a two-mode XPP model with $\lambda_{0b,1} = 5\,\mathrm{s}$, $\lambda_{0b,2} = 100\,\mathrm{s}$, $\lambda_{0s,1} = 0.1\,\mathrm{s}$, $\lambda_{0s,2} = 0.5\,\mathrm{s}$, $q_1 = q_2 = 1$ and $\alpha_{11} = \alpha_{12} = \alpha_{22} = 0$. Dashed lines: $\alpha_{21} = 0$, solid lines: $\alpha_{21} = 0.5$.

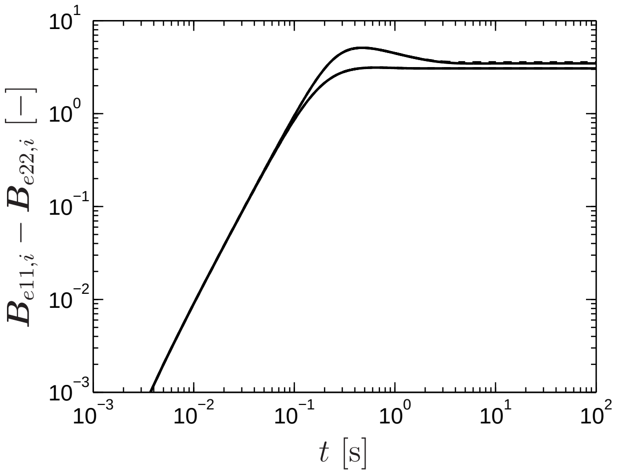

Figure 6.2: First normal component difference of the elastic Finger tensor for $\dot{\gamma} = 10\,\mathrm{s}^{-1}$ in a two-mode XPP model with $\lambda_{0b,1} = 5\,\mathrm{s}$, $\lambda_{0b,2} = 100\,\mathrm{s}$, $\lambda_{0s,1} = 0.1\,\mathrm{s}$, $\lambda_{0s,2} = 0.5\,\mathrm{s}$, $q_1 = q_2 = 1$ and $\alpha_{11} = \alpha_{12} = \alpha_{22} = 0$. Dashed lines: $\alpha_{21} = 0$, solid lines: $\alpha_{21} = 0.5$.

References

[1] S. Acierno, B. Palomba, H. H. Winter, and N. Grizzuti. Effect of molecular weight on the flow-induced crystallization of isotactic poly(1-butene). *Rheologica Acta*, 42:243–250, 2003.

[2] S. Acierno and N. Grizzuti. Measurements of the rheological behavior of a crystallizing polymer by an "inverse quenching" technique. *Journal of Rheology*, 47:563–576, 2003.

[3] S. Acierno, S. Coppola, and N. Grizzuti. Effects of molecular weight distribution on the flow-enhanced crystallization of poly(1-butene). *Journal of Rheology*, 52:551–566, 2008.

[4] A. Agbossou, A. Bergeret, K. Benzarti, and N. Albérola. Modelling of the viscoelastic behaviour of amorphous thermoplastic/glass beads composites based on the evaluation of the complex Poisson's ratio of the polymer matrix. *Journal of Materials Science*, 28:1963–1972, 1993.

[5] N. D. Albérola and P. Mélé. Viscoelasticity of polymers filled by rigid or soft particles: theory and experiment. *Polymer Composites*, 17:751–759, 1996.

[6] G. C. Alfonso and A. Ziabicki. Memory effects in isothermal crystallization II. Isotactic polypropylene. *Colloid and Polymer Science*, 273:317–323, 1995.

[7] B. K. Aral and D. M. Kalyon. Viscoelastic material functions of noncolloidal suspensions with spherical particles. *Journal of Rheology*, 41:599–620, 1997.

[8] M. Avrami. Kinetics of phase change I. General theory. *Journal of Chemical Physics*, 7:1103–1112, 1939.

[9] M. Avrami. Kinetics of phase change II. Transformation-time relations for random distribution of nuclei. *Journal of Chemical Physics*, 8:212–224, 1940.

[10] M. Avrami. Kinetics of phase change III. Granulation, phase change, and microstructure. *Journal of Chemical Physics*, 9:177–184, 1941.

[11] F. Azzurri and G. C. Alfonso. Lifetime of shear-induced crystal nucleation precursors. *Macromolecules*, 38:1723–1728, 2005.

[12] F. Azzurri and G. C. Alfonso. Insights into formation and relaxation of shear-induced nucleation precursors in isotactic polystyrene. *Macromolecules*, 41:1377–1383, 2008.

[13] J. Baert and P. van Puyvelde. Effect of molecular and processing parameters on the flow-induced crystallization of poly-1-butene. Part 1: kinetics and morphology. *Polymer*, 47:5871–5879, 2006.

[14] J. Baert, P. van Puyvelde, and F. Langouche. Flow-induced crystallization of PB-1: from the low shear rate region up to processing rates. *Macromolecules*, 39:9215–9222, 2006.

[15] J. Baert and P. van Puyvelde. Density fluctuations during the early stages of polymer crystallization: an overview. *Macromolecular Materials and Engineering*, 293:255–273, 2008.

[16] J. Baert. *Flow-Induced Crystallization of Poly-1-Butene*. PhD thesis, Katholieke Universiteit Leuven, 2009.

[17] D. G. H. Ballard, P. Cheshire, G. W. Longman, and J. Schelten. Small-angle neutron scattering studies of isotropic polypropylene. *Polymer*, 19:379–385, 1978.

[18] L. Balzano, N. Kukalyekar, S. Rastogi, G. W. M. Peters, and J. C. Chadwick. Crystallization and dissolution of flow-induced precursors. *Physical Review Letters*, 100:048302-1–048302-4, 2008.

[19] L. Balzano, S. Rastogi, and G. W. M. Peters. Crystallization and precursors during fast short-term shear. *Macromolecules*, 42:2088–2092, 2009.

[20] Z. Bashir, J. A. Odell, and A. Keller. Stiff and strong polyethylene with shish kebab morphology by continuous melt extrusion. *Journal of Materials Science*, 21:3993–4002, 1986.

[21] F. S. Bates and P. Wiltzius. Spinodal decomposition of a symmetric critical mixture of deuterated and protonated polymer. *Journal of Chemical Physics*, 91:3258–3274, 1989.

[22] Y. Benveniste. A new approach to the application of Mori–Tanaka's theory in composite materials. *Mechanics of Materials*, 6:147–157, 1987.

[23] A. N. Beris and B. J. Edwards. *Thermodynamics of Flowing Systems with Internal Microstructure*. Oxford University Press, Oxford, 1994.

[24] R. J. Blackwell, T. C. B. McLeish, and O. G. Harlen. Molecular drag-strain coupling in branched polymer melts. *Journal of Rheology*, 44:121–136, 2000.

[25] D. J. Blundell, D. H. MacKerron, W. Fuller, A. Mahendrasingam, C. Martin, R. J. Oldman, R. J. Rule, and C. Riekel. Characterization of strain-induced crystallization of poly(ethylene terephthalate) at fast draw rates using synchrotron radiation. *Polymer*, 37:3303–3311, 1996.

[26] D. J. Blundell, A. Mahendrasingam, C. Martin, W. Fuller, D. H. MacKerron, J. L. Harvie, R. J. Oldman, and C. Riekel. Orientation prior to crystallisation during drawing of poly(ethylene terephthalate). *Polymer*, 41:7793–7802, 2000.

[27] M. Bousmina. Rheology of polymer blends: linear model for viscoelastic emulsions. *Rheologica Acta*, 38:73–83, 1999.

[28] K. Boutahar, C. Carrot, and J. Guillet. Polypropylene during crystallization from the melt as a model for the rheology of molten-filled polymers. *Journal of Applied Polymer Science*, 60:103–114, 1996.

[29] K. Boutahar, C. Carrot, and J. Guillet. Crystallization of polyolefins from rheological measurements – relation between the transformed fraction and the dynamic moduli. *Macromolecules*, 31:1921–1929, 1998.

[30] J. Braun, D. Pillichshammer, G. Eder, and H. Janeschitz-Kriegl. Industrial solidification processes in polybutene-1. Part I–Quiescent melts. *Polymer Engineering and Science*, 43:180–187, 2003.

[31] J. Braun, H. Wippel, G. Eder, and H. Janeschitz-Kriegl. Industrial solidification processes in polybutene-1. Part II–Influence of shear flow. *Polymer Engineering and Science*, 43:188–203, 2003.

[32] D. A. G. Bruggeman. Berechnung verschiedener physikalischer Konstanten von heterogenen Substanzen I. Dielektrizitätskonstanten und Leitfähigkeiten der Mischkörper aus isotropen Substanzen. *Annalen der Physik 5. Folge*, 24:636–664, 665–679, 1935.

[33] B. Budiansky. On the elastic moduli of some heterogeneous materials. *Journal of the Mechanics and Physics of Solids*, 13:223–227, 1965.

[34] A. C. Bushman and A. J. McHugh. A continuum model for the dynamics of flow-induced crystallization. *Journal of Polymer Science, Part B: Polymer Physics*, 34:2393–2407, 1996.

[35] C. Carrot, J. Guillet, and K. Boutahar. Rheological behavior of a semi-crystalline polymer during isothermal crystallization. *Rheologica Acta*, 32:566–574, 1993.

[36] S. Z. D. Cheng and B. Lotz. Enthalpic and entropic origins of nucleation barriers during polymer crystallization: the Hoffman–Lauritzen theory and beyond. *Polymer*, 46:8662–8681, 2005.

[37] R. M. Christensen. Viscoelastic properties of heterogeneous media. *Journal of the Mechanics and Physics of Solids*, 17:23–41, 1969.

[38] R. M. Christensen and K. H. Lo. Solutions for effective shear properties in three phase sphere and cylinder models. *Journal of the Mechanics and Physics of Solids*, 27:315–330, 1979.

[39] R. M. Christensen and K. H. Lo. Erratum: Solutions for effective shear properties in three phase sphere and cylinder models. *Journal of the Mechanics and Physics of Solids*, 34:639, 1986.

[40] R. M. Christensen. A critical evaluation for a class of micro-mechanics models. *Journal of the Mechanics and Physics of Solids*, 38:379–404, 1990.

[41] I. Coccorullo, R. Pantani, and G. Titomanlio. Spherulitic nucleation and growth rates in an iPP under continuous shear flow. *Macromolecules*, 41:9214–9223, 2008.

[42] S. Coppola, N. Grizzuti, and P. L. Maffettone. Microrheological modeling of flow-induced crystallization. *Macromolecules*, 34:5030–5036, 2001.

[43] S. Coppola, S. Acierno, N. Grizzuti, and D. Vlassopoulos. Viscoelastic behavior of semicrystalline thermoplastic polymers during the early stages of crystallization. *Macromolecules*, 39:1507–1514, 2006.

[44] F. J. M. F. Custódio, R. J. A. Steenbakkers, P. D. Anderson, G. W. M. Peters, and H. E. H. Meijer. Model development and validation of crystallization behavior in injection molding prototype flows. *Macromolecular Theory and Simulations*, 2009. In print.

[45] D. R. Daniels, T. C. B. McLeish, R. Kant, B. J. Crosby, R. N. Young, A. Pryke, J. Allgaier, D. J. Groves, and R. J. Hawkins. Linear rheology of diluted linear, star and model long chain branched polymer melts. *Rheologica Acta*, 40:403–415, 2001.

[46] D. R. Daniels, T. C. B. McLeish, B. J. Crosby, R. N. Young, and C. M. Fernyhough. Molecular rheology of comb polymer melts. 1. Linear viscoelastic response. *Macromolecules*, 34:7025–7033, 2001.

[47] G. D'Avino, P. L. Maffettone, M. A. Hulsen, and G. W. M. Peters. A numerical method for simulating concentrated rigid particle suspensions in an elongational flow using a fixed grid. *Journal of Computational Physics*, 2007. Article in press.

[48] G. D'Avino, P. L. Maffettone, M. A. Hulsen, and G. W. M. Peters. Numerical simulation of planar elongational flow of concentrated rigid particle suspensions in a viscoelastic fluid. *Journal of Non-Newtonian Fluid Mechanics*, 150:65–79, 2007.

[49] J. des Cloizeaux. Relaxation of entangled polymers in melts. *Macromolecules*, 23:3992–4006, 1990.

[50] N. Devaux, B. Monasse, J.-M. Haudin, P. Moldenaers, and J. Vermant. Rheooptical study of the early stages of flow enhanced crystallization in isotactic polypropylene. *Rheologica Acta*, 43:210–222, 2004.

[51] M. Doi and S. F. Edwards. *The Theory of Polymer Dynamics*. Oxford University Press, Oxford, 1986.

[52] A. K. Doufas, I. S. Dairanieh, and A. J. McHugh. A continuum model for flow-induced crystallization of polymer melts. *Journal of Rheology*, 43:85–109, 1999.

[53] A. K. Doufas, A. J. McHugh, and C. Miller. Simulation of melt spinning including flow-induced crystallization. Part I: Model development and predictions. *Journal of Non-Newtonian Fluid Mechanics*, 92:27–66, 2000.

[54] A. K. Doufas, A. J. McHugh, C. Miller, and A. Immaneni. Simulation of melt spinning including flow-induced crystallization. Part II: Quantitative comparisons with industrial spinline data. *Journal of Non-Newtonian Fluid Mechanics*, 92:81–103, 2000.

[55] A. K. Doufas and A. J. McHugh. Simulation of film blowing including flow-induced crystallization. *Journal of Rheology*, 45:1085–1104, 2001.

[56] A. K. Doufas and A. J. McHugh. Simulation of melt spinning including flow-induced crystallization. Part III: Quantitative comparisons with PET spinline data. *Journal of Rheology*, 45:403–420, 2001.

[57] A. K. Doufas and A. J. McHugh. Two-dimensional simulation of melt spinning with a microstructural model for flow-induced crystallization. *Journal of Rheology*, 45:855–879, 2001.

[58] G. Eder, H. Janeschitz-Kriegl, and S. Liedauer. Crystallization processes in quiescent and moving polymer melts under heat transfer conditions. *Progress in Polymer Science*, 15:629–714, 1990.

[59] G. Eder and H. Janeschitz-Kriegl. Structure development during processing: crystallization. In H. E. H. Meijer, editor, *Processing of Polymers*, number 18 in Materials Science and Technology: a Comprehensive Treatment, pages 269–342. Wiley-VCH, Weinheim, 1997.

[60] A. Elmoumni, H. H. Winter, A. J. Waddon, and H. Fruitwala. Correlation of material and processing time scales with structure development in isotactic polypropylene crystallization. *Macromolecules*, 36:6453–6461, 2003.

[61] A. Elmoumni and H. H. Winter. Large strain requirements for shear-induced crystallization of isotactic polypropylene. *Rheologica Acta*, 45:793–801, 2006.

[62] L. J. Fetters, D. J. Lohse, and W. W. Graessley. Chain dimensions and entanglement spacings in dense macromolecular systems. *Journal of Polymer Science, Part B: Polymer Physics*, 37:1023–1033, 1999.

[63] J. C. Fisher, J. H. Hollomon, and D. Turnbull. Nucleation. *Journal of Applied Physics*, 19:775–784, 1948.

[64] N. A. Frankel and A. Acrivos. On the viscosity of a concentrated suspension of solid spheres). *Chemical Engineering Science*, 22:847–853, 1967.

[65] H. Fröhlich and R. Sack. Theory of the rheological properties of dispersions. *Proceedings of the Royal Society of London A*, 185:415–430, 1946.

[66] M. Gahleitner, J. Wolfschwenger, C. Bachner, K. Bernreitner, and W. Neißl. Crystallinity and mechanical properties of PP-homopolymers as influenced by molecular structure and nucleation. *Journal of Applied Polymer Science*, 61:649–657, 1996.

[67] C. Gauthier, J.-F. Chailan, and J. Chauchard. Utilisation de l'analyse viscoélastique dynamique à l'étude de la crystallisation isotherme du poly(téréphtalate d'ethylène) amorphe. Application à des composites unidirectionnels avec fibres de verre. *Die Makromolekulare Chemie*, 193:1001–1009, 1992.

[68] R. H. Gee, N. Lacevic, and L. E. Fried. Atomistic simulations of spinodal phase separation preceding polymer crystallization. *Nature Materials*, 5:39–43, 2006.

[69] H. Giesekus. A simple constitutive equation for polymer fluids based on the concept of deformation-dependent tensorial mobility. *Journal of Non-Newtonian Fluid Mechanics*, 11:69–109, 1982.

[70] H. Giesekus. A unified approach to a variety of constitutive models for polymer fluids based on the concept of deformation-dependent molecular mobility. *Rheologica Acta*, 21:366–375, 1982.

[71] D. Graebling, R. Muller, and J.-F. Palierne. Linear viscoelastic behavior of some incompatible polymer blends in the melt. Interpretation of data with a model of emulsion of viscoelastic liquids. *Macromolecules*, 26:320–329, 1993.

[72] R. S. Graham, A. E. Likhtman, T. C. B. McLeish, and S. Milner. Microscopic theory of linear, entangled polymer chains under rapid deformation including chain stretch and convective constraint release. *Journal of Rheology*, 47:1171–1200, 2003.

[73] R. S. Graham and P. D. Olmsted. Coarse-grained simulations of flow-induced nucleation in semicrystalline polymers. *Physical Review Letters*, 103:115702-1–115702-4, 2009.

[74] R. S. Graham and P. D. Olmsted. Supplementary information. *Physical Review Letters*, 103, 2009.

[75] R. S. Graham and P. D. Olmsted. Kinetic Monte Carlo simulations of flow-induced nucleation in polymer melts. *Faraday Discussions*, 144:1–22, 2010.

[76] M. Grmela and H. C. Öttinger. Dynamics and thermodynamics of complex fluids. I. Development of a general formalism. *Physical Review E*, 56:6620–6632, 1997.

[77] C. Hadinata, C. Gabriel, M. Ruellman, and H. M. Laun. Comparison of shear-induced crystallization behavior of PB-1 samples with different molecular weight distribution. *Journal of Rheology*, 49:327–349, 2005.

[78] C. Hadinata, C. Gabriel, M. Ruellman, N. Kao, and H. M. Laun. Shear-induced crystallization of PB-1 up to processing-relevant shear rates. *Rheologica Acta*, 45:539–546, 2006.

[79] C. Hadinata, D. Boos, C. Gabriel, E. Wassner, M. Rüllmann, N. Kao, and M. Laun. Elongation-induced crystallization of a high molecular weight isotactic polybutene-1 melt compared to shear-induced crystallization. *Journal of Rheology*, 51:195–215, 2007.

[80] Z. Hashin. The elastic moduli of heterogeneous materials. *Transactions of the ASME, Series E,* 84, *Journal of Applied Mechanics*, 29:143–150, 1962.

[81] Z. Hashin and S. Shtrikman. A variational approach to the theory of the elastic behaviour of multiphase materials. *Journal of the Mechanics and Physics of Solids*, 11:127–140, 1963.

[82] Z. Hashin and B. W. Rosen. The elastic moduli of fiber-reinforced materials. *Transactions of the ASME, Series E,* 86, *Journal of Applied Mechanics*, 31:223–232, 1964.

[83] Z. Hashin. Viscoelastic behavior of heterogeneous media. *Transactions of the ASME, Series E,* 87, *Journal of Applied Mechanics*, 32:630–636, 1965.

[84] Z. Hashin. Complex moduli of viscoelastic composites - I. General theory and application to particulate composites. *International Journal of Solids and Structures*, 6:539–552, 1970.

[85] Z. Hashin. Complex moduli of viscoelastic composites - II. Fiber reinforced materials. *International Journal of Solids and Structures*, 6:797–807, 1970.

[86] E. L. Heeley, C. K. Poh, W. Li, A. Maidens, W. Bras, I. P. Dolbnya, A. J. Gleeson, N. J. Terrill, J. P. A. Fairclough, P. D. Olmsted, R. I. Ristic, M. J. Hounslow, and A. J. Ryan. Are metastable, precrystallisation, density-fluctuations a universal phenomena? *Faraday Discussions*, 122:343–361, 2002.

[87] E. L. Heeley, A. V. Maidens, P. D. Olmsted, W. Bras, I. P. Dolbnya, J. P. A. Fairclough, N. J. Terrill, and A. J. Ryan. Early stages of crystallization in isotactic polypropylene. *Macromolecules*, 36:3656–3665, 2003.

[88] E. L. Heeley, C. M. Fernyhough, R. S. Graham, P. D. Olmsted, N. J. Inkson, J. Embery, D. J. Groves, T. C. B. McLeish, A. C. Morgovan, F. Meneau, W. Bras, and A. J. Ryan. Shear-induced crystallization in blends of model linear and long-chain branched hydrogenated polybutadienes. *Macromolecules*, 39:5058–5071, 2006.

[89] J. J. Hermans. The elastic properties of fiber reinforced materials when the fibers are aligned. *Proceedings of the Koninklijke Nederlandse Akademie van Wetenschappen, Series B*, 70:1–9, 1967.

[90] E. Hervé and A. Zaoui. n-Layered inclusion-based micromechanical modelling. *International Journal of Engineering Science*, 31:1–10, 1993.

[91] E. Hervé and A. Zaoui. Elastic behaviour of multiply coated fibre-reinforced composites. *International Journal of Engineering Science*, 33:1419–1433, 1995.

[92] R. C. Hilborn. Sea gulls, butterflies, and grasshoppers: a brief history of the butterfly effect in nonlinear dynamics. *American Journal of Physics*, 72:425–427, 2004.

[93] R. Hill. A self-consistent mechanics of composite materials. *Journal of the Mechanics and Physics of Solids*, 13:213–222, 1965.

[94] R. Hill. Theory of mechanical properties of fibre-strengthened materials: III. Self-consistent model. *Journal of the Mechanics and Physics of Solids*, 13:189–198, 1965.

[95] R. H. Horst and H. H. Winter. Stable critical gels of a copolymer of ethene and 1-butene achieved by partial melting and recrystallization. *Macromolecules*, 33:7538–7543, 2000.

[96] R. H. Horst and H. H. Winter. Stable critical gels of a crystallizing copolymer of ethene and 1-butene. *Macromolecules*, 33:130–136, 2000.

[97] J.-W. Housmans, R. J. A. Steenbakkers, P. C. Roozemond, G. W. M. Peters, and H. E. H. Meijer. Saturation of pointlike nuclei and the transition to oriented structures in flow-induced crystallization of isotactic polypropylene. *Macromolecules*, 42:5728–5740, 2009.

[98] D. G. Hristova, G. W. M. Peters, and H. E. H. Meijer. Flow induced crystallization: effect of flow strength and temperature. In *Proceedings of the 228th ACS National Meeting*, Philadelphia, August 2004. CD-ROM.

[99] M. Hütter. Thermodynamically consistent incorporation of the Schneider rate equations into two-phase models. *Physical Review E*, 64:011209-1–011209-11, 2001.

[100] M. Hütter, G. C. Rutledge, and R. C. Armstrong. Crystal shapes and crystallization in continuum modeling. *Physics of Fluids*, 17:014107-1–014107-13, 2005.

[101] W. R. Hwang, M. A. Hulsen, H. E. H. Meijer, and T. H. Kwon. Direct numerical simulations of suspensions of spherical particles in a viscoelastic fluid in sliding tri-periodic domains. In *Proceedings of the XIVth International Congress on Rheology*, Seoul, August 2004.

[102] W. R. Hwang, M. A. Hulsen, and H. E. H. Meijer. Direct simulations of particle suspensions in a viscoelastic fluid in sliding bi-periodic frames. *Journal of Non-Newtonian Fluid Mechanics*, 121:15–33, 2004.

[103] W. R. Hwang and M. A. Hulsen. Direct numerical simulations of hard particle suspensions in planar elongational flow. *Journal of Non-Newtonian Fluid Mechanics*, 136:167–178, 2006.

[104] W. R. Hwang, G. W. M. Peters, M. A. Hulsen, and H. E. H. Meijer. Modeling of flow-induced crystallization of particle-filled polymers. *Macromolecules*, 39:8389–8398, 2006.

[105] H. Janeschitz-Kriegl. Conditions of nucleation in crystallizable polymers: reconnaissance of positions – a critical evaluation. *Colloid and Polymer Science*, 275:1121–1135, 1997.

[106] H. Janeschitz-Kriegl, E. Ratajski, and H. Wippel. The physics of athermal nuclei in polymer crystallization. *Colloid and Polymer Science*, 277:217–226, 1999.

[107] H. Janeschitz-Kriegl, E. Ratajski, and M. Stadlbauer. Flow as an effective promotor of nucleation in polymer melts: a quantitative evaluation. *Rheologica Acta*, 42:355–364, 2003.

[108] H. Janeschitz-Kriegl. How to understand nucleation in crystallizing polymer melts under real processing conditions. *Colloid and Polymer Science*, 281:1157–1171, 2003.

[109] H. Janeschitz-Kriegl and E. Ratajski. Kinetics of polymer crystallization under processing conditions: transformation of dormant nuclei by the action of flow. *Polymer*, 46:3856–3870, 2005.

[110] F. Jay, J.-M. Haudin, and B. Monasse. Shear-induced crystallization of polypropylenes: effect of molecular weight. *Journal of Materials Science*, 34:2089–2102, 1999.

[111] P. Jerschow. *Crystallization of Polypropylene. New Experiments, Evaluation Methods and Coice of Material Compositions*. PhD thesis, Johannes Kepler Universität Linz, 1994.

[112] P. Jerschow and H. Janeschitz-Kriegl. The role of long molecules and nucleating agents in shear induced crystallization of isotactic polypropylenes. *International Polymer Processing*, 12:72–77, 1997.

[113] K. K. Kabanemi and J.-F. Hétu. Nonequilibrium stretching dynamics of dilute and entangled linear polymers in extensional flow. *Journal of Non-Newtonian Fluid Mechanics*, 160:113–121, 2009.

[114] E. H. Kerner. The elastic and thermo-elastic properties of composite media. *Proceedings of the Physical Society of London B*, 69:808–813, 1956.

[115] Y. P. Khanna. Rheological mechanism and overview of nucleated crystallization kinetics. *Macromolecules*, 26:3639–3643, 1993.

[116] S. Kimata, T. Sakurai, Y. Nozue, T. Kasahara, N. Yamaguchi, T. Karino, M. Shibayama, and J. A. Kornfield. Molecular basis of the shish-kebab morphology in polymer crystallization. *Science*, 316:1014–1017, 2007.

[117] A. N. Kolmogorov. On the statistical theory of the crystallization of metals. *Bulletin of the Academy of Sciences of the USSR, Mathematics Series* (in Russian), 1:355–359, 1937.

[118] J. A. Kornfield, G. Kumaraswamy, and A. M. Issaian. Recent advances in understanding flow effects on polymer crystallization. *Industrial and Engineering Chemistry Research*, 41:6383–6392, 2002.

[119] G. Kumaraswamy, R. K. Verma, and J. A. Kornfield. Novel flow apparatus for investigating shear-enhanced crystallization and structure development in semicrystalline polymers. *Review of Scientific Instruments*, 70:2097–2104, 1999.

[120] G. Kumaraswamy, A. M. Issaian, and J. A. Kornfield. Shear-enhanced crystallization in isotactic polypropylene. 1. Correspondence between in situ rheo-optics and ex situ structure determination. *Macromolecules*, 32:7537–7547, 1999.

[121] G. Kumaraswamy, J. A. Kornfield, F. Yeh, and B. S. Hsiao. Shear-enhanced crystallization in isotactic polypropylene. 3. Evidence for a kinetic pathway to nucleation. *Macromolecules*, 35:1762–1769, 2002.

[122] G. Kumaraswamy. Crystallization of polymers from stressed melts. *Journal of Macromolecular Science, Part C: Polymer Reviews*, 45:375–397, 2005.

[123] R. G. Larson. A constitutive equation for polymer melts based on partially extending strand convection. *Journal of Rheology*, 28:545–571, 1984.

[124] R. G. Larson. *Constitutive Equations for Polymer Melts and Solutions*. Butterworth, London, 1988.

[125] J. I. Lauritzen Jr. and J. D. Hoffman. Extension of theory of growth of chain-folded polymer crystals to large undercoolings. *Journal of Applied Physics*, 44:4340–4352, 1973.

[126] A. I. Leonov. Nonequilibrium thermodynamics and rheology of viscoelastic polymer media. *Rheologica Acta*, 15:85–98, 1976.

[127] A. I. Leonov. On a class of constitutive equations for viscoelastic liquids. *Journal of Non-Newtonian Fluid Mechanics*, 25:1–59, 1987.

[128] A. I. Leonov. Analysis of simple constitutive equations for viscoelastic liquids. *Journal of Non-Newtonian Fluid Mechanics*, 42:323–350, 1992.

[129] S. Liedauer, G. Eder, H. Janeschitz-Kriegl, P. Jerschow, W. Geymayer, and E. Ingolic. On the kinetics of shear induced crystallization in polypropylene. *International Polymer Processing*, 8:236–244, 1993.

[130] A. E. Likhtman and R. S. Graham. Simple constitutive equation for linear polymer melts derived from molecular theory: Rolie-Poly equation. *Journal of Non-Newtonian Fluid Mechanics*, 114:1–12, 2003.

[131] C. Liu and M. Muthukumar. Langevin dynamics simulations of early-stage polymer nucleation and crystallization. *Journal of Chemical Physics*, 109:2536–2542, 1998.

[132] B. Lotz. What can polymer crystal structure tell about polymer crystallization processes? *European Physical Journal E*, 3:185–194, 2000.

[133] B. Lotz. Analysis and observation of polymer crystal structures at the individual stem level. *Advances in Polymer Science*, 180:17–44, 2005.

[134] A. Mahendrasingam, C. Martin, W. Fuller, D. J. Blundell, R. J. Oldman, J. L. Harvie, D. H. MacKerron, C. Riekel, and P. Engström. Effect of draw ratio and temperature on the strain-induced crystallization of poly(ethylene terephthalate) at fast draw rates. *Polymer*, 40:5553–5565, 1999.

[135] A. Mahendrasingam, D. J. Blundell, C. Martin, W. Fuller, D. H. MacKerron, J. L. Harvie, R. J. Oldman, and C. Riekel. Influence of temperature and chain orientation on the crystallization of poly(ethylene terephthalate) during fast drawing. *Polymer*, 41:7803–7814, 2000.

[136] A. Mahendrasingam, C. Martin, W. Fuller, D. J. Blundell, R. J. Oldman, D. H. MacKerron, J. L. Harvie, and C. Riekel. Observation of a transient structure prior to strain-induced crystallization in poly(ethylene terephthalate). *Polymer*, 41:1217–1221, 2000.

[137] A. Mahendrasingam, D. J. Blundell, A. K. Wright, V. Urban, T. Narayanan, and W. Fuller. Observations of structure development during crystallisation of oriented poly(ethylene terephthalate). *Polymer*, 44:5915–5925, 2003.

[138] A. Mahendrasingam, D. J. Blundell, M. Parton, A. K. Wright, J. Rasburn, T. Narayanan, and W. Fuller. Time resolved study of oriented crystallisation of poly(lactic acid) during rapid tensile deformation. *Polymer*, 46:6009–6015, 2005.

[139] A. Mahendrasingam, D. J. Blundell, C. Martin, V. Urban, T. Narayanan, and W. Fuller. Time resolved WAXS study of the role of mesophase in oriented crystallisation of poly(ethylene-*co*-isophthalate) copolymers. *Polymer*, 46:6044–6049, 2005.

[140] S. E. Mall-Gleissle, W. Gleissle, G. H. McKinley, and H. Buggisch. The normal stress behavior of suspensions with viscoelastic matrix fluids. *Rheologica Acta*, 41:61–76, 2002.

[141] J. A. Martins, W. Zhang, and A. M. Brito. Saturation of shear-induced isothermal crystallization of polymers at the steady state and the entanglement-disentanglement transition. *Macromolecules*, 39:7626–7634, 2006.

[142] T. C. B. McLeish and R. G. Larson. Molecular constitutive equations for a class of branched polymers: the pom-pom polymer. *Journal of Rheology*, 42:81–110, 1998.

[143] T. C. B. McLeish, J. Allgaier, D. K. Bick, G. Bishko, P. Biswas, R. Blackwell, B. Blottière, N. Clarke, B. Gibbs, D. J. Groves, A. Hakiki, R. K. Heenan, J. M. Johnson, R. Kant, D. J. Read, and R. N. Young. Dynamics of entangled H-polymers: theory, rheology, and neutron-scattering. *Macromolecules*, 32:6734–6758, 1999.

[144] M. Muthukumar. Commentary on theories of polymer crystallization. *European Physical Journal E*, 3:199–202, 2000.

[145] M. Muthukumar and P. Welch. Modeling polymer crystallization from solutions. *Polymer*, 41:8833–8837, 2000.

[146] O. O. Mykhaylyk, P. Chambon, R. S. Graham, J. P. A. Fairclough, P. D. Olmsted, and A. J. Ryan. The specific work of flow as a criterion for orientation in polymer crystallization. *Macromolecules*, 41:1901–1904, 2008.

[147] S. Nemat-Nasser and N. Yu. Bounds and estimates of overall moduli of composites with periodic microstructure. *Mechanics of Materials*, 15:163–181, 1993.

[148] S. Nemat-Nasser and M. Hori. *Micromechanics: Overall Properties of Heterogeneous Materials*. Elsevier, Amsterdam, 1993.

[149] N. Ohl and W. Gleissle. The characterization of the steady-state shear and normal stress functions of highly concentrated suspensions formulated with viscoelastic liquids. *Journal of Rheology*, 37:381–406, 1993.

[150] J. G. Oldroyd. The elastic and viscous properties of emulsions and suspensions. *Proceedings of the Royal Society of London A*, 218:122–132, 1953.

[151] P. D. Olmsted, W. C. K. Poon, T. C. B. McLeish, N. J. Terrill, and A. J. Ryan. Spinodal-assisted crystallization in polymer melts. *Physical Review Letters*, 81:373–376, 1998.

[152] H. C. Öttinger and M. Grmela. Dynamics and thermodynamics of complex fluids. II. Illustrations of a general formalism. *Physical Review E*, 56:6633–6655, 1997.

[153] J.-F. Palierne. Linear rheology of viscoelastic emulsions with interfacial tension. *Rheologica Acta*, 29:204–214, 1990. Errata available at http://www.mxpl.net.

[154] P. Panine, V. Urban, P. Boesecke, and T. Narayanan. Combined small- and wide-angle X-ray scattering study of early stages of polymer crystallization. *Journal of Applied Crystallography*, 36:991–994, 2003.

[155] P. Panine, E. Di Cola, M. Sztucki, and T. Narayanan. Early stages of polymer melt crystallization. *Polymer*, 49:676–680, 2008.

[156] G. W. M. Peters and F. P. T. Baaijens. Modelling of non-isothermal viscoelastic flows. *Journal of Non-Newtonian Fluid Mechanics*, 68:205–224, 1997.

[157] G. W. M. Peters, F. H. M. Swartjes, and H. E. H. Meijer. A recoverable strain-based model for flow-induced crystallization. *Macromolecular Symposia*, 185:277–292, 2002.

[158] G. W. M. Peters. A computational model for processing of semicrystalline polymers: the effects of flow-induced crystallization. In G. Reiter and J.-U. Sommer, editors, *Polymer Crystallization: Observations, Concepts and Interpretations*, pages 312–324. Springer, Berlin, 2003.

[159] N. Phan-Thien and D. C. Pham. Differential multiphase models for polydispersed suspensions and particulate solids. *Journal of Non-Newtonian Fluid Mechanics*, 72:305–318, 1997.

[160] N. V. Pogodina and H. H. Winter. Polypropylene crystallization as a physical gelation process. *Macromolecules*, 31:8164–8172, 1998.

[161] N. V. Pogodina, S. K. Siddiquee, J. W. van Egmond, and H. H. Winter. Correlation of rheology and light scattering in isotactic polypropylene during early stages of crystallization. *Macromolecules*, 32:1167–1174, 1999.

[162] N. V. Pogodina, H. H. Winter, and S. Srinivas. Strain effects on physical gelation of crystallizing isotactic polypropylene. *Journal of Polymer Science, Part B: Polymer Physics*, 37:3512–3519, 1999.

[163] N. V. Pogodina, V. P. Lavrenko, S. Srinivas, and H. H. Winter. Rheology and structure of isotactic polypropylene near the gel point: quiescent and shear-induced crystallization. *Polymer*, 42:9031–9043, 2001.

[164] P. Rubio and M. H. Wagner. A note added to "Molecular constitutive equations for a class of branched polymers: the pom-pom polymer" [J. Rheol. 42, 81 (1998)]. *Journal of Rheology*, 43:1709–1710, 1999.

[165] A. J. Ryan, J. P. A. Fairclough, N. J. Terrill, P. D. Olmsted, and W. C. K. Poon. A scattering study of nucleation phenomena in polymer crystallisation. *Faraday Discussions*, 112:13–29, 1999.

[166] H. M. Schaink, J. J. M. Slot, R. J. J. Jongschaap, and J. Mellema. The rheology of systems containing rigid spheres suspended in both viscous and viscoelastic media, studied by Stokesian dynamics simulations. *Journal of Rheology*, 44:473–498, 2000.

[167] J. D. Schieber, D. Nair, and T. Kitkrailard. Comprehensive comparisons with nonlinear flow data of a consistently unconstrained Brownian slip-link model. *Journal of Rheology*, 51:1111–1141, 2007.

[168] W. Schneider, A. Köppl, and J. Berger. Non-isothermal crystallization of polymers. System of rate equations. *International Polymer Processing*, 2:151–154, 1988.

[169] H. See, P. Jiang, and N. Phan-Thien. Concentration dependence of the linear viscoelastic properties of particle suspensions. *Rheologica Acta*, 39:131–137, 2000.

[170] J. Segurado and J. Llorca. A numerical approximation to the elastic properties of sphere-reinforced composites. *Journal of the Mechanics and Physics of Solids*, 50:2107–2121, 2002.

[171] M. Seki, D. W. Thurman, J. P. Oberhauser, and J. A. Kornfield. Shear-mediated crystallization of isotactic polypropylene: the role of long chain-long chain overlap. *Macromolecules*, 35:2583–2594, 2002.

[172] M. L. Sentmanat, S. G. Hatzikiriakos, and O. Delgadillo. An investigation of the flow induced crystallization behavior of polyethylene at high rates of extension. In *Proceedings of the 78*$^{\text{th}}$ *Annual Meeting of the Society of Rheology*, Portland, Maine, 2006.

[173] R. H. Somani, L. Yang, B. S. Hsiao, I. Sics, N. V. Pogodina, H. H. Winter, P. K. Agarwal, H. A. Fruitwala, and A. H. Tsou. Orientation-induced crystallization in isotactic polypropylene melt by shear deformation. *Macromolecular Symposia*, 185:105–117, 2002.

[174] R. H. Somani, L. Yang, L. Zhu, and B. S. Hsiao. Flow-induced shish-kebab precursor structures in entangled polymer melts. *Polymer*, 46:8587–8623, 2005.

[175] M. Stadlbauer, H. Janeschitz-Kriegl, G. Eder, and E. Ratajski. New extensional rheometer for creep flow at high tensile stress. Part II. Flow induced nucleation for the crystallization of iPP. *Journal of Rheology*, 48:631–639, 2004.

[176] P. S. Stephanou, C. Baig, and V. G. Mavrantsas. A generalized differential constitutive equation for polymer melts based on principles of nonequilibrium thermodynamics. *Journal of Rheology*, 53:309–337, 2009.

[177] G. Strobl. From the melt via mesomorphic and granular crystalline layers to lamellar crystallites: a major route followed in polymer crystallization? *European Physical Journal E*, 3:165–183, 2000.

[178] G. Strobl. A thermodynamic multiphase scheme treating polymer crystallization and melting. *European Physical Journal E*, 18:295–309, 2005.

[179] G. Strobl. Crystallization and melting of bulk polymers: new observations, conclusions and a thermodynamic scheme. *Progress in Polymer Science*, 31:398–442, 2006.

[180] M. J. Struglinski and W. W. Graessley. Effects of polydispersity on the linear viscoelastic properties of entangled polymers. 1. Experimental observations for binary mixtures of linear polybutadiene. *Macromolecules*, 18:2630–2643, 1985.

[181] F. H. M. Swartjes. *Stress Induced Crystallization in Elongational Flow*. PhD thesis, Technische Universiteit Eindhoven, 2001. Available at http://www.mate.tue.nl/mate.

[182] F. H. M. Swartjes, G. W. M. Peters, S. Rastogi, and H. E. H. Meijer. Stress induced crystallization in elongational flow. *International Polymer Processing*, 18:53–66, 2003.

[183] R. I. Tanner. A suspension model for low shear rate polymer solidification. *Journal of Non-Newtonian Fluid Mechanics*, 102:397–408, 2002.

[184] R. I. Tanner. On the flow of crystallizing polymers I. Linear regime. *Journal of Non-Newtonian Fluid Mechanics*, 112:251–268, 2003.

[185] R. I. Tanner and F. Qi. A phenomenological approach to suspensions with viscoelastic matrices. *Korea-Australia Rheology Journal*, 17:149–156, 2005.

[186] N. J. Terrill, P. A. Fairclough, E. Towns-Andrews, B. U. Komanschek, R. J. Young, and A. J. Ryan. Density fluctuations: the nucleation event in isotactic polypropylene crystallization. *Polymer*, 39:2381–2385, 1998.

[187] D. G. Thomas. Transport characteristics of suspension: VIII. A note on the viscosity of Newtonian suspensions of uniform spherical particles. *Journal of Colloid Science*, 20:267–277, 1965.

[188] S. Torquato. Effective stiffness tensor of composite media–I. Exact series expansions. *Journal of the Mechanics and Physics of Solids*, 45:1421–1448, 1997.

[189] S. Torquato. Effective stiffness tensor of composite media: II. Applications to isotropic dispersions. *Journal of the Mechanics and Physics of Solids*, 46:1411–1440, 1998.

[190] S. Torquato. *Random Heterogeneous Materials: Microstructure and Macroscopic Properties*. Springer, Berlin, 2002.

[191] C. Tribout, B. Monasse, and J. M. Haudin. Experimental study of shear-induced crystallization of an impact polypropylene copolymer. *Colloid and Polymer Science*, 274:197–208, 1996.

[192] S. Uemura and M. Takayanagi. Application of the theory of elasticity and viscosity of two-phase systems to polymer blends. *Journal of Applied Polymer Science*, 10:113–125, 1966.

[193] J. Van Meerveld, M. Hütter, and G. W. M. Peters. Continuum model for the simulation of fiber spinning, with quiescent and flow-induced crystallization. *Journal of Non-Newtonian Fluid Mechanics*, 150:177–195, 2008.

[194] J. van Meerveld. Note on the thermodynamic consistency of the integral pom-pom model. *Journal of Non-Newtonian Fluid Mechanics*, 108:291–299, 2002.

[195] J. van Meerveld, G. W. M. Peters, and M. Hütter. Towards a rheological classification of flow induced crystallization experiments of polymer melts. *Rheologica Acta*, 44:119–134, 2004.

[196] J. van Meerveld. *Model Development and Validation of Rheological and Flow Induced Crystallization Models for Entangled Polymer Melts*. PhD thesis, Eidgenössische Technische Hochschule Zürich, 2005.

[197] N. J. L. van Ruth, J. F. Vega, S. Rastogi, and J. Martínez-Salazar. Viscoelastic behaviour during the crystallisation of isotactic polypropylene. *Journal of Materials Science*, 41:3899–3905, 2006.

[198] J. F. Vega, D. G. Hristova, and G. W. M. Peters. Flow induced crystallization regimes and rheology of isotactic polypropylene: effects of molecular architecture. *Journal of Thermal Analysis & Calorimetry*. Accepted.

[199] W. M. H. Verbeeten. *Computational Melt Rheology*. PhD thesis, Technische Universiteit Eindhoven, 2001. Available at http://www.mate.tue.nl/mate.

[200] W. M. H. Verbeeten, G. W. M. Peters, and F. P. T. Baaijens. Differential constitutive equations for polymer melts: the extended Pom-Pom model. *Journal of Rheology*, 45:823–843, 2001.

[201] W. M. H. Verbeeten, G. W. M. Peters, and F. P. T. Baaijens. Viscoelastic analysis of complex polymer melt flows using the eXtended Pom-Pom model. *Journal of Non-Newtonian Fluid Mechanics*, 108:301–326, 2002.

[202] W. M. H. Verbeeten, G. W. M. Peters, and F. P. T. Baaijens. Numerical simulations of the planar contraction flow for a polyethylene melt using the XPP model. *Journal of Non-Newtonian Fluid Mechanics*, 117:73–84, 2004.

[203] S. Vleeshouwers and H. E. H. Meijer. A rheological study of shear induced crystallization. *Rheologica Acta*, 35:391–399, 1996.

[204] L. J. Walpole. On bounds for the overall elastic moduli of inhomogeneous systems - I. *Journal of the Mechanics and Physics of Solids*, 14:151–162, 1966.

[205] E. Wassner and R.-D. Maier. Shear-induced crystallization of polypropylene melts. In *Proceedings of the XIIIth International Congress on Rheology*, Cambridge, August 2000.

[206] H. A. Waterman. Relations between loss angles in isotropic linear viscoelastic materials. *Rheologica Acta*, 16:31–42, 1977.

[207] M. W. L. Wilbrink, M. A. J. Michels, W. P. Vellinga, and H. E. H. Meijer. Rigidity percolation in dispersions with a structured viscoelastic matrix. *Physical Review E*, 71:031402-1–031402-10, 2005.

[208] H. H. Winter and M. Mours. Rheology of polymers near liquid-solid transitions. *Advances in Polymer Science*, 134:165–234, 1997.

[209] M. D. Wolkowicz. Nucleation and crystal growth in sheared poly(1-butene) melts. *Journal of Polymer Science, Polymer Symposia*, 63:365–382, 1978.

[210] L. Yang, R. H. Somani, I. Sics, B. S. Hsiao, R. Kolb, H. Fruitwala, and C. Ong. Shear-induced crystallization precursor studies in model polyethylene blends by in-situ rheo-SAXS and rheo-WAXD. *Macromolecules*, 37:4845–4859, 2004.

[211] P. Zoller and D. J. Walsh. *Standard Pressure-Volume-Temperature Data for Polymers*. Technomic, Lancaster, 1995.

[212] H. Zuidema. *Flow-Induced Crystallization of Polymers; Application to Injection Moulding*. PhD thesis, Technische Universiteit Eindhoven, 2000. Available at http://www.mate.tue.nl/mate.

[213] H. Zuidema, G. W. M. Peters, and H. E. H. Meijer. Development and validation of a recoverable strain-based model for flow-induced crystallization of polymers. *Macromolecular Theory and Simulations*, 10:447–460, 2001.

Samenvatting

Stromingsgeïnduceerde kristallisatie (flow-induced crystallization, FIC) is de bepalende factor voor de eigenschappen van in de smelt verwerkte semikristallijne polymeren producten.[1] Er is daarom al veel wetenschappelijk onderzoek aan gewijd, zowel experimenteel als theoretisch. Hoewel de essentiële fenomenen in FIC langzaam onthuld worden, ontbreekt nog een overkoepelend theoretisch raamwerk, waarmee al deze fenomenen verklaard kunnen worden.

Kristallisatie van polymeren is in drie regimes op te delen:

1. kristallisatie in rust, waarbij bolvormige structuren (sferulieten) gevormd worden,
2. door stroming versterkte nucleatie, met als gevolg een groter aantal sferulieten,
3. vorming van georiënteerde vezels, de nuclei van anisotrope kristallijne structuren.

Wanneer de snelheid of duur van stroming verhoogd wordt, zien we overgangen van regime 1 naar regime 2 en regime 3. Het doel van dit proefschrift is te onderzoeken hoe versterkte nucleatie (regime 2) gemodelleerd kan worden vanuit een reologische benadering, inclusief de koppeling tussen de gevormde structuur en het viscoelastische gedrag van de smelt.

De resultaten van dit proefschrift zijn tweeledig. Ten eerste wordt de reologie van polymere smelten in de late stadia van kristallisatie, waarin, in regime 2, sferulieten groeien, beschreven met een viscoelastisch suspensiemodel. Ten tweede wordt versterkte nucleatie in de vroege stadia, die de latere ontwikkeling van de sferulitische structuur bepaalt, gemodelleerd. Een lokale en een globale formulering van dit fenomeen worden vergeleken. De lokale formulering biedt een consistent theoretisch concept voor de vorming en nucleatie van stromingsgeïnduceerde precursors (subkritische nuclei). Het is echter nog niet in staat om experimentele waarnemingen te verklaren. De meer empirische globale formulering stemt daarentegen zeer goed overeen met experimentele data. Uit deze resultaten volgen conclusies en aanbevelingen voor toekomstig onderzoek.

---

[1] Strikt spreekt men van *polymere* materialen – ‘van de aard van polymerie of gepaard gaand met polymerisatie’ [Van Dale, 14^{e} Editie (2005)] – maar niet van hieruit vervaardigde *polymeren* producten.

Acknowledgements

This thesis would not have turned out the way it did without the input and support of several people, first and foremost Gerrit Peters, with whom I had countless exciting discussions. From the very beginning of my project, he and Han Meijer have been (co)promotor in the most literal sense of the word. Gentlemen, thank you for the excellent PR.

I enjoyed the sometimes heated debates in our FIC group meetings. Past and present FICkers, thanks for the fun as well as the occasional learning experiences. An extra word of appreciation for those who gave me what I could never have obtained by my own hands, namely reliable experimental data: Denka Hristova, Juan Vega, and Jan-Willem Housmans. Also thumbs up to all other colleagues who helped me out in any way.

Outside Eindhoven, I am indebted to the following people. Jimmy Baert and Peter van Puyvelde from KU Leuven for their contribution to Chapter 5, Jimmy in particular for doing the experiments. Susana Filipe and Markus Gahleitner from Borealis for the extensional viscosity measurements, used in Chapter 4. The Crystal µPPets, especially Richard Graham and Peter Olmsted, for their helpful comments. Julie Kornfield for inviting me to Caltech and for the long discussions on FIC (with digressions to politics) during my stays. Jay Schieber for the opportun*ii*ty to visit Chicago and for being the one whose criticism, in the end, inspired Chapter 3.

Cheers to you all!

Rudi,
Eindhoven, November 2009

Curriculum vitae

Rudi Steenbakkers was born on the 23rd of February 1978 in Geldrop, the Netherlands. He completed his pre-university secondary education at the College Asten-Someren (currently Varendonck College) in Asten, the Netherlands, in 1996. Between 1996 and 2005 he studied Mechanical Engineering at Eindhoven University of Technology, at the same time being a voluntary bartender and secretary of a youth center near his home town, and playing guitar in bands from amateur to semi-professional level.

In 2003, as part of his Master track, Rudi spent three months at the Technische Universität Berlin in the group of professor Manfred H. Wagner, for a project on modeling of strain hardening of long-chain branched polymer melts. In 2005, he successfully defended his Master thesis 'Modeling Flow-Induced Crystallization of Polymers' under supervision of dr. Gerrit W. M. Peters and professor Han E. H. Meijer at the Materials Technology Institute (m@te) at Eindhoven University of Technology.

From 2005 to 2009, Rudi continued his work on flow-induced crystallization in a PhD project with the same supervisors. During this project, he spent short periods of time in the group of professor Julia A. Kornfield at California Institute of Technology and in the group of professor Jay D. Schieber at Illinois Institute of Technology. He also participated in the UK-based second Microscale Polymer Processing (μPP^2) project. He successfully completed the following postgraduate courses from the National Dutch Graduate School of Polymer Science and Technology, PTN: Polymer Processing, Polymer Innovations, Polymer Physics, and Polymer Properties.

During his PhD project, Rudi was a board member of Hora Est, the PhD Association of Mechanical and Biomedical Engineering at Eindhoven University of Technology, and editor of their magazine, the Pedel. He also developed a method to determine the winner of the public award in the annual m@te poster contest, which, due to the peculiar voting system, is not as easy as it sounds. Unfortunately, his own method has never made him win.

List of publications

- R.J.A. Steenbakkers and G.W.M. Peters. Suspension-based rheological modeling of crystallizing polymer melts. *Rheologica Acta*, 47:643–665, 2008.
- J.-W. Housmans, R.J.A. Steenbakkers, P.C. Roozemond, G.W.M. Peters, and H.E.H. Meijer. Saturation of pointlike nuclei and the transition to oriented structures in flow-induced crystallization of isotactic polypropylene. *Macromolecules*, 42:5728–5740, 2009.
- F.J.M.F. Custódio, R.J.A. Steenbakkers, P.D. Anderson, G.W.M. Peters, and H.E.H. Meijer. Model development and validation of crystallization behavior in injection molding prototype flows. *Macromolecular Theory and Simulations*. In print.
- R.J.A. Steenbakkers. Laplace's law and the interfacial momentum source in two-phase models. *Physical Review E*. Accepted.